The Effect of Quantum Confinement on the Thermoelectric Figure of Merit

by

Xiangzhong Sun

B. S., Tsinghua University, Beijing (1991)
M. S., Tsinghua University, Beijing (1993)

Submitted to the Department of Physics
in partial fulfillment of the requirements for the degree of

Doctor of Philosophy

at the

MASSACHUSETTS INSTITUTE OF TECHNOLOGY

June 1999

Author .....
Department of Physics
April 30, 1999

Certified by .....
Mildred S. Dresselhaus
Institute Professor
Thesis Supervisor

Accepted by .....
Thomas J. Greytak
Associate Department Head for Education

The Effect of Quantum Confinement on the Thermoelectric Figure of Merit

by

Xiangzhong Sun

Submitted to the Department of Physics
on April 30, 1999, in partial fulfillment of the
requirements for the degree of
Doctor of Philosophy

Abstract

The thermoelectric figure of merit (Z) determines the usefulness of a material for thermoelectric energy conversion applications. Since the 1960's, the best thermoelectric material has been Bi_2Te_3 alloys, with a ZT of 1.0 at a temperature of $T = 300$ K. The advancement of nano-scale technologies has opened up the possibility of engineering materials at nano-scale dimensions to achieve low-dimensional thermoelectric structures which may be superior to their bulk forms. In this thesis, I established the basis of the low dimensional thermoelectric transport principle in the $Si/Si_{1-x}Ge_x$ quantum well superlattice (two-dimensional) system and in the Bi quantum wire (one-dimensional) system. In bulk form, $Si_{1-x}Ge_x$ is a promising thermoelectric material for high temperature applications. The $Si/Si_{1-x}Ge_x$ quantum well superlattice structures are studied based on their electronic band structures using semiclassical transport theory. Detailed subband structures are considered in an infinite series of finite height quantum wells and barriers. A significant enhancement of the thermoelectric figure of merit is expected. Based on my calculations, experimental studies are designed and performed on MBE grown $Si/Si_{1-x}Ge_x$ quantum well superlattice structures. The experimental results are found to be consistent with theoretical predictions and indicate a significant enhancement of Z within the quantum wells over bulk values. The bismuth quantum wire system is a one-dimensional (1D) thermoelectric system. Bismuth as a semimetal is not a good thermoelectric material in bulk form because of the approximate cancellation between the electron and hole contributions to the Seebeck coefficient. However, quantum confinement can be introduced by making Bi nanowires to yield a 1D semiconductor. 1D transport properties are calculated along the principal crystallographic directions. By carefully tailoring the Bi wire size and carrier concentration, substantial enhancement in Z is expected. A preliminary experimental study of Bi nanowire arrays is also presented.

Thesis Supervisor: Mildred S. Dresselhaus
Title: Institute Professor

Acknowledgments

First I would like to deeply thank my supervisor Professor Mildred Dresselhaus for her guidance to make this thesis happen. The most fortunate thing happened to me at M.I.T. was to have the opportunity to carry out my graduate research in her group. The training I have received from her has been diverse and complete, a lot more than just science itself. Her spirit, her energy, and her high level of perfection are going to give me constant courage to strive for success in the rest of my life.

My thesis research would not have been half as successful without the contribution of Professor Kang L. Wang of the University of California at Los Angeles, who provided all the superlattice samples throughout the past four years. Drs. Jianlin Liu and Martin Tanner, who grew all the samples, should take the most credit for the success of the experimental side of my thesis. I am also very grateful to Professor Gang Chen of the University of California at Los Angeles for providing the simulation programs for the thermal conductivity of superlattices, and to Dr. Tamara Radetic of the University of California at Berkeley for providing the TEM pictures of the superlattice samples. The discussions with Dr. Cronin Vining of ZT Services, Dr. Ted Harman of M.I.T. Lincoln Laboratory, and Dr. Jos Heremans of Delphi Research & Development Center have also been inspiring and fruitful.

I am also indebted to Professors Morinobu Endo, Riichiro Saito, and Dr. Herbert Zeiger for their help on my research on graphite fibers and carbon nanotubes, which, unfortunately, could not be included in this thesis.

Dresselhaus group has been a great place to stay. The precious friendships and the cheerful environment are all going to be unforgettable. Lyndon Hicks kept impressing me with his deep understanding of Physics and his sharp mathematics and computer skills. I thank him for establishing the initial low dimensional thermoelectricity framework which made this thesis possible. Steve Cronin and Takaaki Koga gave me a lot of help during my research, both experimentally and theoretically. The memorable trip to Kentucky with Steve and Taka was a lot of fun. Zhibo Zhang had always impressed me with his energy and speed. For the new thermoelectricians,

Marcie Black and Yu-Ming Lin, I wish them the best of the luck in their adventures. Outside the thermoelectric "community", I have a lot of people to thank. James Chen was my officemate for the first two years, and he is one of the funniest and most cheerful persons I have ever known. My good friends Ibo Matthews and Sandra Brown taught me a lot about carbon materials. I thank Alex Fung and Xiang-Xin Bi for teaching me Raman spectroscopy, Gillian Reynolds for teaching me photoconductivity measurements, Boris Pevzner for computer tips, and Ching-Hwa Kiang and Huiming Cheng for the collaborations on carbon nanotube research. I had a lot of joyful time with Marcos Pimenta talking about the World Cup and Ronaldo. Alessandra Marucci, Dima Gekhtman, Hao Xin, Lorenzo Bergomi, Joe Habib, Paola Corio were all great to be around. I am grateful to Laura Doughty for everything she has done to me. Her hard work keeps the whole group in harmony. Gene Dresselhaus is not only an exceptional physicist, but also a true UNIX lover. I am grateful to him for the trust of letting me take care of the computer system for the group.

Words could not express my gratitude to my parents, who loved me, raised me, supported me, and helped me in every way they could. Unlimited thanks go to my wife Yi for her companionship and patience during my stay at M.I.T. Without her love and support, this thesis would not have been possible. It is to her that this thesis is dedicated.

Contents

List of Figures

List of Tables

Chapter 1

Introduction to thermoelectricity

1.1 A brief history

Thermoelectricity was discovered by Seebeck in the nineteenth century [1]. Modern research in thermoelectrics started with Ioffe's observation [2] that doped semiconductors should be the best thermoelectrics. He also proposed that thermoelectrics could be used to make solid state refrigerators, which would have no moving parts and would last indefinitely.

Ioffe's suggestions ignited a frenzy of worldwide activity. During the period of 1957–1965, measurements were done on every known semiconductor, semimetal, and on many alloys. The best refrigeration materials were discovered at that time: bismuth telluride, lead telluride, and bismuth antimony alloys. However, the best materials produced refrigerators of poor efficiency. The benchmark for efficiency is the Freon compressor in every household. Thermoelectric refrigerators have about one-third of the efficiency of Freon technology, so that today thermoelectric refrigerators are not a competitive technology for most refrigerator uses.

For the past 30 years, after the very active period of 1957–1965, thermoelectric research has been a small activity in the world. In the United States the major activity has been to build power sources for spacecraft and space stations. This activity has developed new thermoelectric materials, such as $Si_{1-x}Ge_x$ alloys, that work well at high temperature ($\sim$1000 K) with moderate efficiencies (0.2–0.3 of Carnot efficiency).

Recent research has found another material that has good thermoelectric properties at high temperatures: the skutterudites [3] which work well at 700 K. $CoAs_3$, discovered in Skutterud, Norway, serves as the prototype for this class of materials. Although cubic, the crystal structure is complicated. There are either 16 or 32 atoms per unit cell, depending on how one counts. The lattice has empty sites into which other atoms can be inserted. This leads to a related class of materials called filled skutterudites, discovered by Jeitschko and Braun [4]. If the atoms in the cage sites are small and can rattle around, the thermal conductivity is lowered significantly. These materials are under active investigation regarding their thermoelectric properties.

The introduction of quantum scaled structures [5–8] into this field has aroused a great deal of research activity during the past few years. The enhancement in the density of states at the Fermi level due to quantum confinement in low dimensional structures, such as quantum wells and quantum wires, makes these systems outperform their bulk forms significantly. A number of materials systems are being investigated for their potential as thermoelectrics [9–16].

Besides the main research activities in this field, some new research directions, such as phonon engineering [17] and carrier pocket engineering [18], have also emerged.

1.2 Thermoelectric effects

1.2.1 The Seebeck effect

When a temperature gradient is maintained in a material and no electric current is allowed to flow, there will be a steady-state electrostatic potential difference between the high- and low-temperature regions of the specimen. The corresponding electric field is known as the thermoelectric field and is conventionally written as

$$\mathbf{E} = \mathbf{S} \cdot \nabla T, \tag{1.1}$$

where the proportionality constant $\mathbf{S}$ is known as the Seebeck coefficient or the thermoelectric power of the material, which is in general a second rank symmetric tensor

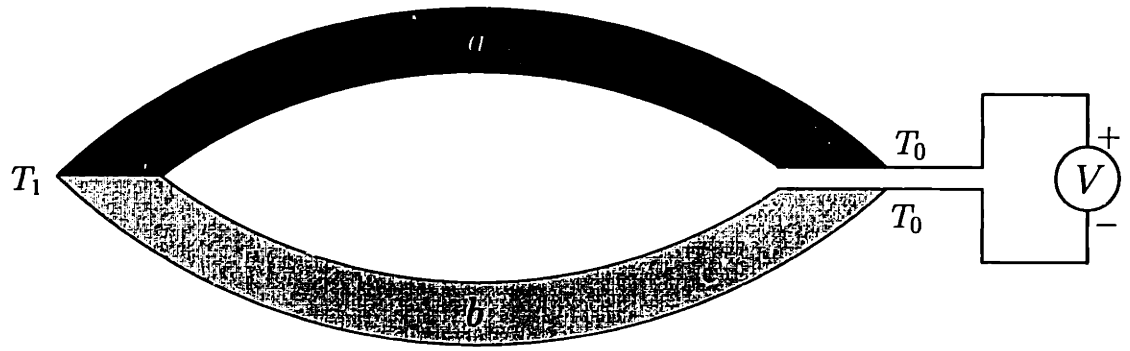

Figure 1-1: Circuit for measuring the difference in thermoelectric voltages developed in two different materials (a and b), in each of which the temperature varies from T_0 to T_1.

for anisotropic materials.

To measure this thermoelectric voltage, one must use a circuit of two different materials (Fig. 1-1), connected so that one junction is at a temperature T_1 and the other junction is open circuited (bridged only by a voltmeter) at a temperature $T_0 \neq T_1$. This is necessary to avoid a temperature gradient within the circuitry of the meter itself, accompanied by an additional thermoelectric voltage. The thermoelectric voltage measured across the voltmeter is then

$$\Delta V = \int \mathbf{E} \cdot d\mathbf{l} = -S_{ab}\Delta T, \tag{1.2}$$

where S_{ab} is the differential Seebeck coefficient between the elements a and b. Note that $S_{ab} = S_a - S_b$, whereas the absolute value of S for a single material is measured relative to a superconductor for which $S = 0$.

1.2.2 The Peltier effect

If an electrical current is driven in a circuit of two dissimilar materials that is maintained at a uniform temperature, then heat will be evolved at one junction and absorbed at the other (Fig. 1-2). This is because an isothermal electric current in a

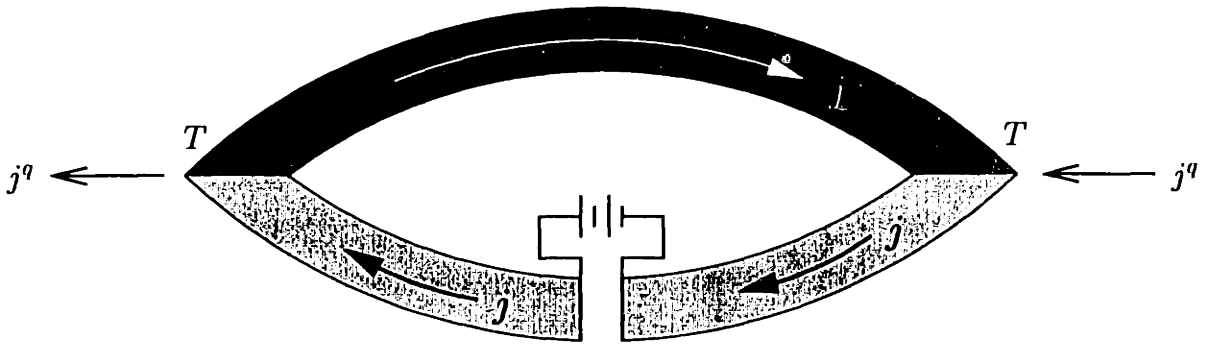

Figure 1-2: The Peltier effect. A current $\mathbf{j}$ is driven in a circuit of two dissimilar materials at uniform temperature T. Thermal current q is evolved at one junction and supplied at the other.

material is accompanied by a thermal current,

$$\mathbf{j}^q = \mathbf{\Pi} \cdot \mathbf{j}, \tag{1.3}$$

where $\mathbf{j}$ and $\mathbf{j}^q$ are the electrical and thermal current densities, respectively, and $\mathbf{\Pi}$ is known as the Peltier coefficient which is in general a second rank symmetric tensor for anisotropic materials. Because the electric current is uniform in the closed circuit and the Peltier coefficient differs from material to material, the thermal current in the two materials will not be equal, and the difference must be evolved at one junction and supplied to the other if a uniform temperature is to be maintained.

In the circuit shown in Fig. 1-2, a thermal flow j^q is generated[1] according to the differential Peltier coefficient between the two elements $\Pi_{ab} = \Pi_a - \Pi_b$. The absolute value of the Peltier coefficient for a single element is determined when one of the two branches is a superconductor.

1.2.3 The Thomson effect

Consider a homogeneous conductor in which thermal and electric current flow simultaneously. If a temperature gradient, ∇T, is maintained within the specimen, heat

[1]Note that j^q is the heat flow generated at the junctions. It is a scalar rather than a vector.

can be generated or absorbed due to the difference in the thermal energy of carriers which is determined by the local temperature. The rate at which heat is generated or absorbed in a unit volume due to the Thomson effect is a scalar which can be expressed as

$$\frac{dq}{dt} = -\mathbf{j} \cdot \boldsymbol{\tau} \cdot \nabla T, \tag{1.4}$$

where $\mathbf{j}$ is the electric current density in the specimen and the proportionality constant $\boldsymbol{\tau}$ is known as the Thomson coefficient, which is in general a second rank tensor for anisotropic materials. Note that $\boldsymbol{\tau}$ is here defined for a single material. A junction is not needed.

The three thermoelectric coefficients, the Seebeck coefficient, $\mathbf{S}$, the Peltier coefficient, $\boldsymbol{\Pi}$, and the Thomson coefficient, $\boldsymbol{\tau}$, are related to each other by the application of the theory of thermodynamics [2]:

$$\boldsymbol{\Pi} = \mathbf{S}T, \tag{1.5}$$

and

$$\boldsymbol{\tau} = T\frac{d\mathbf{S}}{dT}, \tag{1.6}$$

where T is the absolute temperature.

1.3 Thermoelectric refrigeration

Without any loss of generality, we consider a single thermocouple shown in Fig. 1-3 as a simple model for a thermoelectric refrigerator [19, 20], which may form part of a module that consists of many such couples that act thermally in parallel. One such couple consists of two branches of p-type and n-type legs, and the direction of electrical current[2] shown in Fig. 1-3 is such as to cool the heat source and to heat the heat sink. The branches have the transport parameters S_p, σ_p, κ_p and S_n, σ_n, κ_n,

[2]This electrical current drives the carriers, including both electrons and holes, in both the n-type and p-type legs. The direction of the electric current is shown in Fig. 1-3 as is the direction of the thermal current. The diagram shows that the thermal energy carried by the carriers is transferred from the heat source to the heat sink.

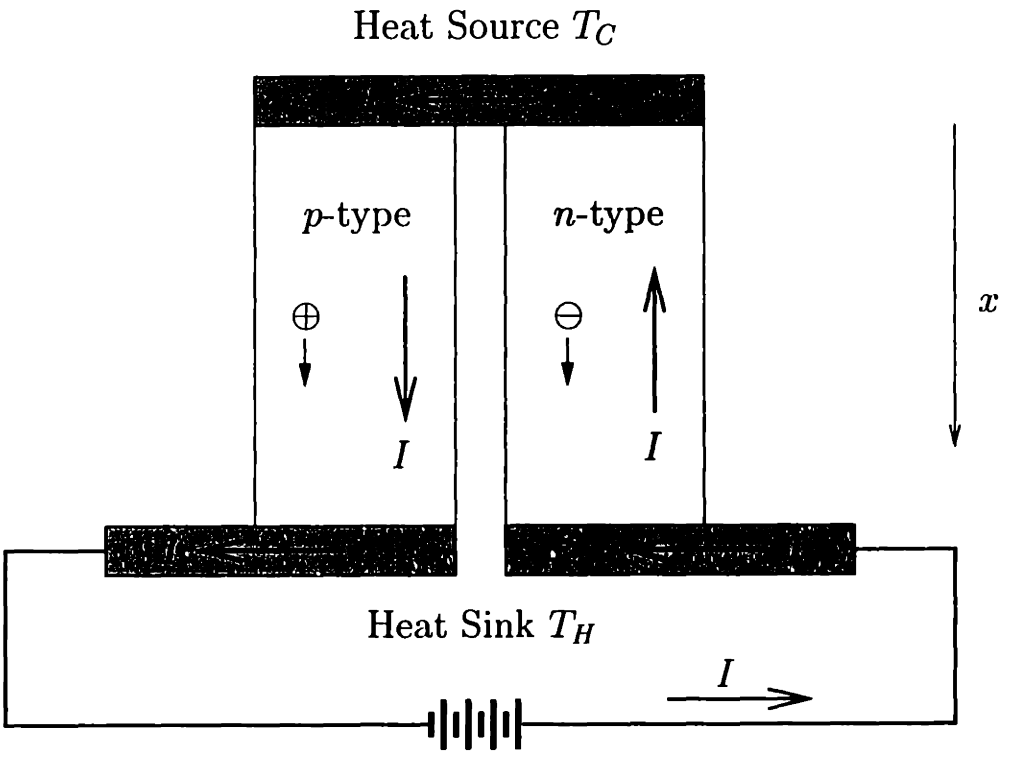

Figure 1-3: Simple thermoelectric refrigerator.

respectively, where S is the Seebeck coefficient, σ is the electrical conductivity and κ is the thermal conductivity. For simplicity, we assume that these parameters are temperature independent.[3] The branches have constant cross-sectional areas A_p and A_n and are of length L_p and L_n. They are joined by a link of zero electrical resistance at the heat source and by a source of emf, which produces a current I, at the heat sink. The temperatures of the heat source and sink are T_C and T_H, respectively, denoting cold and hot junctions. It is assumed that there is no heat transfer to or from the environment other than at the source or the sink.

Our goal is to find the thermoelectric coefficient of performance for a given temperature difference between the source and the sink. The thermoelectric coefficient of performance is defined as the ratio of the rate at which heat is extracted from the source to the rate of expenditure of electrical energy. Another quantity of interest is

[3]See page 34 for a brief discussion considering the temperature dependent parameters. In fact, this assumption is not a serious approximation because ΔT for a single couple in an actual multistage device will be small.

the maximum temperature difference that can be achieved when no heat has to be extracted from the source.

The rate of heat flow q_i within one of the conductors i ($i = p, n$) at a distance x from the heat source is given by

$$q_{p,n} = \pm S_{p,n} I T - \kappa_{p,n} A_{p,n} \frac{dT}{dx}, \tag{1.7}$$

where T is the absolute temperature at x and the Peltier coefficient Π has been expressed as ST using Eq. (1.5). The $\pm$ sign in front of the Peltier term in Eq. (1.7) is because the electric current flowing in the n-branch is in the opposite direction to the heat flow or in the $+x$ direction as defined in Fig. 1-3. Since S_n is a negative quantity, the thermoelectric heat flow from the source to the sink through both branches is positive and is opposed by the effect of thermal conduction which tries to bring the hot junction in thermal equilibrium with the cold junction.

Within the two branches of Fig. 1-3 the rate of generation of heat per unit length from the Joule effect is given by

$$\frac{I^2}{\sigma_{p,n} A_{p,n}} = -\kappa_{p,n} A_{p,n} \frac{d^2T}{dx^2}. \tag{1.8}$$

There are no thermoelectric terms in Eq. (1.8) when the Seebeck coefficient is independent of temperature, since the Thomson coefficient is zero (Eq. (1.6)).

Equation (1.8) must be solved with the boundary conditions $T|_{x=0} = T_C$ and $T|_{x=L_{p,n}} = T_H$. Thus we find the heat flow at a point x in Fig. 1-3 is given by

$$\kappa_{p,n} A_{p,n} \frac{dT}{dx} = -\frac{I^2 (x - \frac{1}{2} L_{p,n})}{\sigma_{p,n} A_{p,n}} + \frac{\kappa_{p,n} A_{p,n} (T_H - T_C)}{L_{p,n}}. \tag{1.9}$$

By substitution in Eq. (1.7), at $x = 0$,

$$q_{p,n}|_{x=0} = \pm S_{p,n} I T_C - \frac{\kappa_{p,n} A_{p,n} (T_H - T_C)}{L_{p,n}} - \frac{I^2 L_{p,n}}{2\sigma_{p,n} A_{p,n}}. \tag{1.10}$$

The cooling power, q_C, at the source is the sum of q_p and q_n at $x = 0$:[4]

$$q_C = (S_p - S_n)IT_C - K(T_H - T_C) - \frac{1}{2}I^2R, \tag{1.11}$$

where the thermal conductance, K, of the two branches in parallel is given by

$$K = \frac{\kappa_p A_p}{L_p} + \frac{\kappa_n A_n}{L_n}, \tag{1.12}$$

and the electrical resistance, R, of the two branches in series is given by

$$R = \frac{L_p}{\sigma_p A_p} + \frac{L_n}{\sigma_n A_n}. \tag{1.13}$$

The electrical power consumed in the branches is given by

$$W_{p,n} = \pm S_{p,n} I(T_H - T_C) + \frac{I^2 L_{p,n}}{\sigma_{p,n} A_{p,n}}. \tag{1.14}$$

Thus, the total power input is

$$W = W_p + W_n = (S_p - S_n)I(T_H - T_C) + I^2R, \tag{1.15}$$

and the thermoelectric coefficient of performance, ϕ, is

$$\phi \equiv \frac{q_C}{W} = \frac{(S_p - S_n)IT_C - \frac{1}{2}I^2R - K(T_H - T_C)}{(S_p - S_n)I(T_H - T_C) + I^2R}. \tag{1.16}$$

The thermoelectric coefficient of performance depends on the current I. Two cases are of special interest, the current I_q for maximum cooling power and the current I_ϕ for maximum coefficient of performance.

We determine I_q for maximum cooling power by setting $dq_C/dI = 0$ in Eq. (1.11), and find that

$$I_q = \frac{(S_p - S_n)T_C}{R}, \tag{1.17}$$

[4]Note that in the first term on the right hand side, $S_p > 0$ and $S_n < 0$ so that both p-branch and n-branch have positive contributions to the cooling power.

with the corresponding coefficient of performance given by

$$\phi_q = \frac{\frac{1}{2}ZT_C - (T_H/T_C - 1)}{ZT_H}, \tag{1.18}$$

where[5]

$$Z = \frac{(S_p - S_n)^2}{KR}. \tag{1.19}$$

If the heat source is removed, the coefficient of performance falls to zero and the temperature difference $(T_H - T_C)$ rises to its maximum value

$$(T_H - T_C)_{\max} = \frac{1}{2}ZT_C^2. \tag{1.20}$$

The current I_ϕ for maximum coefficient of performance is found by setting $d\phi/dI = 0$ in Eq. (1.16), so

$$I_\phi = \frac{(S_p - S_n)(T_H - T_C)}{R(\sqrt{1 + ZT_M} - 1)}, \tag{1.21}$$

where $T_M = \frac{1}{2}(T_H + T_C)$ is the mean temperature. The maximum coefficient of performance is

$$\phi_{\max} = \frac{T_C(\sqrt{1 + ZT_M} - T_H/T_C)}{(T_H - T_C)(\sqrt{1 + ZT_M} + 1)}. \tag{1.22}$$

Since the quantity Z determines both the maximum temperature difference and the maximum coefficient of performance, it is called the figure of merit of the thermoelectric device. It is easy to see in Eqs. (1.18), (1.20) and (1.22) that $(T_H - T_C)_{\max}$, ϕ_q and $\phi_{\max}$ are all monotonically increasing functions of Z as long as $T_H > T_C$, and $\phi_{\max}$ in Eq. (1.22) renders the value of the Carnot coefficient of performance

$$\phi_{\text{Carnot}} = \frac{T_C}{T_H - T_C} \tag{1.23}$$

as $Z \to \infty$.

The figure of merit Z is not a fixed quantity for a given pair of thermoelectric materials but depends on the relative geometries of the branches. It has its maximum

[5]Note that $S_p > 0$ and $S_n < 0$.

value when the product RK in Eq. (1.19) is a minimum, which occurs when

$$\frac{L_p/A_p}{L_n/A_n} = \sqrt{\frac{\sigma_p \kappa_p}{\sigma_n \kappa_n}}. \tag{1.24}$$

When the dimensions are optimized, the figure of merit becomes[6]

$$Z = \frac{(S_p - S_n)^2}{[(\kappa_p/\sigma_p)^{1/2} + (\kappa_n/\sigma_n)^{1/2}]^2}. \tag{1.25}$$

Although the figure of merit Z of a cooling device depends on the properties of the materials in both branches, it is convenient to define a figure of merit for a single material, positive or negative, as

$$Z_{p,n} = \frac{S_{p,n}^2 \sigma_{p,n}}{\kappa_{p,n}}. \tag{1.26}$$

In practice, at most temperatures of interest, the properties of the materials for the positive and negative branches are comparable, so that

$$Z \simeq \frac{Z_p + Z_n}{2}. \tag{1.27}$$

The previous treatment assumes that the parameters S, σ and κ are independent of temperature. The errors that originate from this assumption are likely to be important for devices that are operated with large temperature differences between the source and sink. The basic differential equation for the problem of the temperature dependence of the parameters takes the form

$$\frac{d}{dx}\left[\kappa_{p,n}(T) A_{p,n} \frac{dT}{dx}\right] \pm IT \frac{dS_{p,n}(T)}{dT} \frac{dT}{dx} + \frac{I^2}{\sigma_{p,n}(T) A_{p,n}} = 0. \tag{1.28}$$

In general, the best that one can hope for is a numerical solution following the substitution of empirical temperature-dependences for the parameters. However, by taking

[6]Note that $S_p > 0$ and $S_n < 0$.

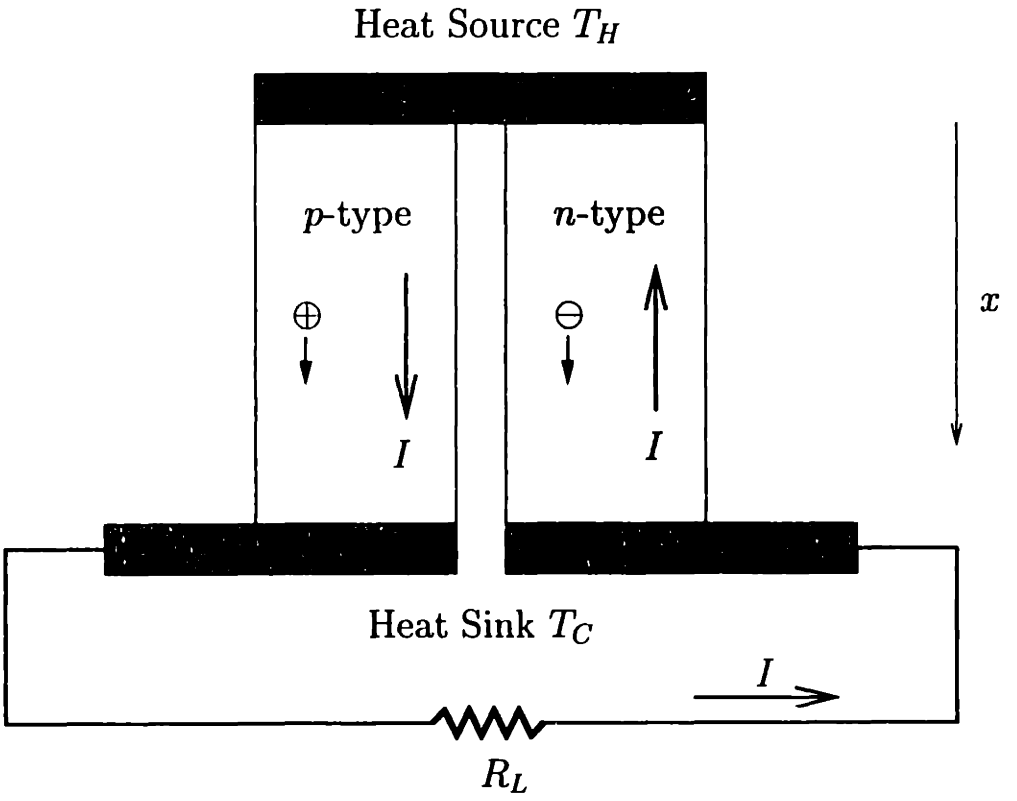

Figure 1-4: Simple thermoelectric power generator.

average values over the two branches, one finds [2]

$$Z \simeq \frac{< S_p - S_n >^2}{(< \kappa_p/\sigma_p >^{1/2} + < \kappa_n/\sigma_n >^{1/2})^2}, \tag{1.29}$$

where the angular brackets indicate temperature-averaged quantities. The numerical solution [21] of Eq. (1.28) indicates that this method gives an accuracy that is good enough for most purposes.

1.4 Thermoelectric power generation

The device shown in Fig. 1-3 can also be used as a thermoelectric power generator as shown in Fig. 1-4. Thermal energy is delivered from the heat source to the hot junction (T_H), and leaks from the cold junction (T_C) to the heat sink. Because the carriers, including both electrons and holes, in both branches thermally diffuse along

the $+x$ direction, an *emf* is generated in the device. The generated electrical energy is used to produce the current I through the resistor R_L and thereby provides work. The thermal efficiency η is defined as the ratio of the electrical power output to the thermal power input to the hot junction.

In a similar way that leads to Eq. (1.11), the thermal power input to the hot junction from the heat source is derived to be

$$q_H = (S_p - S_n)IT_H + K(T_H - T_C) - \frac{1}{2}I^2R, \tag{1.30}$$

where K and R are the geometry dependent thermal conductance and electrical resistance, respectively, of the device as in Eqs. (1.12) and (1.13). The electrical power output is

$$W = I^2R_L, \tag{1.31}$$

where R_L is the load resistance. The current I is given by[7]

$$I = \frac{(S_p - S_n)(T_H - T_C)}{R + R_L}, \tag{1.32}$$

since the open-circuit voltage is $(S_p - S_n)(T_H - T_C)$. Thus the thermal efficiency is

$$\eta \equiv \frac{W}{q_H} = \frac{I^2R_L}{(S_p - S_n)IT_H + K(T_H - T_C) - \frac{1}{2}I^2R}. \tag{1.33}$$

The thermal efficiency depends on the load resistance R_L. Two cases are of special interest, the load resistance for maximum power output and the load resistance for maximum thermal efficiency.

The load resistance which maximizes the power output is obtained by setting equal to zero the derivative with respect to the load resistance of the power output given by Eqs. (1.31) and (1.32). The result $R_L = R$ is obtained and the thermal efficiency

[7]Note that $S_p > 0$ and $S_n < 0$, therefore both p-branch and n-branch contribute to the current generation.

at maximum power output is found to be

$$\eta_W = \frac{2Z(T_H - T_C)}{Z(3T_H + T_C) + 8}, \tag{1.34}$$

where Z is the thermoelectric figure of merit of the device as defined in Eq. (1.19). The maximum thermal efficiency is found by setting $d\eta/dR_L = 0$ in Eq. (1.33) so that $R_L = \sqrt{ZT_M + 1}R$, and the maximum thermal efficiency is

$$\eta_{\max} = \frac{(T_H - T_C)(\sqrt{1 + ZT_M} - 1)}{T_H(\sqrt{1 + ZT_M} + T_C/T_H)}, \tag{1.35}$$

where $T_M = \frac{1}{2}(T_H + T_C)$ is the mean temperature. The thermoelectric figure of merit Z again determines the thermal efficiency, and it is easy to see that both η_W in Eq. (1.34) and $\eta_{\max}$ in Eq. (1.35) are monotonically increasing functions of Z as long as $T_H > T_C$, and $\eta_{\max}$ in Eq. (1.35) approaches the value of Carnot efficiency

$$\eta_{\text{Carnot}} = \frac{T_H - T_C}{T_H} \tag{1.36}$$

as $Z \to \infty$.

1.5 Good thermoelectric materials

To be a good thermoelectric material for cooling applications, the material must have a high thermoelectric figure of merit (see Eq. (1.26))

$$Z = \frac{S^2\sigma}{\kappa} \tag{1.37}$$

where S is the thermoelectric power (Seebeck coefficient), σ is the electrical conductivity, and κ is the thermal conductivity.

In order to achieve a high Z, one requires a high thermoelectric power S, a high electrical conductivity σ, and a low thermal conductivity κ. Present good thermoelectric materials are all semiconductors that have large impurity concentrations. The

reason for this can be explained by the curves in Fig. 1-5. The horizontal scale is the carrier concentration which is divided into four regions, which are insulators, semiconductors, semimetals, and metals, from the left to the right. The upper part of the figure shows three curves, which are S, σ, and κ, while the resulting thermoelectric figure of merit, ZT, is shown in the lower part. It is seen that the optimum thermoelectric figure of merit occurs in the region of the heavily doped semiconductors. Because of the Jonker pear [22] behavior of the Seebeck coefficient as the function of the carrier concentration, the value of S drops at the insulator end, and therefore a insulator is not a good thermoelectric material.

In principle, the difficulties of increasing Z relate to the following reasons: Increasing S for simple materials also leads to a simultaneous decrease in σ, and an increase in σ leads to a comparable increase in the electronic contribution to κ because of the Wiedemann-Franz law. So with known conventional solids, a limit is rapidly obtained where a modification to any one of the three parameters S, σ, or κ, adversely affects the other transport coefficients, so that the resulting Z does not vary significantly. Currently, the materials with the highest Z are Bi_2Te_3 alloys such as $Bi_{0.5}Sb_{1.5}Te_3$, with $ZT \simeq 1.0$ at $T = 300\,\mathrm{K}$.

In order to break this bottleneck for the enhancement of the thermoelectric figure of merit, we can take advantage of the enhanced density of states in low-dimensional transport systems. In general, increasing the chemical potential in the system by increasing the doping level will increase the electrical conductivity and decrease the Seebeck coefficient, and vise versa. As shown in Fig. 1-6, the density of states is enhanced in two-dimensional (2D) and one-dimensional (1D) systems. Therefore, we can hope to increase the electrical conductivity without decreasing the Seebeck coefficient, or increasing the Seebeck coefficient without decreasing the electrical conductivity in low-dimensional systems, resulting in a higher power factor $S^2\sigma$.[8]

Another favorable effect associated with quantum wells (2D) and quantum wires (1D) is that more interface scattering for phonons is introduced so that the lattice

[8]In practice, an optimal chemical potential is chosen to get the maximum thermoelectric figure of merit (see Chapters 3 and 4).

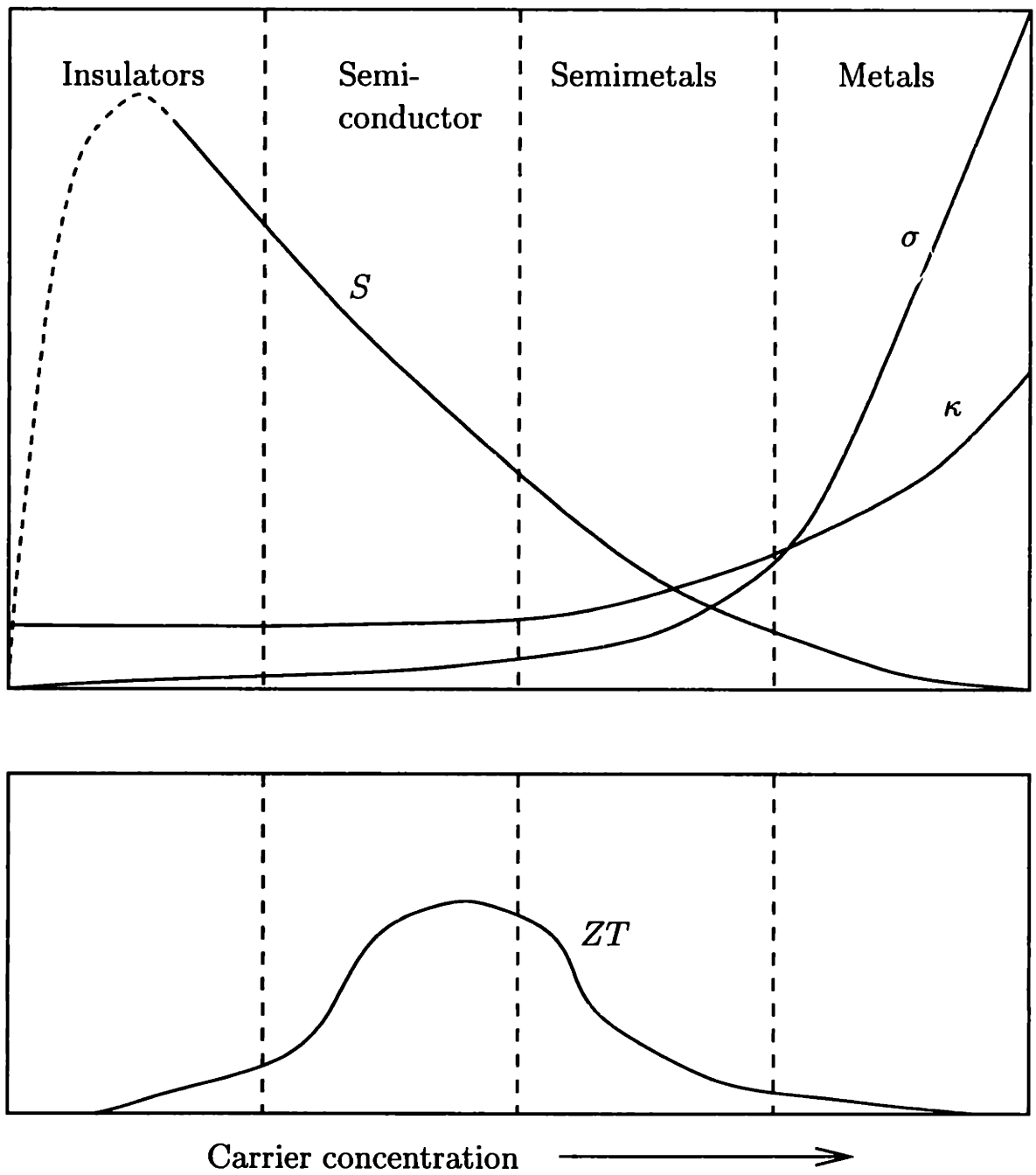

Figure 1-5: What materials can have high ZT?

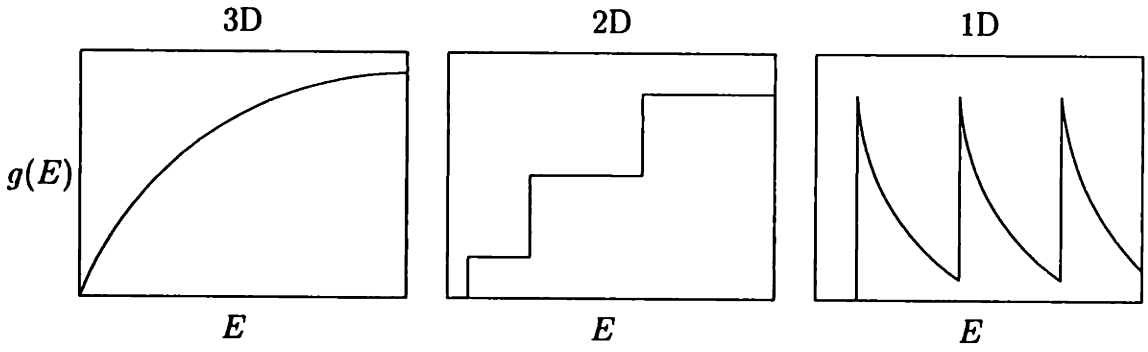

Figure 1-6: The density of states $g(E)$ for 3D, 2D and 1D systems.

thermal conductivity is reduced. This happens when the size of the quantum wells or quantum wires becomes smaller than the phonon mean free path.

It is important to notice that the device equations derived in Sections 1.3 and 1.4 have no assumptions on dimensionality. Therefore the same definition of the thermoelectric figure of merit applies for both 2D and 1D transport systems.

In this thesis, the $Si/Si_{1-x}Ge_x$ superlattice system is studied as an example of a 2D system. $Si_{1-x}Ge_x$ is a presently used as a 3D thermoelectric material for thermoelectric power generator for space applications in which $Si_{1-x}Ge_x$ is operated at elevated temperatures ($\sim$1000 K). My theoretical modeling shows that this system is also a potentially good thermoelectric material even at room temperature if it is made in 2D superlattice form (or also for 1D quantum wires). This finding has a great potential impact on the microelectronics industry which is based on Si technologies.

The second system I investigated in this thesis is the 1D bismuth quantum wire system. Bismuth in bulk form is a semimetal and is not a good thermoelectric material because of the cancellation between the electron and hole contributions to the Seebeck coefficient. However, quantum confinement effects can be introduced to achieve a semimetal-semiconductor transition so that by adjusting the chemical potential, the thermoelectric figure of merit can be greatly enhanced (Chapter 4). This system is potentially a good thermoelectric material at temperatures below 300 K.

1.6 The road map

Following this introductory chapter, the semiclassical transport theory is briefly reviewed based on Ref. [23], and an extension to the low dimensional transport is presented in the next chapter.

Chapter 3 consists of a detailed theoretical modeling of the thermoelectric properties for the $Si/Si_{1-x}Ge_x$ quantum well superlattice structures. Following a preliminary modeling of a single Si quantum well with a infinite barrier height, a detailed calculation is performed on an infinite series of Si quantum wells and $Si_{1-x}Ge_x$ barriers with a finite potential height. A temperature dependent study suggests favorable thermoelectric performance of the $Si/Si_{1-x}Ge_x$ quantum well superlattice structures at elevated temperatures. The effect of the barrier layers is briefly discussed. A strategy for improving the quantum confinement and high temperature performance by introducing wide band gap materials within the barrier layers through δ-doping is also proposed.

Chapter 4 presents the theoretical modeling of the bismuth quantum wire system. After a simplified model considering a parabolic band structure is discussed, a more detailed and more realistic theoretical modeling is performed, based on the non-parabolic band structure and the temperature dependent band structure parameters of Bi. The thermoelectric transport coefficients are calculated for Bi quantum wires oriented along the three principal crystallographic directions. A detailed temperature dependent study is also presented.

Chapter 5 consists of the experimental investigations. A transport measurement system is designed and constructed. The characterization of the thermoelectric power factor is performed on $PbTe/Pb_{1-x}Eu_xTe$ and $Si/Si_{1-x}Ge_x$ superlattices. The experimental results are compared with theoretical predictions, and good agreement is achieved with *no* adjustable parameters in theory. Some preliminary experimental characterizations of Bi nanowire arrays are also reported.

The last chapter of the thesis provides some suggestions for possible future research activities base on the work presented in this thesis.

Chapter 2

Basic transport theory for thermoelectricity

The semiclassical transport theory is briefly reviewed based on Ref. [23], and an extension to the low dimensional transport is presented in this chapter.

2.1 The semiclassical model

The semiclassical model predicts how, in the absence of collisions, the position $\mathbf{r}$ and the wave vector $\mathbf{k}$ of each electron evolve in the presence of external fields based on the band structure $\varepsilon_n(\mathbf{k})$. In the course of time, the variables $\mathbf{r}$, $\mathbf{k}$, and n evolve according to the following rules:

1. The band index n is a constant of motion. The semiclassical model does not consider the possibility of inter-band transitions.

2. The semiclassical equations of motion[1]

$$\dot{\mathbf{r}} = \mathbf{v}_n(\mathbf{k}) = \frac{1}{\hbar}\frac{\partial \varepsilon_n(\mathbf{k})}{\partial \mathbf{k}}, \tag{2.1}$$

[1] In this chapter, all equations are derived for electrons. For holes, a positive charge $+e$ should be used instead of $-e$.

$$\hbar\dot{\mathbf{k}} = -e\left[\mathbf{E}(\mathbf{r},t) + \frac{1}{c}\mathbf{v}_n(\mathbf{k}) \times \mathbf{H}(\mathbf{r},t)\right]. \tag{2.2}$$

3. All distinct wave vectors for a single band lie in a single primitive unit cell of the reciprocal lattice.

2.2 The relaxation-time approximation

A non-equilibrium distribution function $g_n(\mathbf{r},\mathbf{k},t)$ is defined so that $g_n(\mathbf{r},\mathbf{k},t)d\mathbf{r}d\mathbf{k}/4\pi^3$ is the number of electrons in the nth band at time t in the semiclassical phase space volume $d\mathbf{r}d\mathbf{k}$ about the point $\mathbf{r}$, $\mathbf{k}$. The relaxation-time approximation assumes that the distribution of those electrons $dg_n(\mathbf{r},\mathbf{k},t)$ that emerge from collisions into band n with wave vector $\mathbf{k}$ at position $\mathbf{r}$ during the time interval dt is given by

$$dg_n(\mathbf{r},\mathbf{k},t) = \frac{dt}{\tau_n(\mathbf{r},\mathbf{k})} g_n^0(\mathbf{r},\mathbf{k}), \tag{2.3}$$

where $\tau_n(\mathbf{r},\mathbf{k})$ is defined as the relaxation time, and $g_n^0(\mathbf{r},\mathbf{k})$ is the equilibrium distribution function appropriate to a local temperature $T(\mathbf{r})$ and a local chemical potential $\zeta(\mathbf{r})$,

$$g_n^0(\mathbf{r},\mathbf{k}) \equiv f(\varepsilon_n(\mathbf{k})) = \frac{1}{e^{(\varepsilon_n(\mathbf{k})-\zeta(\mathbf{r}))/k_BT(\mathbf{r})}+1}. \tag{2.4}$$

With this assumption, we can calculate the non-equilibrium distribution function in the presence of external electric fields and temperature gradients.

2.3 Calculation of the non-equilibrium distribution function

Consider collisions at time $t' < t$ about $\mathbf{r}_n(t')$, $\mathbf{k}_n(t')$, where $\mathbf{r}_n(t')$, $\mathbf{k}_n(t')$ are the solutions to the semiclassical equations of motion (Eqs. (2.1) and (2.2)) for the nth band that passes through the point $\mathbf{r}$, $\mathbf{k}$ in phase space, only a fraction $P_n(\mathbf{r},\mathbf{k},t;t')$ of the electrons actually follow the equations of motion during the time between t' and t to arrive the point $\mathbf{r}$, $\mathbf{k}$, the others being scattered off that trajectory in phase

space. Using the relaxation-time approximation, the distribution function $g_n(\mathbf{r}, \mathbf{k}, t)$ can be calculated by integrating Eq. (2.3) over t' after multiplying the right hand side by $P_n(\mathbf{r}, \mathbf{k}, t; t')$,

$$g(t) = \int_{-\infty}^{t} \frac{dt'}{\tau(t')} g^0(t') P(t, t'), \tag{2.5}$$

where we have left the variables $\mathbf{r}$, $\mathbf{k}$, and n to be temporarily implicit.

The fraction of electrons that survive collisions from t' to t is less than the fraction that survive from $t' + dt'$ to t by the factor $[1 - dt'/\tau(t')]$, so that

$$P(t, t') = P(t, t' + dt') \left[1 - \frac{dt'}{\tau(t')}\right]. \tag{2.6}$$

In the limit as $dt' \to 0$, this gives the differential equation

$$\frac{\partial}{\partial t'} P(t, t') = \frac{P(t, t')}{\tau(t')}, \tag{2.7}$$

which can be used to integrate Eq. (2.5) by parts, giving

$$g(t) = g^0(t) - \int_{-\infty}^{t} dt' P(t, t') \frac{d}{dt'} g^0(t'), \tag{2.8}$$

where we have used the boundary conditions $P(t, -\infty) = 0$ and $P(t, t) = 1$.

To evaluate the time derivative of g^0, note that g^0 in Eq. (2.4) depends on time only through $\varepsilon_n(\mathbf{k}_n(t'))$, $T(\mathbf{r}_n(t'))$, and $\zeta(\mathbf{r}_n(t'))$, so that

$$\frac{dg^0(t')}{dt'} = \frac{\partial g^0}{\partial \varepsilon_n} \frac{\partial \varepsilon_n}{\partial \mathbf{k}} \cdot \frac{d\mathbf{k}_n}{dt'} + \frac{\partial g^0}{\partial T} \frac{\partial T}{\partial \mathbf{r}} \cdot \frac{d\mathbf{r}_n}{dt'} + \frac{\partial g^0}{\partial \zeta} \frac{\partial \zeta}{\partial \mathbf{r}} \cdot \frac{d\mathbf{r}_n}{dt'}. \tag{2.9}$$

If we use semiclassical equations of motion Eqs. (2.1) and (2.2) in Eq. (2.9), then Eq. (2.8) becomes

$$g(t) = g^0 + \int_{-\infty}^{t} dt' P(t, t') \left[\left(-\frac{\partial f}{\partial \varepsilon} \right) \mathbf{v} \cdot \left(-e\mathbf{E} - \boldsymbol{\nabla} \zeta - \left(\frac{\varepsilon - \zeta}{T} \right) \boldsymbol{\nabla} T \right) \right], \tag{2.10}$$

where f is the Fermi function (Eq. (2.4)), and all the quantities in the brackets depend on t' through their arguments $\mathbf{r}_n(t')$ and $\mathbf{k}_n(t')$. Note that magnetic field $\mathbf{H}$ does not

appear in Eq. (2.10) since the Lorentz force is perpendicular to $\mathbf{v}$.

2.4 Thermoelectric transport coefficients

Since carrier density in the reciprocal space volume element $d\mathbf{k}$ is $g(\mathbf{k})d\mathbf{k}/4\pi^3$, the current density in a band is

$$\mathbf{j} = -e\sum_n \int \frac{d\mathbf{k}}{4\pi^3}\mathbf{v}_n(\mathbf{k})g_n(\mathbf{k}). \tag{2.11}$$

Each partially filled band makes a contribution to the current density; the total current density is the sum of these contributions over all bands.

Analogously, consider a small fixed region of the solid within which the temperature is effectively constant. The rate at which heat appears in the region is just T times the rate at which the entropy of the electrons within the region changes ($dQ = TdS$). Thus the thermal current density is related to the entropy current density $\mathbf{j}^s$ by

$$\mathbf{j}^q = T\mathbf{j}^s. \tag{2.12}$$

Since the volume of the region is fixed, changes in the entropy in the region are related to changes in the internal energy and number of electrons by the thermodynamic identity

$$TdS = dU - \zeta dN, \tag{2.13}$$

or, in terms of current densities,

$$T\mathbf{j}^s = \mathbf{j}^e - \zeta\mathbf{j}^n \tag{2.14}$$

where the energy and number current densities are[2]

$$\left\{ \begin{array}{c} \mathbf{j}^{\varepsilon} \\ \mathbf{j}^{n} \end{array} \right\} = \sum_{n} \int \frac{d\mathbf{k}}{4\pi^3} \left\{ \begin{array}{c} \varepsilon_n(\mathbf{k}) \\ 1 \end{array} \right\} \mathbf{v}_n(\mathbf{k}) g_n(\mathbf{k}). \tag{2.15}$$

Substituting for $\mathbf{j}^{\varepsilon}$ and $\mathbf{j}^{n}$ in Eq. (2.14), we find a thermal current density

$$\mathbf{j}^{q} = \sum_{n} \int \frac{d\mathbf{k}}{4\pi^3} \left[\varepsilon_n(\mathbf{k}) - \zeta\right] \mathbf{v}_n(\mathbf{k}) g_n(\mathbf{k}). \tag{2.16}$$

For thermoelectric transport, we can assume a time-independent, uniform weak electric field and temperature gradient, and a zero magnetic field. In this case, we can further assume a position-independent relaxation time so that the solution to Eq. (2.7) is

$$P(t, t') = e^{-(t-t')/\tau_n(\mathbf{k})}. \tag{2.17}$$

Thus, Equation (2.10) can be integrated to give

$$g(\mathbf{k}) = g^0(\mathbf{k}) + \tau(\mathbf{k}) \left(-\frac{\partial f}{\partial \varepsilon}\right) \mathbf{v}(\mathbf{k}) \cdot \left[-e\left(\mathbf{E} + \frac{\nabla\zeta}{e}\right) + \frac{\varepsilon(\mathbf{k}) - \zeta}{T}(-\nabla T)\right]. \tag{2.18}$$

We can construct the electrical current density Eq. (2.11) and the thermal current density Eq. (2.16) from this distribution function:

$$\mathbf{j} = \mathbf{L}^{11} \cdot \left(\mathbf{E} + \frac{\nabla\zeta}{e}\right) + \mathbf{L}^{12} \cdot (-\nabla T), \tag{2.19}$$

$$\mathbf{j}^{q} = \mathbf{L}^{21} \cdot \left(\mathbf{E} + \frac{\nabla\zeta}{e}\right) + \mathbf{L}^{22} \cdot (-\nabla T), \tag{2.20}$$

where $\mathbf{L}^{ij}$ are defined in terms of the second rank symmetric tensors

$$\mathcal{L}^{(\alpha)} = e^2 \sum_{n} \int \frac{d\mathbf{k}}{4\pi^3} \left(-\frac{\partial f}{\partial \varepsilon}\right) \tau_n(\mathbf{k}) \mathbf{v}_n(\mathbf{k}) \mathbf{v}_n(\mathbf{k}) (\varepsilon_n(\mathbf{k}) - \zeta)^{\alpha} \tag{2.21}$$

[2]Note that $\mathbf{j} = -e\mathbf{j}^{n}$, and also we must be careful not to confuse the superscript n, indicating that $\mathbf{j}^{n}$ is the number current density, with the band index n.

by

$$\begin{aligned} \mathbf{L}^{11} &= \boldsymbol{\mathcal{L}}^{(0)}, \\ \mathbf{L}^{21} &= T\mathbf{L}^{12} = -\frac{1}{e}\boldsymbol{\mathcal{L}}^{(1)}, \\ \mathbf{L}^{22} &= \frac{1}{e^2T}\boldsymbol{\mathcal{L}}^{(2)}. \end{aligned} \tag{2.22}$$

Equations (2.19) and (2.20) can be used to deduce the thermoelectric transport coefficients.

2.4.1 DC electrical conductivity

When there is only a static electric field present in the solid, Eq. (2.19) reduces to Ohm's Law $\mathbf{j} = \boldsymbol{\sigma} \cdot \mathbf{E}$, where the conductivity tensor $\boldsymbol{\sigma}$ becomes

$$\boldsymbol{\sigma} = \mathbf{L}^{11} = \boldsymbol{\mathcal{L}}^{(0)}. \tag{2.23}$$

2.4.2 Seebeck coefficient

While measuring the Seebeck coefficient (Fig. 1-1), an ideal voltmeter is used so that $\mathbf{j} \to 0$. Thus, Eq. (2.19) becomes

$$\mathbf{E} + \frac{\boldsymbol{\nabla}\zeta}{e} = (\mathbf{L}^{11})^{-1} \cdot \mathbf{L}^{12} \cdot (\boldsymbol{\nabla}T). \tag{2.24}$$

We need to keep in mind that the voltmeter is driven not just by the electric field $\mathbf{E}$, but by $\mathbf{E} + (1/e)\boldsymbol{\nabla}\zeta$, because the chemical potential gradient leads to a diffusion potential, in addition to the electric field. Therefore, the Seebeck coefficient tensor (Eq. (1.1)) is

$$\mathbf{S} = (\mathbf{L}^{11})^{-1} \cdot \mathbf{L}^{12} = -\left(\frac{1}{eT}\right)(\boldsymbol{\mathcal{L}}^{(0)})^{-1} \cdot \boldsymbol{\mathcal{L}}^{(1)}. \tag{2.25}$$

2.4.3 Electronic thermal conductivity

To deduce the electronic thermal conductivity $\boldsymbol{\kappa}_e$, we note that it relates the thermal current to the temperature gradient under conditions in which no electric current flows. Substituting Eq. (2.24) into Eq. (2.20), we find that

$$\mathbf{j}^q = \boldsymbol{\kappa}_e \cdot (-\boldsymbol{\nabla} T), \tag{2.26}$$

where $\boldsymbol{\kappa}$, the electronic thermal conductivity tensor (a second rank symmetric tensor), is given by

$$\boldsymbol{\kappa}_e = \mathbf{L}^{22} - \mathbf{L}^{21} \cdot (\mathbf{L}^{11})^{-1} \cdot \mathbf{L}^{12} = \left(\frac{1}{e^2 T}\right) (\boldsymbol{\mathcal{L}}^{(2)} - \boldsymbol{\mathcal{L}}^{(1)} \cdot (\boldsymbol{\mathcal{L}}^{(0)})^{-1} \cdot \boldsymbol{\mathcal{L}}^{(1)}). \tag{2.27}$$

2.5 Low dimensional thermoelectricity

In summary, all the thermoelectric transport coefficients, which are in general all tensors, can be calculated by

$$\boldsymbol{\sigma} = \boldsymbol{\mathcal{L}}^{(0)}, \tag{2.28}$$

$$\mathbf{S} = -\left(\frac{1}{eT}\right) (\boldsymbol{\mathcal{L}}^{(0)})^{-1} \cdot \boldsymbol{\mathcal{L}}^{(1)}, \tag{2.29}$$

$$\boldsymbol{\kappa}_e = \left(\frac{1}{e^2 T}\right) (\boldsymbol{\mathcal{L}}^{(2)} - \boldsymbol{\mathcal{L}}^{(1)} \cdot (\boldsymbol{\mathcal{L}}^{(0)})^{-1} \cdot \boldsymbol{\mathcal{L}}^{(1)}), \tag{2.30}$$

where

$$\boldsymbol{\mathcal{L}}^{(\alpha)} = e^2 \sum_n \int \frac{d^3k}{4\pi^3} \left(-\frac{\partial f}{\partial \varepsilon}\right) \tau_n(\mathbf{k}) \mathbf{v}_n(\mathbf{k}) \mathbf{v}_n(\mathbf{k}) (\varepsilon_n(\mathbf{k}) - \zeta)^\alpha. \tag{2.31}$$

Note that we have replaced $d\mathbf{k}$ by d^3k to indicate explicitly that the integration is over a three-dimensional k-space.

In the previous sections, we have derived these transport quantities semiclassically without any assumption about dimensionality except using a three-dimensional density of states $d^3k/4\pi^3$. Therefore, it is straightforward to extend the theory into low dimensional transport by just replacing the density of states by appropriate forms.

In case of a two-dimensional (2D) system, the density of states becomes $d^2k/2\pi^2 a$,

where a is the thickness of the quantum well, so that

$$\mathcal{L}_{2D}^{(\alpha)} = e^2 \sum_{n,\nu} \int \frac{d^2k}{2\pi^2 a} \left(-\frac{\partial f}{\partial \varepsilon} \right) \tau_{n,\nu}(\mathbf{k}) \mathbf{v}_{n,\nu}(\mathbf{k}) \mathbf{v}_{n,\nu}(\mathbf{k}) (\varepsilon_{n,\nu}(\mathbf{k}) - \zeta)^{\alpha}, \tag{2.32}$$

where the index ν is the subband index.

Similarly, with the one-dimensional (1D) density of states $dk/\pi a^2$, where a is the quantum wire thickness, we have

$$\mathcal{L}_{1D}^{(\alpha)} = e^2 \sum_{n,\nu} \int \frac{dk}{\pi a^2} \left(-\frac{\partial f}{\partial \varepsilon} \right) \tau_{n,\nu}(\mathbf{k}) \mathbf{v}_{n,\nu}(\mathbf{k}) \mathbf{v}_{n,\nu}(\mathbf{k}) (\varepsilon_{n,\nu}(\mathbf{k}) - \zeta)^{\alpha}. \tag{2.33}$$

Although we have written the $\mathcal{L}^{(\alpha)}$ tensors for 2D and 1D systems in Eqs. (2.32) and (2.33) in the same tensor form as in the 3D case, the $\mathcal{L}^{(\alpha)}$ tensors are actually reduced to lower dimensionalities. Especially, the $\mathcal{L}^{(\alpha)}$ tensors reduce to scalars, because the velocity vector $\mathbf{v}_{n,\nu}$ is confined on the axis determined by the transport direction and becomes a scalar. In this case, the anisotropy of the material is handled by the quantum confinement of the anisotropic band structures, as shown in Chapter 3 for the case of $Si/Si_{1-x}Ge_x$ quantum wells and in Chapter 4 for the case of Bi quantum wires.

Chapter 3

The $Si/Si_{1-x}Ge_x$ quantum well system

The study of $Si_{1-x}Ge_x$ alloys as possible materials for thermoelectric generators was undertaken as early as 1954 by Ioffe and Ioffe [24]. In bulk form, $Si_{1-x}Ge_x$ is a promising thermoelectric material for high temperature ($\sim 1000\,K$) applications [25–27]. It was first used in space in the SNAP-10A nuclear reactor and has been the exclusive choice for radioisotope thermoelectric generators (RTGs) launched by the U.S. since 1976 [28]. In addition to having attractive thermoelectric and physical properties, $Si_{1-x}Ge_x$ devices can operate at temperatures up to about 1300 K without significant degradation.

The $Si/Si_{1-x}Ge_x$ quantum well system is interesting for thermoelectric studies because it is not only an excellent system for demonstrating proof-of-principle, but also has the potential for use in thermoelectric device applications. By carefully designing the $Si/Si_{1-x}Ge_x$ superlattice structures, we expect this system to have sufficiently good thermoelectric performance to be interesting for possible device applications at room temperature and above, which could have a potentially important impact on the Si-based microelectronics industry.

3.1 Si properties and research strategies

Si crystallizes in the diamond structure. The conduction band is characterized by six minima at equivalent Δ-points located at $(2\pi/a)(0.85, 0, 0)$ along the $\langle 100 \rangle$-axes of the Brillouin zone, as shown in Fig. 3-1. The surfaces of constant energy for n-type Si are ellipsoids of revolution with their major axes along $\langle 100 \rangle$, as shown in Fig. 3-2. Each ellipsoid is characterized by its transverse and longitudinal effective masses, which are $m_\perp = 0.1905\, m_0$ and $m_{||} = 0.9163\, m_0$, respectively, where m_0 is the free electron mass. In Fig. 3-2, the carrier pockets are labelled with a, b, c, d, e, and f, which is convenient in discussing the anisotropy in the presence of quantum confinement. The electron mobility at room temperature for bulk Si is $\mu_n = 1447\,\mathrm{cm^2\,V^{-1}\,s^{-1}}$. The bulk phonon thermal conductivity is $\kappa_{ph} = 1.313\,\mathrm{W\,cm^{-1}\,K^{-1}}$ at 300 K [29]. The maximum thermoelectric figure of merit for bulk Si at its optimal doping level at room temperature is calculated to be $Z_{3D}T = 0.014$ [5, 11] using the formalism derived in Section 2.4.

In this thesis, I concentrate on the investigation of the thermoelectricity of this system based on n-type quantum wells for the following reasons. First of all, n-type Si has six anisotropic (roughly 4.5:1) carrier pockets at the Δ-point, while p-type Si has only one isotropic carrier pocket at the Γ-point as shown in Fig. 3-1. Secondly, the mobility of holes, $\mu_p = 480\,\mathrm{cm^2\,V^{-1}\,s^{-1}}$, is much lower than that of electrons. Therefore, n-type Si is much more promising in getting a high thermoelectric figure of merit compared to its p-type counterpart.[1]

However, it is relatively difficult to get quantum confinement in the Si layer in the conduction band for $Si/Si_{1-x}Ge_x$ superlattices. $Si_{1-x}Ge_x$ forms a continuous series of solid solutions with gradually varying Ge concentration x, which can vary from 0 to 1. The indirect band gap $E_{g,ind}$ between the conduction band extremum at the Δ-points and the valence band extrema at the Γ-point decreases with x up to a value 0.85 [30]. Therefore, in $Si/Si_{1-x}Ge_x$ quantum well superlattices grown on a Si substrate, the

[1] However, for thermoelectric device applications, both n-type and p-type structures are needed. The investigation of p-type structures forms one of our next phase research activities (see Chapter 6).

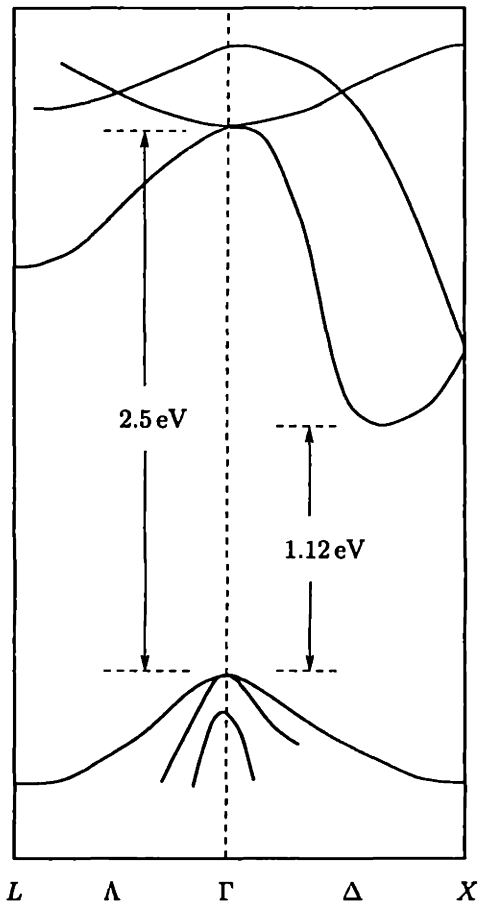

Figure 3-1: The electronic band structure of Si. The conduction band minima are at the six Δ-points equivalent to $(2\pi/a)(0.85, 0, 0)$.

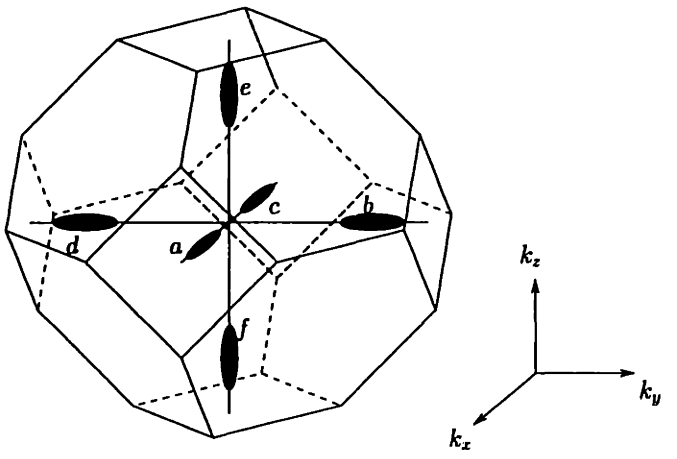

Figure 3-2: The six symmetry-related carrier pockets of n-type Si in its Brillouin zone. The long axes are directed along $\langle 100 \rangle$ directions. The six pockets are labeled with a, b, c, d, e, and f.

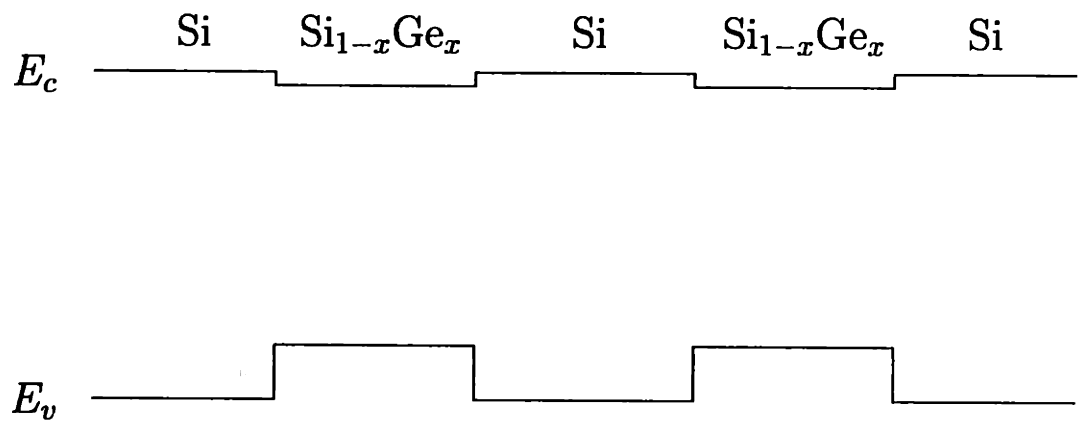

Figure 3-3: Schematic band edge diagram of a type I $Si/Si_{1-x}Ge_x$ quantum well superlattice grown on a Si substrate.

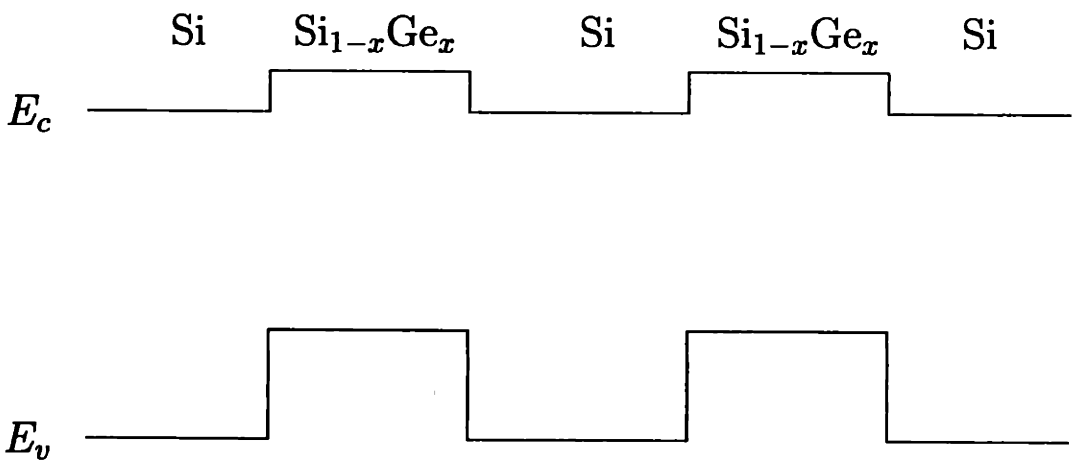

Figure 3-4: Schematic band edge diagram of a type II $Si/Si_{1-x}Ge_x$ quantum well superlattice grown on relaxed $Si_{1-x}Ge_x$.

band structure forms a type I alignment, as shown in Fig. 3-3.

In order to form quantum wells for electrons inside the Si layers, a superlattice structure with type II band alignment (Fig. 3-4) has to be fabricated. This is achieved by growing a relaxed $Si_{1-x}Ge_x$ buffer layer on top of the Si substrate. The relaxed $Si_{1-x}Ge_x$ buffer layer effectively increase the lattice constant of the substrate so that it is slightly larger than that of Si. The subsequent Si layers are therefore under tensile strain. Due to the tensile strain in the Si layers, quantum wells are formed for electrons in the conduction band inside the Si layers [31–33].

3.2 Thermoelectric figure of merit for a 2D quantum well for a single band

In this section, expressions for S, σ, κ_e and Z are derived for transport in a 2D quantum well for a single band. Let the quantum well layer be parallel to the x-y plane and the current flow in the x-direction. The general expressions for σ, S and κ_e given by Eqs. (2.28)-(2.30) can be applied to the 2D system with the transport tensor elements (Eq. (2.32))

$$\mathcal{L}^{(\alpha)} = e^2 \int \frac{d^2k}{2\pi^2 a} \left(-\frac{\partial f}{\partial \varepsilon}\right) \tau(\mathbf{k})\mathbf{v}(\mathbf{k})\mathbf{v}(\mathbf{k})(\varepsilon(\mathbf{k}) - \zeta)^{\alpha}. \tag{3.1}$$

The electronic dispersion relation used for the 2D electrons is

$$\varepsilon(k_x, k_y) = \varepsilon_{\nu}^{(0)} + \frac{\hbar^2 k_x^2}{2m_x} + \frac{\hbar^2 k_y^2}{2m_y}, \tag{3.2}$$

indicating free electron-like motion in the x-y plane, where $\varepsilon_{\nu}^{(0)}$ is the band edge of the ν^{th} subband under consideration, which for an infinite potential well is $\hbar^2\pi^2\nu^2/2m_z a^2$. Using

$$\mathbf{v}(\mathbf{k}) \left(-\frac{\partial f}{\partial \varepsilon}\right) = -\frac{1}{\hbar}\frac{\partial}{\partial \mathbf{k}} f(\varepsilon(\mathbf{k})), \tag{3.3}$$

we can integrate Eq. (3.1) by parts to get[2]

$$\mathcal{L}^{(\alpha)} = \frac{e^2\tau}{2\pi^2 a\hbar}\int d^2k \left\{\frac{\partial}{\partial \mathbf{k}}\left[\mathbf{v}(\mathbf{k})(\varepsilon(\mathbf{k})-\zeta)^{\alpha}\right]\right\} f(\varepsilon(\mathbf{k})). \tag{3.4}$$

To get the thermoelectric transport coefficient along the x-direction, we only need to calculate the xx component of the $\mathcal{L}^{(\alpha)}$ tensor. Using $v_x = \hbar k_x/2m_x$ (Eq. (2.2)), the transport tensor components in Eq. (3.1) can be calculated as

$$\mathcal{L}_{xx}^{(0)} = D_x[F_0], \tag{3.5}$$

$$\mathcal{L}_{xx}^{(1)} = D_x(k_BT)[2F_1 - \zeta^* F_0], \tag{3.6}$$

$$\mathcal{L}_{xx}^{(2)} = D_x(k_BT)^2[3F_2 - 4\zeta^* F_1 + \zeta^{*2} F_0], \tag{3.7}$$

where $\zeta^* = \zeta/k_BT$ is the reduced chemical potential. The quantity D_x which depends on the band parameters of the material is given by

$$D_x = \frac{e^2\tau}{\pi a}\left(\frac{k_BT}{\hbar^2}\right)\left(\frac{m_y}{m_x}\right)^{\frac{1}{2}}, \tag{3.8}$$

and the Fermi-Dirac related function F_i (for $i = 0, 1, 2, \ldots$) is given by

$$F_i = F_i(\zeta^*) = \int_0^\infty \frac{x^i\, dx}{e^{(x-\zeta^*)}+1}. \tag{3.9}$$

Equations (2.28)-(2.30) can now be used to calculate the electrical conductivity σ, the Seebeck coefficient S, and the electronic contribution to the thermal conductivity κ_e:

$$\sigma = \frac{e}{\pi a}\left(\frac{k_BT}{\hbar^2}\right)(m_x m_y)^{\frac{1}{2}}\mu_x(F_0), \tag{3.10}$$

$$S = -\frac{k_B}{e}\left(\frac{2F_1}{F_0} - \zeta^*\right), \tag{3.11}$$

$$\kappa_e = \frac{k_B^2T}{\pi a e}\left(\frac{k_BT}{\hbar^2}\right)(m_x m_y)^{\frac{1}{2}}\mu_x\left(3F_2 - \frac{4F_1^2}{F_0}\right), \tag{3.12}$$

[2]Here we have assumed a constant relaxation time τ. This is a reasonable assumption because $(-\partial f/\partial\varepsilon) \simeq \delta(\varepsilon - \varepsilon_F)$ in most cases of interest.

where the mobility is given by $\mu_x = e\tau/m_x$.

Using

$$Z = \frac{S^2\sigma}{\kappa_e + \kappa_{ph}}, \tag{3.13}$$

where κ_{ph} is the phonon thermal conductivity, gives

$$Z_{2D}T = \frac{\left(\frac{2F_1}{F_0} - \zeta^*\right)^2 F_0}{\frac{1}{B_{2D}} + 3F_2 - \frac{4F_1^2}{F_0}}, \tag{3.14}$$

where the dimensionless quantity B_{2D} is given by

$$B_{2D} = \frac{1}{\pi a}\left(\frac{k_B T}{\hbar^2}\right)(m_x m_y)^{\frac{1}{2}} \frac{k_B^2 T \mu_x}{e\kappa_{ph}}. \tag{3.15}$$

For a specific value of the quantity B_{2D}, $Z_{2D}T$ can be optimized by changing the chemical potential in the system. The higher the B_{2D} value, the higher is the optimal $Z_{2D}T$ value [5]. Therefore, the quantity B_{2D} gives a guideline for selecting good thermoelectric materials and designing optimum structures.

3.3 Si quantum wells with infinite barrier height

To begin with, I first calculate the thermoelectric figure of merit for Si quantum wells with infinite barrier height. Let the quantum well be parallel to the x-y plane and the current flow in the x direction. In the $Si/Si_{1-x}Ge_x$ quantum well structures we have investigated, the samples are grown along the [100] direction and the transport measurements are performed along the principal directions of each of the six ellipsoids in the conduction band. By assuming that the conduction band is parabolic and that the electrons occupy only the lowest ($n = 1$) sub-band of the quantum well, the electronic dispersion relation is

$$\varepsilon(k_x, k_y) = \frac{\hbar^2 k_x^2}{2m_x} + \frac{\hbar^2 k_y^2}{2m_y} + \frac{\hbar^2 \pi^2}{2m_z a^2}, \tag{3.16}$$

where a is the width of the quantum well. The two-dimensional thermoelectric figure of merit can be calculated using Eq. (3.14). However, because there are six anisotropic electron carrier pockets along the $\langle 100 \rangle$ directions in the Brillouin zone, the effect of anisotropy and the contributions from all six carrier pockets need to be considered. Therefore, the value of B_{2D} in Eq. (3.14) becomes

$$B_{2D} = \frac{1}{\pi a}\left(\frac{k_B T}{\hbar^2}\right)\frac{k_B^2 T \tau \alpha}{\kappa_{ph}}, \tag{3.17}$$

where in the case of Si quantum wells

$$\alpha = 2\left(\frac{m_{\|}}{m_{\perp}}\right)^{\frac{1}{2}} + 2\left(\frac{m_{\perp}}{m_{\|}}\right)^{\frac{1}{2}} + 2, \tag{3.18}$$

accounting for the anisotropy of the six different ellipsoids in the Si conduction band, in which $m_{\perp}$ and $m_{\|}$ are, respectively, the transverse and longitudinal effective mass components of electrons in the conduction band, and τ is the relaxation time[3] determined by [34]

$$\tau = \frac{3\mu_n}{e\left(\frac{1}{m_{\|}} + \frac{2}{m_{\perp}}\right)}, \tag{3.19}$$

where μ_n is the measured electron mobility. The existence of the α factor in B_{2D} reflects the number of carrier pockets so that it is desirable to have many carrier pockets to get high ZT values. Also, the form of α shown in Eq. (3.18) indicates that a large anisotropy in the Fermi surface gives a value of α greater than the number of carrier pockets. In case of n-type Si, the value of α is 7.19, which is greater than 6. Therefore, materials with high anisotropy in the Fermi surface have a greater potential of being good thermoelectric materials.

The value B_{2D} in Eq. (3.17) is determined by the intrinsic properties of Si and the width of the quantum well. For a given value of B_{2D}, the reduced chemical potential ζ^* in Eq. (3.14) may be optimized to yield the maximum value of $Z_{2D}T$ within the quantum well. In the 2D case, ζ^* may be varied both by doping and by changing the

[3]The constant relaxation approximation is used here. More accurate results would be obtained by considering detailed scattering mechanisms.

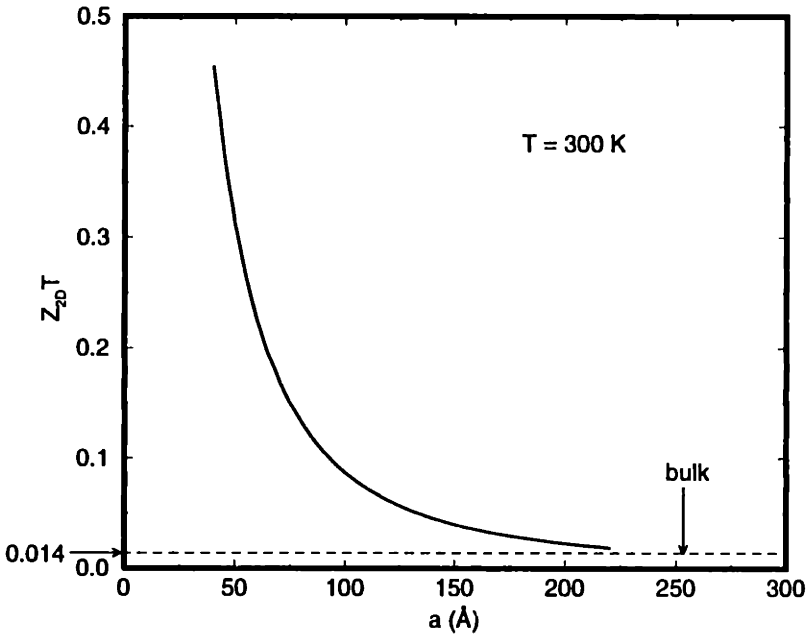

Figure 3-5: The calculated $Z_{2D}T(\zeta^*)$ versus layer thickness a at room temperature for a Si quantum well. The dashed line indicates the ZT for bulk Si.

layer thickness a. This extra degree of freedom provides a new approach for increasing $Z_{2D}T$ above the value characteristic of bulk materials.

In a quantum-well structure, since phonons can scatter off the interfaces, the phonon thermal conductivity may be reduced relative to the bulk value which is given by

$$\kappa_{ph} = \frac{1}{3} C_v v l, \tag{3.20}$$

where l is the phonon mean free path, C_v is the lattice heat capacity, and v is the velocity of sound in the material. For Si, $C_v = 1.658\,\mathrm{J\,K^{-1}\,cm^{-3}}$ and $v = 8.4332 \times 10^5\,\mathrm{cm/s}$, giving a value of $l = 282\,\text{Å}$. If the layer thickness a is greater than 282 Å, then layering does not seriously affect the mean free path l, and κ_{ph} should then be similar to its bulk value. However, if a is less than 282 Å, then l and κ_{ph} are limited by phonon scattering off the interfaces and a rough estimate for κ_{ph} is obtained by setting $l = a$ and using Eq. (3.20).

The calculated $Z_{2D}T(\zeta^*)$ as a function of a for Si quantum wells at room temperature is shown in Fig. 3-5, together with a dashed line indicating the room temperature

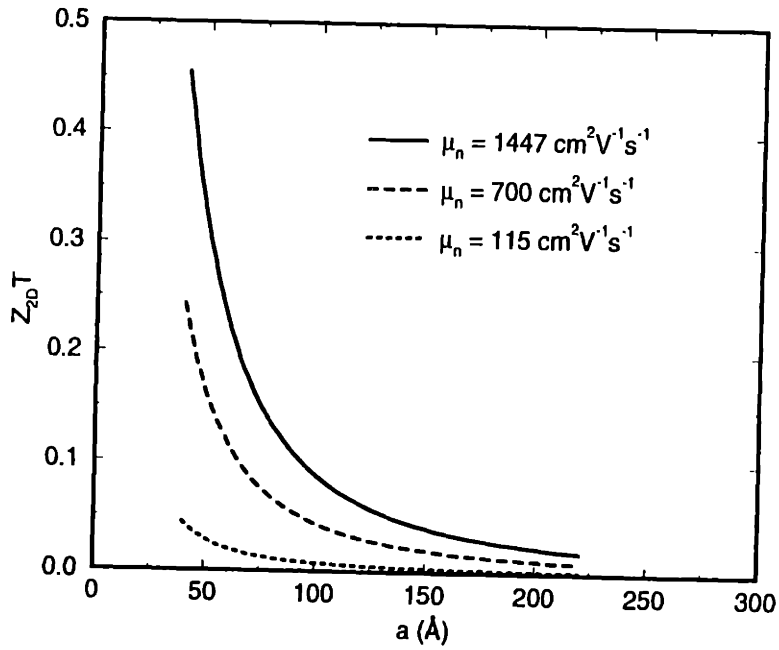

Figure 3-6: The calculated optimal $Z_{2D}T(\zeta^*)$ versus quantum well thickness a at room temperature for a Si quantum well with various electron mobilities. Thus $Z_{2D}T$ has a strong dependence on the carrier mobility.

3D figure of merit of $Z_{3D}T = 0.014$. The quantum well width in the calculations is less than the phonon mean free path l, and therefore $\kappa_{ph} = \frac{1}{3}C_v va$ can be used to provide a rough estimate for the phonon contribution to the thermal conductivity for small well widths. The results show a significant increase in the thermoelectric figure of merit for a quantum well width a below 100 Å.

My calculations further show that the optimal thermoelectric figure of merit $Z_{2D}T$ for the $Si/Si_{1-x}Ge_x$ superlattice structure has a strong dependence on the carrier mobility, as shown in Fig. 3-6.[4] However, $Z_{2D}T$ is not very sensitive to a variation in the carrier concentration in the range of 10^{18}–10^{19} cm^{-3}. Although the dependence of the mobility on the carrier concentration can be neglected in the case of modulation doping, the optimized carrier concentration indicated by the theoretical modeling ($\sim 2 \times 10^{19}$ cm^{-3}) is higher than what can be regularly achieved in the $Si/Si_{1-x}Ge_x$ quantum well system. Therefore it is advantageous to lower the carrier concentration

[4]This is an important feature when we discuss the thermoelectric properties at elevated temperatures.

below the theoretically optimized value in order to get high quality samples with better mobilities in order to improve their thermoelectric performance.

3.4 Infinite series of $Si/Si_{1-x}Ge_x$ quantum wells and barriers

In this section, I consider the superlattice structures with an infinite series of quantum wells and barriers. This is not only a more realistic assumption, but multilayer structures are also needed for making thermoelectric devices in order to get enough cooling or generating power. The band offset U in the conduction between the Si layer and $Si_{1-x}Ge_x$ layer is taken as 100 meV, which is a typical value in type II $Si/Si_{1-x}Ge_x$ superlattice structures. The barrier width is 300 Å in the calculations in order to ensure good quantum confinement of electrons in the Si layers.

Suppose the quantization is along the z-direction, then in the case of an infinitely high quantum well, the electronic dispersion relation for the subbands is

$$\varepsilon_\nu(k_x, k_y) = \frac{\hbar^2 k_x^2}{2m_x} + \frac{\hbar^2 k_y^2}{2m_y} + \frac{\hbar^2 \pi^2 \nu^2}{2m_z a^2}, \tag{3.21}$$

where m_x, m_y, and m_z are the components of the effective mass tensor, and ν is the subband index. The zero of energy is at the bulk conduction band edge. For an infinite series of quantum wells and barriers in a superlattice structure with a finite height of the barrier potential, the subband minima are determined by the relation

$$\left(\frac{\kappa^2 - k^2}{2\kappa k}\right) \sinh \kappa b \sin ka + \cosh \kappa b \cos ka = 1 \tag{3.22}$$

where b is the width of the barrier layer, and

$$\kappa = \sqrt{\frac{2m_z U}{\hbar^2} - k^2}, \tag{3.23}$$

in which U is the height of the barrier potential. The roots $\hat{k}_\nu$ of Eq. (3.22) give the

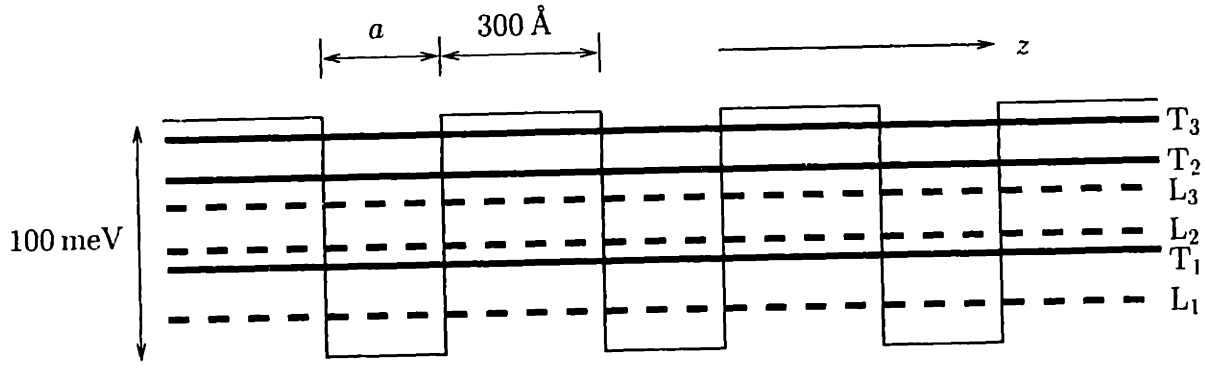

Figure 3-7: The subband levels of Si formed in an infinite series of quantum wells and quantum barriers, with a barrier height of 100 meV and a barrier width of 300 Å. Levels T_1, T_2, and T_3 denote the first three subband edges for transverse electron pockets labeled by a, b, c, and d in Fig. 3-2, and levels L_1, L_2, and L_3 denote the first three subband edges for longitudinal electron pockets labeled by e and f in Fig. 3-2.

energy band structure as

$$\varepsilon_\nu(k_x, k_y) = E_\nu + \frac{\hbar^2 k_x^2}{2m_x} + \frac{\hbar^2 k_y^2}{2m_y}, \tag{3.24}$$

where we use the notation

$$E_\nu = \frac{\hbar^2 \hat{k}_\nu^2}{2m_z} \tag{3.25}$$

to denote the subband energy levels for $k_x = 0$ and $k_y = 0$, corresponding to the energy minimum or bottom of each subband.

When the six electron ellipsoidal pockets shown in Fig. 3-2 are confined in quantum wells shown in Fig. 3-7, four of them (transverse pockets) become four-fold degenerate subband levels (pockets labeled by a, b, c, and d in Fig. 3-2), and the other two (longitudinal pockets) become two-fold degenerate subband levels (pockets labeled by e and f in Fig. 3-2). Because the z-component effective mass for the transverse pockets is smaller than that for the longitudinal pockets, the transverse subband levels for a given ν value lie higher in energy than those of the longitudinal subbands.

Figure 3-8 shows the first few transverse and longitudinal subband energy minima E_ν of Eq. (3.25) as a function of quantum well width a, taking $b = 300$ Å and $U = 100$ meV for the barrier width and height, respectively. Here we see that the second

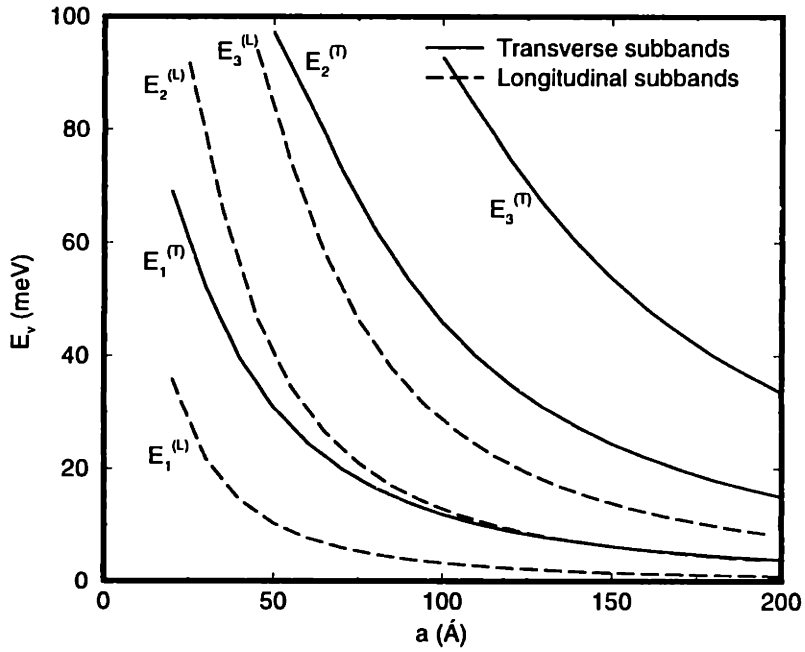

Figure 3-8: The dependence on quantum well width a of the first few subband energy minima E_ν for an infinite series of quantum wells and barriers in an n-type $Si/Si_{1-x}Ge_x$ superlattice structure with a finite height of 100 meV for the barrier potential, and 300 Å for the barrier width. The energy minima in the figure are labeled by a subscript ν and by a superscript (L) or (T) which denote the longitudinal or transverse subband, respectively.

bound state for the longitudinal subband is very close to that for the first transverse subband (for $a > 100$ Å). Therefore, more than one subband need to be taken into account in order to get more precise and reliable modeling results, as indicated in Fig. 3-8.

Theoretical calculations of the power factor for multiple subbands have been carried out as a function of the 2D carrier concentration[5] for n-type Si, based on the band structure calculation performed for different quantum well widths (Fig. 3-9). For a multiple subband model, the transport tensor is a linear combination of contributions from each transport subband (see Eq. (2.32)). Or equivalently, the overall

[5]The 2D carrier concentration is calculated as

$$n_{2D} = \int \frac{d^2k}{2\pi^2} f(\varepsilon(\mathbf{k})) = \frac{k_B T}{\pi\hbar^2}(m_x m_y)^{\frac{1}{2}} F_0,$$

where F_0 is the zeroth order Fermi-Dirac function defined in Eq. (3.9).

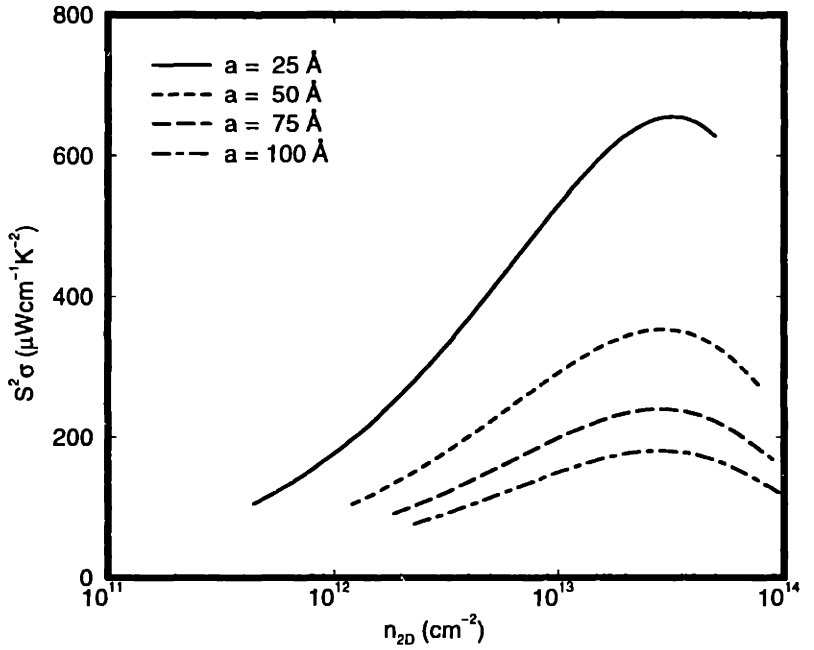

Figure 3-9: The power factor $S^2\sigma$ as a function of sheet carrier concentration n_{2D} for various quantum well widths a for various n-type $Si/Si_{1-x}Ge_x$ superlattice structures, considering contributions from the first transverse subband and the first and second longitudinal subbands (see Fig. 3-8).

electrical conductivity and Seebeck coefficient can be calculated from

$$\sigma = \sum_{\nu} \sigma^{(\nu)} \tag{3.26}$$

and

$$S = \frac{\sum_{\nu} \sigma^{(\nu)} S^{(\nu)}}{\sum_{\nu} \sigma^{(\nu)}}, \tag{3.27}$$

where it is seen that the subbands with higher electrical conductivity are more heavily weighted in calculating the Seebeck coefficient.

Figure 3-9 shows the results for $S^2\sigma$ considering the first transverse subband and the first and second longitudinal subbands. These calculations show that the required carrier concentration for optimum performance (*i.e.*, maximum $S^2\sigma$) is very high, and the optimum doping level for the maximum power factor is now in a regime where the carrier concentrations are so high, that it is difficult to prepare good quality samples with good mobility. Considering the influence of the carrier concentration on the

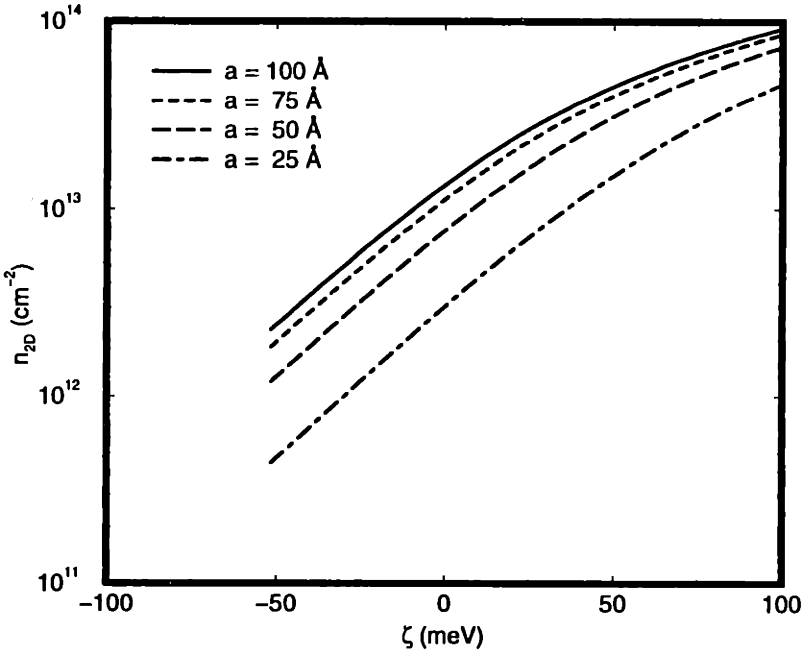

Figure 3-10: The sheet carrier concentration n_{2D} as a function of the chemical potential ζ. The chemical potential is here measured relative to the bottom of the conduction band in three-dimensional Si before the subband energies are shifted due to quantum confinement effects.

mobility, the optimum doping level should be relatively lower than that given above, because of the dependence of the mobility on the carrier concentration. Another factor that needs to be considered is that we may lose quantum confinement when we enter the heavy doping regime. Figure 3-10 shows the two-dimensional carrier density as a function of chemical potential. If the carrier density is very high, the chemical potential may get too close to the barrier potential ($U = 100\,\text{meV}$). Moreover we should take into account more subbands as the chemical potential gets larger, since more subbands will be populated and will contribute to the transport properties of the system. When we get more and more subbands to contribute to transport, then the transport also becomes more 3D and we will lose the advantage of quantum confinement. However, when the quantum well width is small enough (e.g., smaller than 100 Å) and the carrier concentration is within a practical and reasonable range so that the chemical potential is smaller than 20 meV, then there are at most three subbands, one of which is transverse and two of which are longitudinal, that contribute

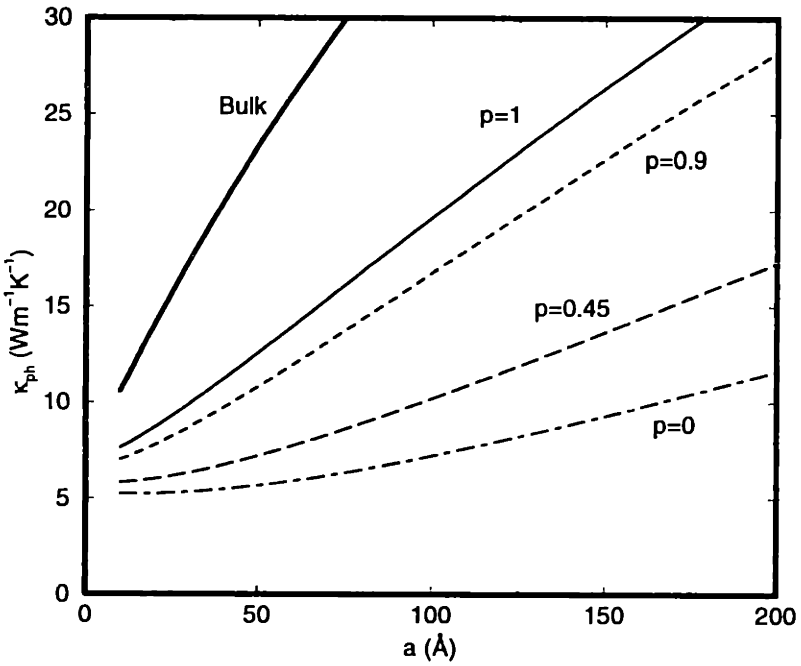

Figure 3-11: The lattice thermal conductivity for $Si/Si_{0.7}Ge_{0.3}$ superlattices as function of well thickness for various values of specularity (p). The barrier width is 300 Å.

to the transport of the system. In practice, the actual carrier concentration is far below the criteria that more than three subbands are populated, and therefore we are in the range of two-dimensional quantum confinement.

Although the detailed band shifts are considered, we believe that the carrier mobility still plays a very important role in the thermoelectric performance. Therefore we expect that the temperature dependence of the thermoelectric figure of merit is determined by the behavior of the temperature dependence of the carrier mobility. This will be discussed in Section 3.5.

In a simple kinetic theory for phonon transport, the lattice thermal conductivity is determined by Eq. (3.20). Such a treatment underestimates the mean free path (MFP) of those phonons that actually carry heat because (1) the optical phonons contribute to the specific heat but not much to the thermal conductivity due to their low group velocity, and (2) acoustic phonons in $Si/Si_{1-x}Ge_x$ materials have a large dispersion, so that their velocities are also smaller than the speed of sound. Therefore, we estimated the average phonon MFP by including only acoustic phonons and we

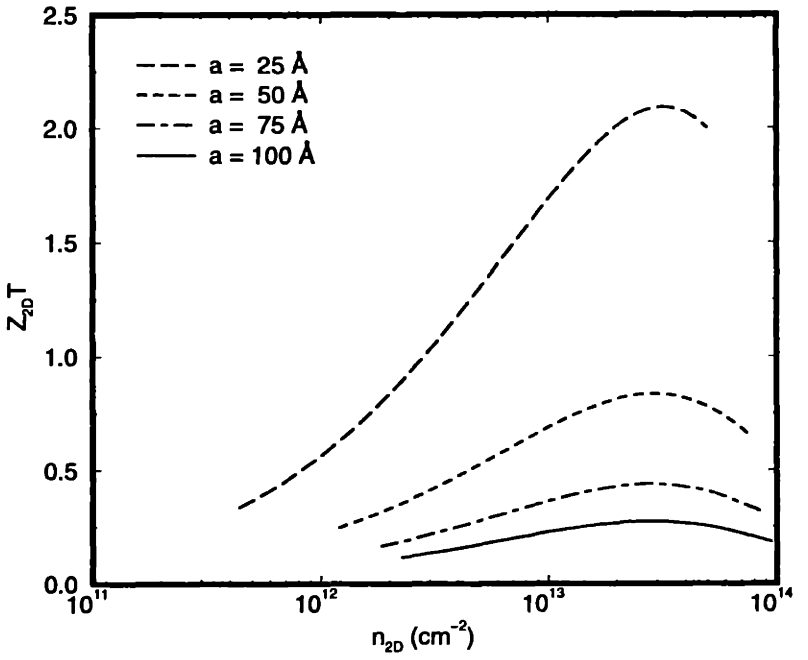

Figure 3-12: The 2D thermoelectric figure of merit for the $Si/Si_{0.7}Ge_{0.3}$ superlattice structure shown in Fig. 3-7 as a function of sheet carrier density at $T = 300\,K$, and taking $p = 1$.

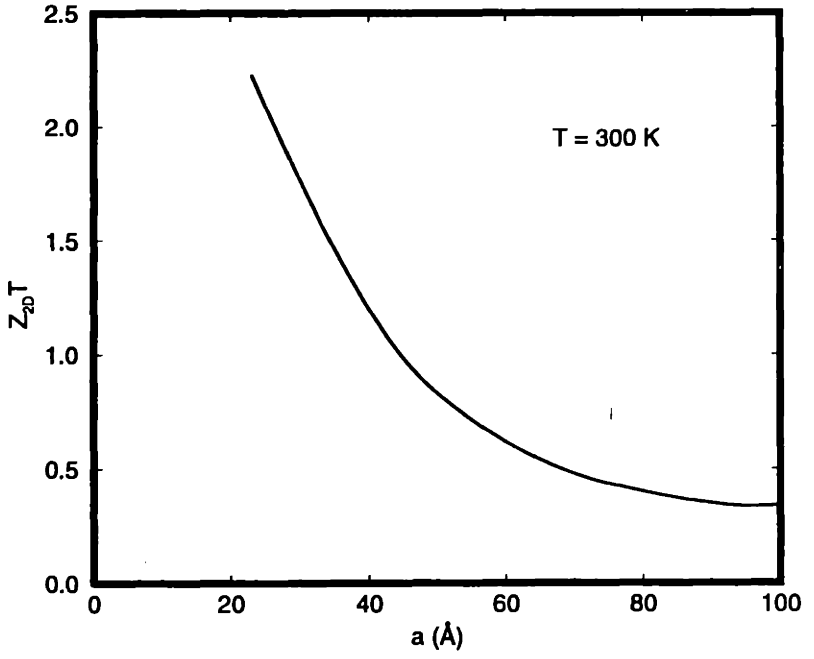

Figure 3-13: The optimal 2D thermoelectric figure of merit for the $Si/Si_{0.7}Ge_{0.3}$ superlattice structure shown in Fig. 3-7 as a function of quantum well width, taking the specularity $p = 1$.

used an averaged phonon group velocity [35]. The interface scattering effect is also considered in the modeling of the $Si/Si_{1-x}Ge_x$ thermal conductivity. A parameter p is introduced to characterize the specularity of the interface scattering, where $p = 1$ refers pure specular scattering, while $p = 0$ refers to pure diffusive scattering [35]. Figure 3-11 shows the lattice thermal conductivity as a function of quantum well width for various values of the parameter p. We see that the reduction in thermal conductivity is significant even in the case of pure specular interface scattering ($p = 1$).

Combining the power factor modeling in Fig. 3-9 and the thermal conductivity[6] in Fig. 3-11 with $p = 1$, which is a conservative assumption, we get the thermoelectric two-dimensional figure of merit for the $Si/Si_{1-x}Ge_x$ superlattice plotted as a function of n_{2D} in Figs. 3-12 and as a function of a in Fig. 3-13. We see that the $Z_{2D}T$ can reach as high as 2.0 at room temperature for a superlattice with a quantum well width of 25 Å. These results imply that this kind of material has very good potential for thermoelectric applications, even at room temperature.

3.5 Temperature dependence study

Since $Si/Si_{1-x}Ge_x$ is a system aimed at high temperature operation (up to 1000 K), it is interesting to investigate the thermoelectric performance of $Si_{1-x}Ge_x$ quantum well systems at elevated temperatures. Since the power factor for $Si_{1-x}Ge_x$ materials generally increases with increasing T above room temperature [25, 26], the power factor as well as the thermoelectric figure of merit within the quantum well are expected to show even greater enhancement above 300 K.

As discussed in Section 3.3, we have found that the value of $Z_{2D}T$ for quantum wells is very sensitive to the carrier mobility. This implies that the carrier mobility is one of the most important factors in determining the thermoelectric performance. With increasing temperature, it is well known that the carrier mobility for Si decreases exponentially in the temperature range between 300 K and 1000 K, which can be

[6]The electronic part of the thermal conductivity is calculated using Eq. (3.12) for each subband.

written empirically as

$$\mu_n = \mu_0 T^{-\lambda}, \tag{3.28}$$

where $\lambda = 2.42$ for electron carriers in intrinsic Si.[7] If we use Eq. (3.28) with $\lambda = 2.42$ to calculate the temperature dependent figure of merit for Si quantum wells, we will find that $Z_{2D}T$ is not favorable at high temperatures because of the rapid decrease of the carrier mobility. However, in the case of 2D Si quantum wells for thermoelectric applications, the optimal carrier concentration is on the order of $4 \times 10^{18}\,\mathrm{cm}^{-3}$. For such heavily doped n-type bulk Si, the exponent λ in Eq. (3.28) can be approximated using existing experimental data [37] to obtain $\mu_n = 2.11 \times 10^5 T^{-1}\mathrm{cm}^2/\mathrm{Vs}$ (T in K). This weaker temperature dependence[8] has a large effect on $Z_{2D}T$ as a function of quantum well width at elevated temperatures, as shown in Figs. 3-14 and 3-15. These results suggest that $Z_{2D}T$ for $Si/Si_{1-x}Ge_x$ quantum wells become more favorable at higher temperatures.

It should be pointed out that the temperature-dependent mobility values used in the calculations so far are all for bulk Si. In the case of Si quantum wells, the mobility as a function of temperature could be quite different from that of the bulk. Specifically, we expect the decrease in mobility with increasing temperature to be slower in a quantum well relative to bulk Si due to the lower impurity scattering by electrons within the quantum well, when modulation doping is employed.

It is important to note that material science issues may cause problems at high temperatures for superlattice structures. The interface may become diffusive, and thermal excitations of electron and hole pairs may reduce the Seebeck coefficient. A more detailed study of these issues is needed when more experimental evidence on this topic becomes available.

---

[7] For intrinsic Si, the scattering mechanism for electrons is predominantly a combination of lattice scattering and inter-valley scattering [36].

[8] For extrinsic Si, the impurity scattering becomes dominant, thereby leads to a T^{-1} law [36].

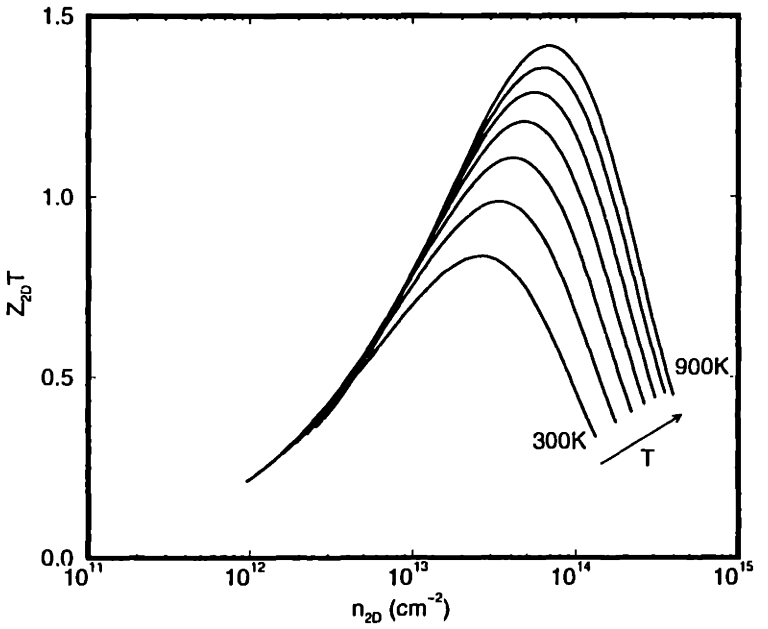

Figure 3-14: The calculated $Z_{2D}T$ versus carrier density at various temperatures (300 K, 400 K, ..., 900 K) for $Si/Si_{1-x}Ge_x$ superlattice structures as considered in Fig. 3-8. The electron mobility is determined empirically as $\mu_n = 2.11 \times 10^5 T^{-1}\text{cm}^2/\text{Vs}$ (T in K) for n-type Si with carrier concentration of 10^{18}cm^{-3}, appropriate for thermoelectricity applications.

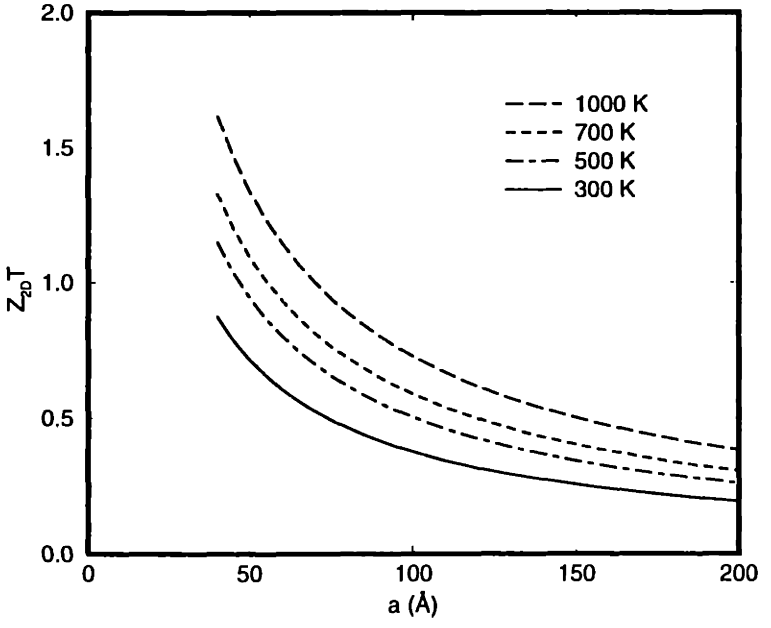

Figure 3-15: The optimal $Z_{2D}T$ versus layer thickness a at various temperatures for a Si quantum well. The electron mobility is determined empirically as $\mu_n = 2.11 \times 10^5 T^{-1}\text{cm}^2/\text{Vs}$ (T in K) for n-type Si with a carrier concentration of 10^{18}cm^{-3} appropriate for thermoelectricity applications.

3.6 The influence of barrier layers on ZT

The influence of barrier layers on the thermoelectric figure of merit has been an important problem for two-dimensional thermoelectric structures. The concept of the enhancement of thermoelectric figure of merit inside quantum wells has been generally accepted. However, in order to make useful thermoelectric devices, the effect of the barrier layers also has to be considered.

In Table 3.1, I calculated a specific example to consider the effect of the barrier layers on the thermoelectric figure of merit of the whole structure. The superlattice structure has a quantum well width $a = 25\,\text{Å}$, and a barrier thickness $b = 300\,\text{Å}$. For the Si quantum well part, I use the modeling results described in Section 3.4, which yields a resulting $Z_{2D}T = 2.0$ at $T = 300\,\text{K}$. I then treated the $Si_{1-x}Ge_x$ barrier layer as an alloy with three-dimensional transport characteristics. In fact, $Si_{1-x}Ge_x$ as an alloy is a good thermoelectric material which could have ZT as high as 0.1 at room temperature. The electrical conductivity and Seebeck coefficient for the $Si_{1-x}Ge_x$ barrier layer have been calculated [25], resulting in an overall electrical conductivity $\sigma_{3D} = 2,499.6\,\Omega^{-1}\text{cm}^{-1}$, and a weighted average of the Seebeck coefficient $S_{3D} = 161.6\,\mu\text{VK}^{-1}$. The thermal conductivity of the superlattice structure is then calculated to be $\kappa = 8.7\,\text{Wm}^{-1}\text{K}^{-1}$ (Section 3.4). The overall three-dimensional figure of merit for this whole superlattice structure is then calculated to be $Z_{3D}T = 0.23$, for $T = 300\,\text{K}$, a nearly nine-fold reduction compared to the $Z_{2D}T$ value within the Si quantum well.

Although a nearly nine-fold reduction is caused by the barrier layer, the value of $Z_{3D}T$ is still quite interesting and shows an enhancement over its bulk $Si_{1-x}Ge_x$ alloys. Moreover, this example shows a very conservative structure which has a rather large barrier thickness. In practice, the barrier layer thickness can be greatly reduced to get better overall thermoelectric performance. The same calculation for a barrier thickness of 100 Å shows only a three quarters reduction in ZT.

The above example gives a pretty good idea of how the barrier layer affects the overall thermoelectric figure of merit in typical cases. In order to optimize $Z_{3D}T$ of the

Table 3.1: The influence of barrier layers on the thermoelectric transport coefficients.

	Si well	$Si_{1-x}Ge_x$ barrier	$Si/Si_{1-x}Ge_x$ superlattice
Thickness (Å)	25	300	325
σ ($\Omega^{-1}cm^{-1}$)	28,000	374.6	2,499.6
S ($\mu V/K$)	150	233.5	161.6
$S^2\sigma$ ($\mu Wcm^{-1}K^{-2}$)	630	20.4	65.2

whole superlattice structure, detailed transport properties inside the barrier region have to be investigated, and a very promising way to approach this problem is the application of carrier pocket engineering to the thermoelectric transport properties [18]. I will briefly discuss this topic in Chapter 6 of this thesis.

3.7 Quantum confinement in the presence of δ-doping in the barrier layers

The quantum confinement of carriers within a quantum well is important for getting high mobility carriers and to validate the two-dimensional transport model. In order to get high thermoelectric performance in the Si quantum well, one has to use a relatively large barrier width. This reduces the overall thermoelectric performance because of the barrier region. Simply reducing the barrier width will destroy the quantum confinement, hence bringing the system back to the three-dimensional case. In this case, a different approach[9] is needed to consider the enhancement of the thermoelectric figure of merit in superlattice structures.

Figure 3-16 shows a strategy to improve quantum confinement with thinner barrier layers by employing δ-doping layers within the barriers to form very thin sheets of a wide band gap semiconductor.[10] I have performed theoretical modeling with SiC, which is a wide band gap semiconductor, as the δ-doping layer. The effect of δ-doping

[9]In fact, carrier pocket engineering [18] provides a different strategy to improve $Z_{3D}T$.

[10]This strategy assumes that we can achieve a high enough carrier density in the quantum wells by this approach.

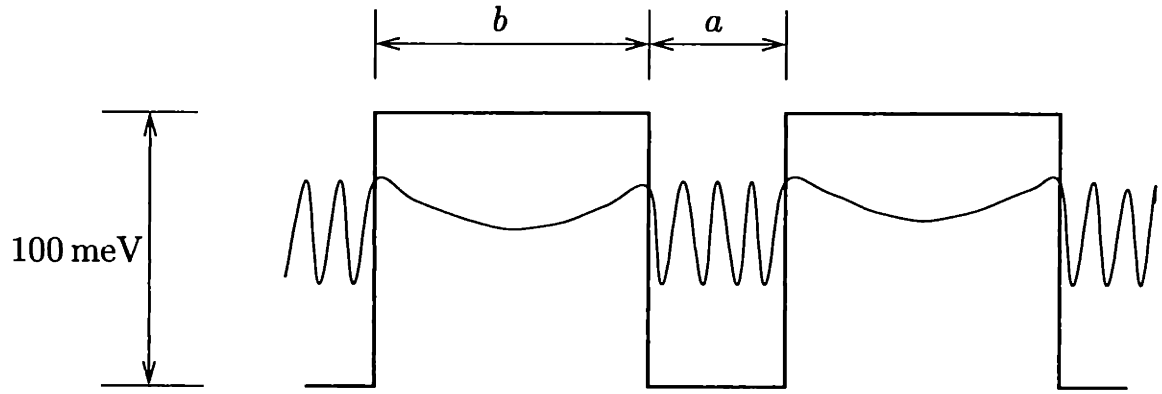

(a)

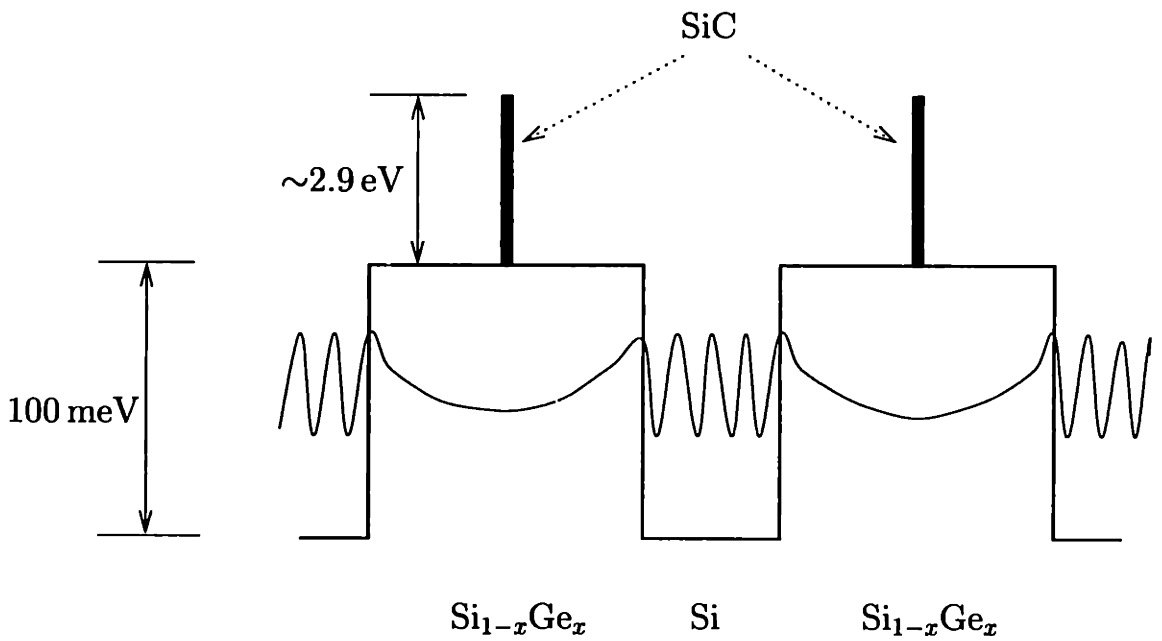

(b)

Figure 3-16: The δ-doping within barrier layers, using the wide bandgap material SiC, and the schematic electron wavefunctions in Si/SiGe superlattices without (a) and with (b) δ-doping SiC layers.

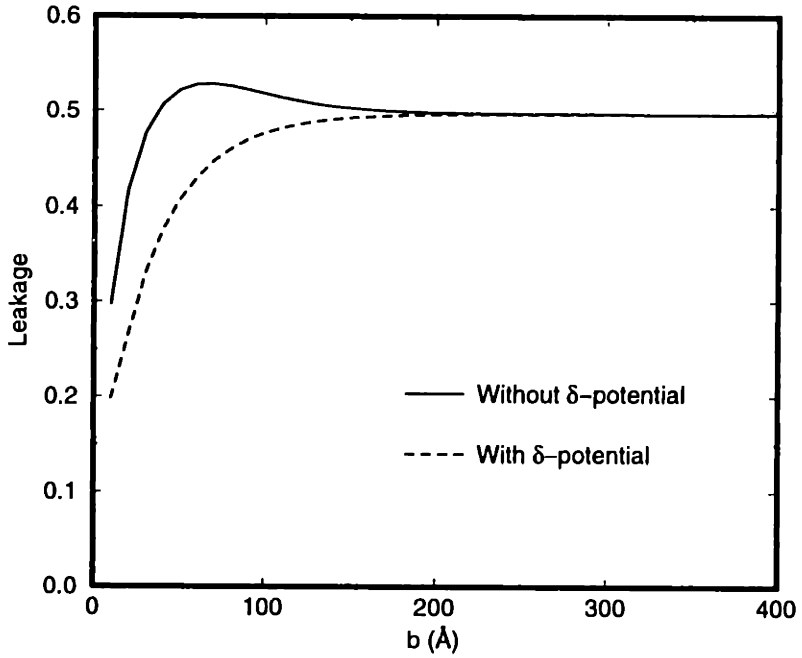

Figure 3-17: The wavefunction leakage as a function of barrier width b without and with the presence of δ-doping in the barrier layers in $Si/Si_{1-x}Ge_x$ superlattices. The quantum well thickness is $a = 20\,\text{Å}$.

can be taken into account by introducing a δ-potential of the form

$$V(z) = V\delta(z - z_0), \tag{3.29}$$

into the Schrödinger equation for electrons in the framework of a semiclassical theory (Chapter 2), where z_0 is the position of the δ-doping layer and V is the product of the barrier height and the width for the δ-doping layer. For δ-doping by SiC, I have considered a δ-doping layer with a width of 2Å, which is a single monolayer of SiC, so that $V = 2.9\,\text{eV} \times 2\,\text{Å}$.

The quantum confinement in the quantum well can be characterized by the wavefunction leakage into the barrier layer which is defined as

$$\text{leakage} = \frac{\int_{\text{barrier}} |\Psi(z)|^2\, dz}{\int_{\text{well+barrier}} |\Psi(z)|^2\, dz}. \tag{3.30}$$

Figure (3-17) shows the wavefunction leakage as a function of barrier width b without

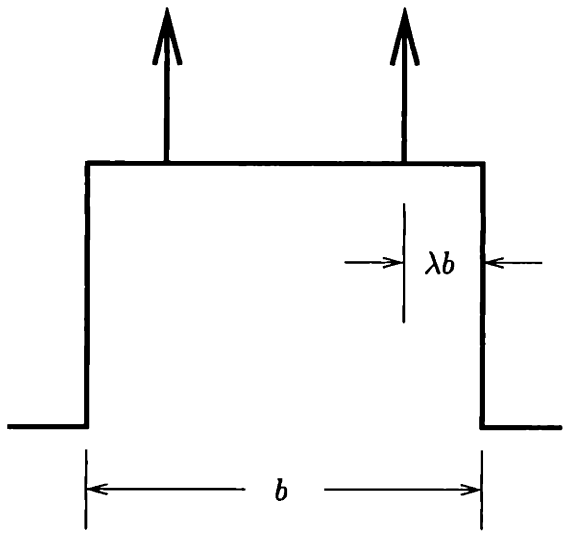

(a)

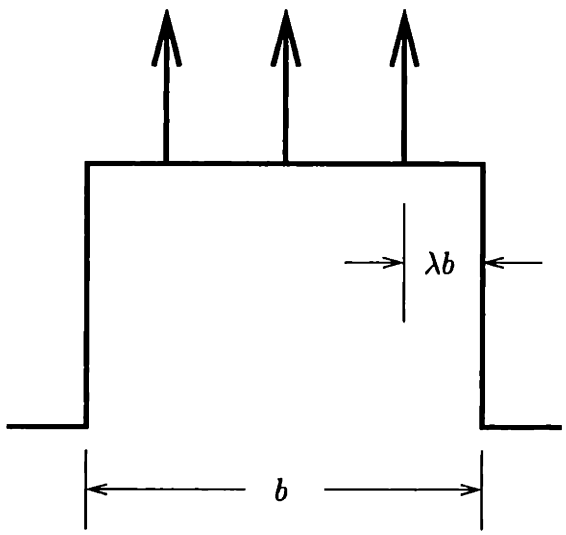

(b)

Figure 3-18: The proposed multiple δ-doping schemes within the barrier layers, using the wide bandgap material SiC. The off-centered δ-doping is λb away from the interface between the barrier layer and quantum well layer. The off-centered δ-doping layers are symmetric with respect to the center of the barrier layer.

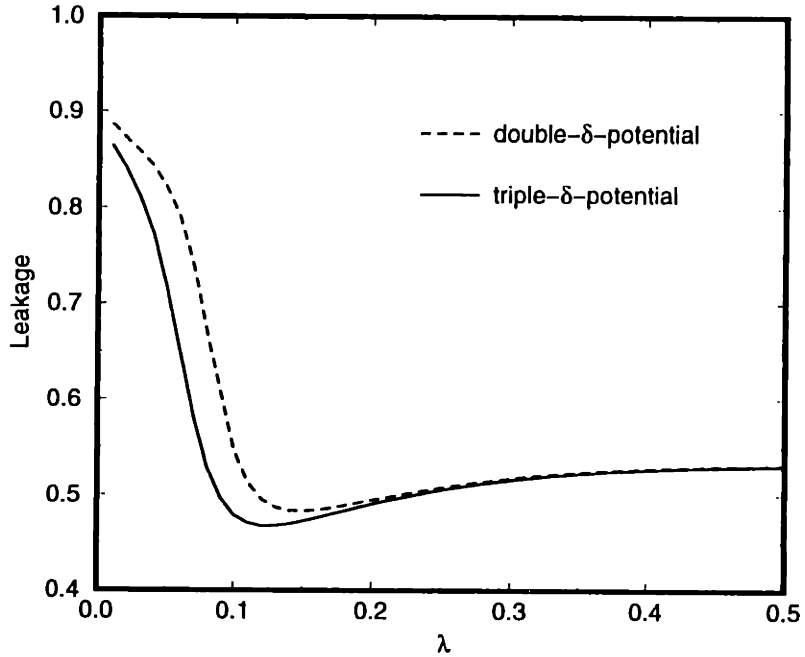

Figure 3-19: The wavefunction leakage as a function of the dimensionless position parameter (λ) of the off-centered δ-doping layers as shown in Fig. 3-18 for a $Si/Si_{1-x}Ge_x$ superlattice with a quantum well thickness $a = 20$ Å and a barrier thickness $b = 300$ Å.

and with the presence of δ-doping in the barrier layers in $Si/Si_{1-x}Ge_x$ superlattices with quantum well thickness $a = 20$ Å. It is seen that for barrier widths less than 200Å, the wavefunction leakage is decreased significantly in the presence of the SiC δ-potential.

Although the presence of a δ-potential in the mid-point of the barrier layer can successfully suppress the wavefunction amplitude $|\Psi(z)|$ in the barrier layers, thereby leading to a better isolation between adjacent quantum wells, the single δ-potential, however, has only a relatively small effect on the leakage of the wave function out of the quantum well due to the very small value of the wavefunction magnitude $|\Psi(z)|$ at the mid-point of the barrier before the δ-potential is introduced.

To get better isolation between adjacent quantum wells, I propose multiple δ-potential schemes as shown in Fig. 3-18. The parameter λ determines the location of the off-centered δ-doping layers. In order to determine the best location for the off-centered δ-doping layers, I calculated the wavefunction leakage as a function of the position (λ) of the off-centered δ-doping layers for a $Si/Si_{1-x}Ge_x$ superlattice with

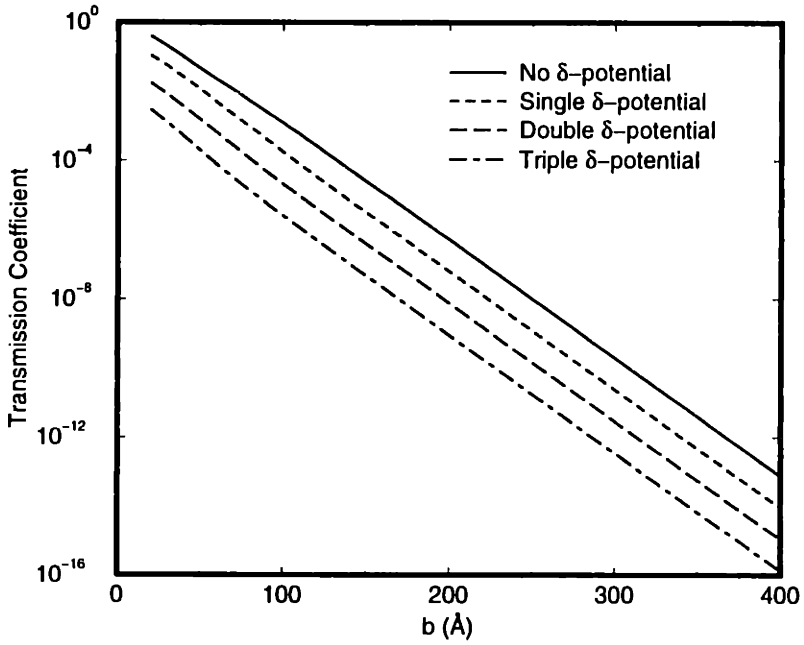

Figure 3-20: The transmission coefficient plotted on a logarithm scale as a function of barrier width b for different δ-doping schemes in $Si/Si_{1-x}Ge_x$ superlattices. The quantum well thickness is $a = 20\,\text{Å}$.

quantum well thickness $a = 20\,\text{Å}$ and barrier thickness $b = 300\,\text{Å}$, shown in Fig. 3-19. We see that for the both double δ-potential and the triple δ-potential, the best location for the off-centered δ-layers is at places such that $\lambda \approx 1/8$.

The wavefunction leakage defined in Eq. (3.30) is not the only factor affecting the electronic states within the superlattice. Carrier tunneling across the barrier layers should also be avoided and therefore should be considered, especially in the case of thin barriers. The transmission coefficient D through a barrier potential $U(z)$ can be found generally as [38]

$$D = D_0\, e^{-\frac{2}{\hbar}\int \sqrt{2m^*[U(z)-E]}\,dz}, \tag{3.31}$$

where E is the energy eigenvalue of the electronic state, and D_0, which corresponds to the transmission coefficient for a freely propagating wave, is approximately equal to one for all practical purposes. Figure 3-20 shows the numerical calculations for the transmission coefficient as a function of barrier width for the four cases that I discussed above, including a single δ-potential at the mid-point of the barrier as well

as two and three δ-potentials within the barrier layer.[11] In Fig. 3-20 we observe that while maintaining the same transmission coefficient, the barrier width can be reduced significantly by introducing one or more δ-doping layers within the barrier region.

The above discussion suggests some promising strategies for making better thermoelectric structures. This will be further discussed in Chapter 6 of this thesis.

[11] Because the transmission coefficient is integrated over the barrier region as shown in Eq. (3.31), the location of the off-centered δ-potential does not affect the value of D.

Chapter 4

Bismuth quantum wire system

In Chapter 3, I considered the effect of using two-dimensional n-type Si quantum well superlattice structures on the thermoelectric figure of merit $Z_{2D}T$. It was shown that ZT was significantly enhanced over its bulk form. In those calculations, the quantum confinement was introduced into a semiconductor system.

For two-band (mixed-conduction of electrons and holes) materials such as semimetals, both electrons and holes contribute to the conduction. As shown in Fig. 4-1, there is an overlap between the conduction band and valence band in a bulk semimetal, with the Fermi level located at a position to yield equal numbers of electrons and holes in the system. This causes an approximate cancellation of the contribution to the Seebeck coefficient, because electrons and holes have charges of opposite sign. Semimetals therefore have relatively low values of ZT.

Although the overall ZT of semimetal systems is generally low, the contribution of the conduction band or valence band individually to the ZT may be high. In fact, bismuth is a such kind of material [39]. In this case, quantum confinement is a possible mechanism to effectively separate the conduction contributed from electrons and holes. When we introduce quantum confinement into a semimetal system, the lowest conduction subband will move up and the highest valence subband will move down. As quantum confinement gets stronger, at some point a semimetal-semiconductor transition will occur, as shown in Fig. 4-1, resulting in a low-dimensional semiconducting system. By adjusting the chemical potential in the system through variation

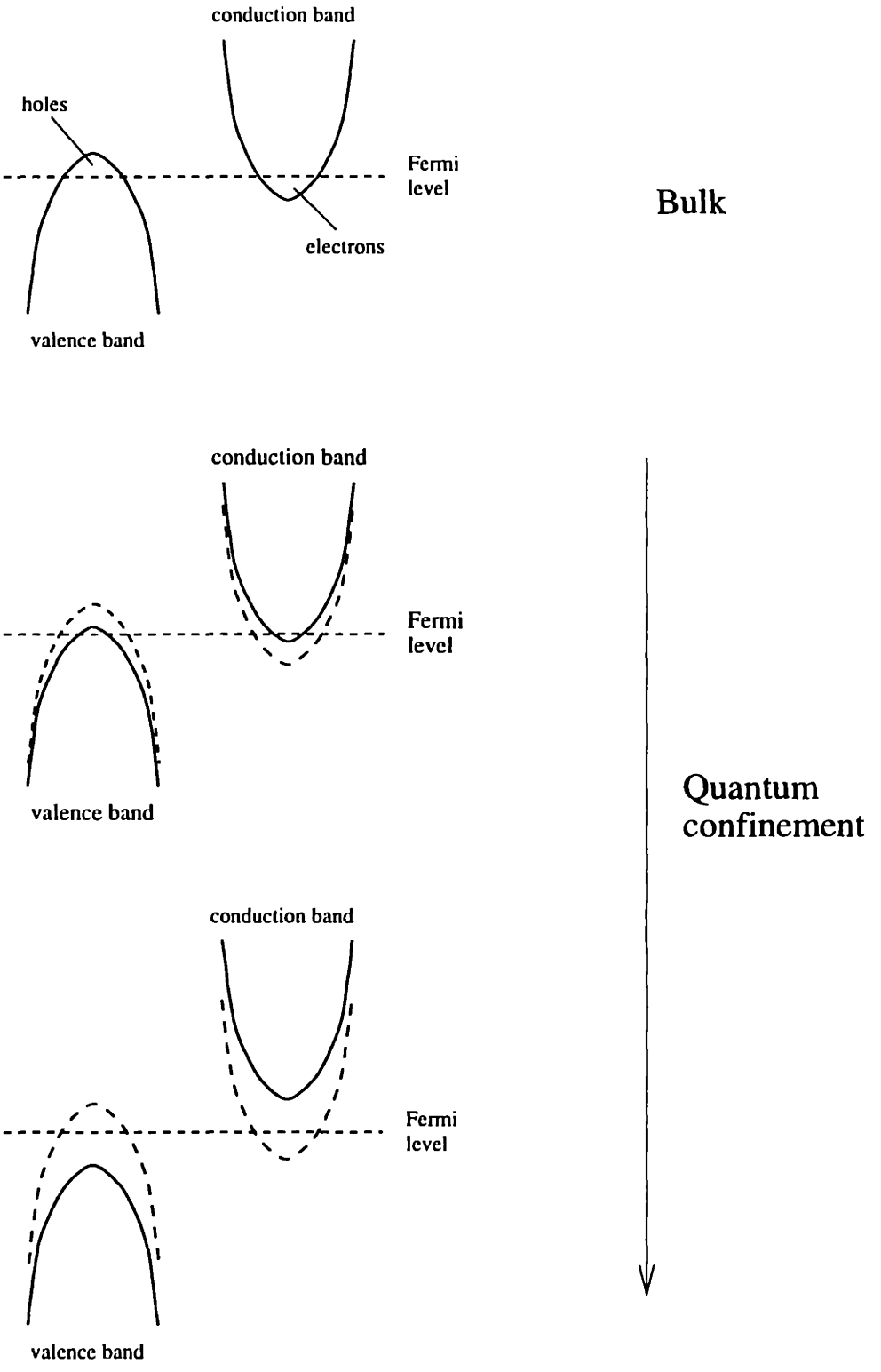

Figure 4-1: The semimetal-semiconductor transition for a semimetal resulting from quantum confinement. The dashed curves denote the bulk band edges for the conduction and valence bands and the solid curves denote the highest valence subband and the lowest conduction subband in the quantum confinement regime.

of the doping level, such kind of a low-dimensional semiconductor can potentially turn into a good thermoelectric material.

Nanowire systems have attracted a great deal of research interest because of their potential applications in thermoelectric devices and their promise for studying the transport properties of 1D systems. Bismuth, which is a semimetal with a very small electron effective mass and a highly anisotropic Fermi surface, is considered as a good candidate to study quantum confinement effects in a 1D system and as a very promising material for thermoelectric applications [7]. One promising approach to fabricate nanowire systems is to fill an array of parallel nano-channels with the media of interest for thermoelectric applications. Porous anodic alumina [40], which has a hexagonal array of nanometer-sized channels, is one such possible host template. Substantial progress in the fabrication techniques has been made recently [41] in filling these channels with bismuth from the liquid phase. The availability of Bi quantum wires stimulated the calculations described in this thesis.

In this chapter, I calculated the one-dimensional thermoelectric transport properties of Bi quantum wires, firstly based on a simple parabolic band structure for Bi. Then a more detailed and more practical investigation was carried out, considering the non-parabolic features of the strongly-coupled L-point conduction and valence bands and the temperature dependence of the various band parameters. Calculations have also been performed for Bi quantum wires along different crystalline directions and as a function of temperature.

4.1 Band structure of bismuth

Bismuth has a rhombohedral crystal structure, which can be expressed in terms of a hexagonal unit cell with lattice parameters $a_0 = 4.5$ Å and $c_0 = 11.9$ Å [42]. The rhombohedral crystal structure can be regarded at two inter-penetrating face centered cubic (fcc) lattices with a slight distortion along the body diagonal of the cube and a small displacement of the two sublattices relative to each other along this body diagonal direction, thereby resulting in a Brillouin zone similar to that for an fcc

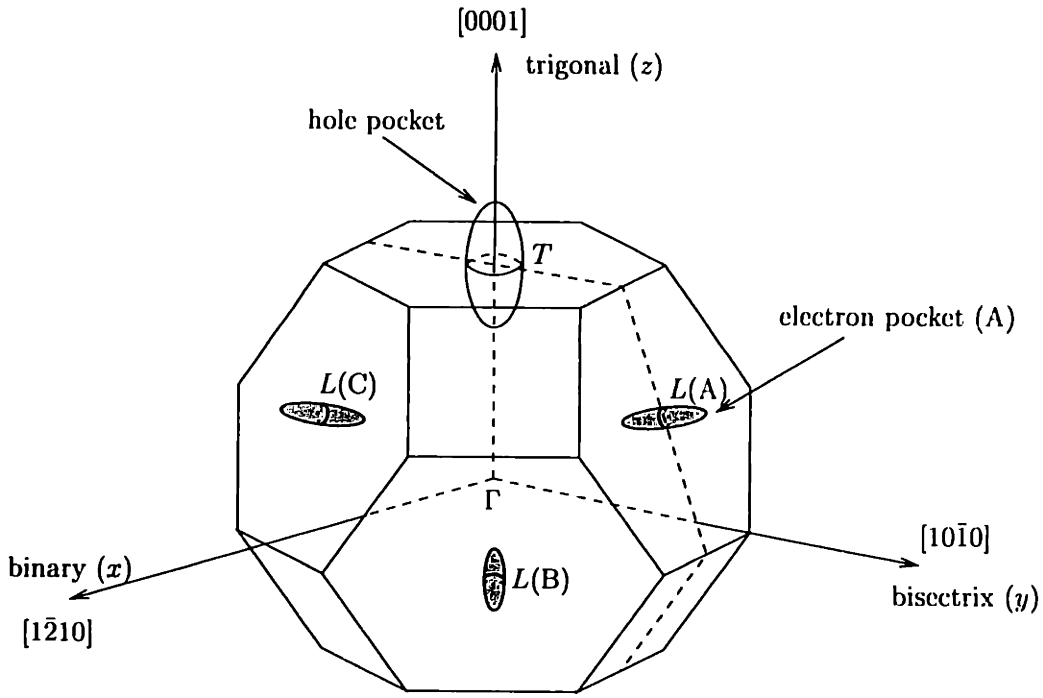

Figure 4-2: The Fermi surface of bulk Bi, showing the hole pocket at the T-point and the three electron pockets at the L-points. The volume of the hole ellipsoid at the T-point is three times of the volume of an electron ellipsoid at each L-point.

lattice, as shown in Fig. 4-2, containing two atoms per unit cell. A schematic band diagram for Bi is shown in Fig. 4-3. In the Bi band structure, there exists an overlap energy of $-\Delta_0$ between the conduction band at the L-point and the valence band at the T-point, with the Fermi level lying in between these band edges.[1] This band structure results in an ellipsoidal hole carrier pocket at the T-point in the Brillouin zone and three equivalent ellipsoidal electron carrier pockets at the L-point, as shown in Fig. 4-2. For pure Bi at 0 K, the Fermi level is determined, such that there are equal numbers of holes and electrons in the system.

The hole carrier pocket at the T-point can be characterized by a effective mass tensor

$$\mathbf{m}_h = \begin{pmatrix} m_{h1} & 0 & 0 \\ 0 & m_{h1} & 0 \\ 0 & 0 & m_{h3} \end{pmatrix}, \tag{4.1}$$

[1] $\Delta_0 = -38$ meV at $T = 0$ K.

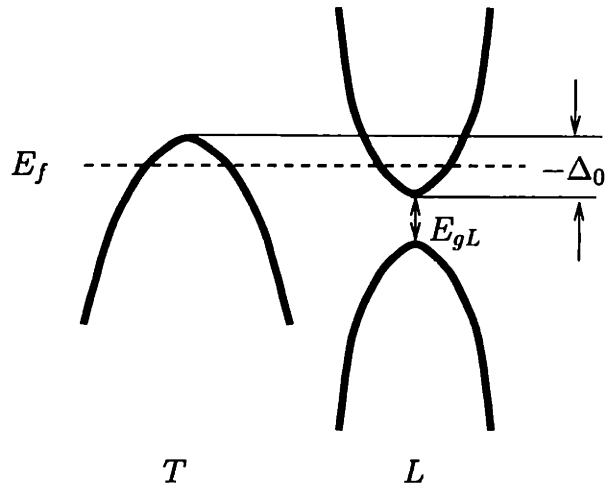

Figure 4-3: A schematic diagram of the band structure for bulk bismuth near the Fermi level E_f. There is an overlap energy of $-\Delta_0$ between the conduction band at the L-point and the valence band at the T-point, with the Fermi level lying in between. There is a small direct band gap E_{gL} between the conduction and valence bands at the L-point.

with symmetric x and y components m_{h1}, and a heavier mass component along the trigonal z direction, $m_{h3} \gg m_{h1}$, reflecting a large anisotropy of the hole carrier pocket. The electron carrier pockets at the L-points, however, are more complicated. The electron carrier pocket lying close to the bisectrix axis (labeled by A in Fig. 4-2) can be expressed by an effective mass tensor

$$\mathbf{m}_e = \begin{pmatrix} m_{e1} & 0 & 0 \\ 0 & m_{e2} & m_{e4} \\ 0 & m_{e4} & m_{e3} \end{pmatrix}, \tag{4.2}$$

with $m_{e2} \gg m_{e1}, m_{e3}$ reflecting a very large anisotropy in the electron ellipsoids. The off-diagonal element m_{e4}, which has a positive value [43], indicates a positive tilt angle $\theta \approx 6°$ of the longest principal axis of the ellipsoid away from the bisectrix axis which is determined by

$$\tan 2\theta = \frac{2m_{e4}}{m_{e2} - m_{e3}}. \tag{4.3}$$

The other two electron ellipsoids (labeled with B and C in Fig. 4-2) are obtained by rotation of ellipsoid A by $\pm 120°$ about the trigonal axis.

Another important feature of the bismuth band structure is that there is a lower valence band at each of the three L-points which is strongly coupled to an L-point conduction band, as shown in Fig. 4-3. The band gap E_{gL} between these two bands is very small,[2] resulting in strong correlation between them. The L-point valence band is generally not occupied by holes at low temperature. The strong coupling between the valence and conduction bands produces strong non-parabolic dispersion relations for the L-point electrons and holes, which are well described by the Lax model [44–46], which is based on $\mathbf{k} \cdot \mathbf{p}$ perturbation theory.

4.2 The two-band thermoelectric transport model for one-dimensional Bi

Under the experimental conditions that are achieved in the fabrication of bismuth nanowires with diameters in the range 10 to 110 nm and lengths up to 100 μm, the bismuth nanowires can be considered as 1D quantum systems. Expressions for S, σ, κ_e in this system can be derived in the same manner as in Section 3.2. The general expressions given by Eqs. (2.28)-(2.30) are here applied to a 1D system with the transport tensor elements given by Eq. (2.33).

As we introduce quantum confinement into the Bi nanowire system, the extremal conduction subband and valence subband edges will move in opposite directions as shown in Figs. 4-1 and 4-4, so that eventually $\Delta = 0$ denoting the semimetal-semiconductor transition as the wire cross-sectional thickness is decreased below a_c. Over a large range of wire diameters where quantum confinement becomes important in Bi nanowires, the separation between the lowest L-point conduction subband edge and the highest T-point valence subband edge Δ is so small, even in the semiconductor range, that we need to take into account the contributions to the transport

[2] $E_{gL} = 13.6$ meV at $T = 0$ K.

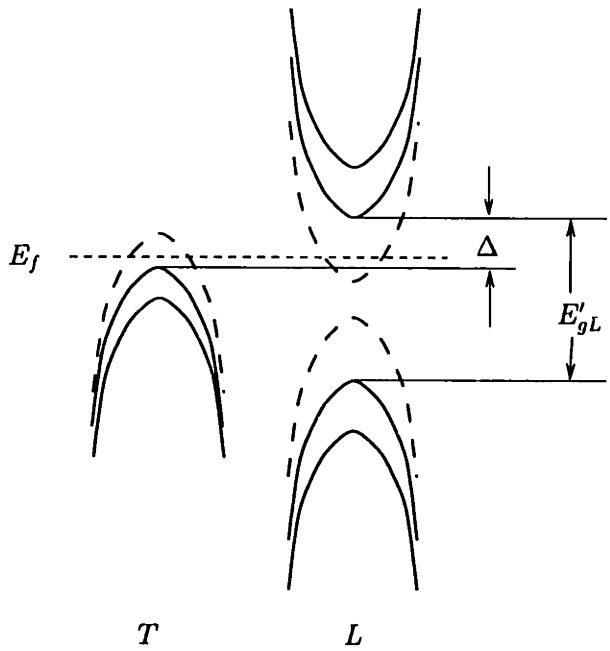

Figure 4-4: A schematic diagram of the band structure for bismuth under quantum confinement conditions. An indirect band gap Δ is developed between the lowest conduction subband at the L-point and the highest valence subband at the T-point. As more quantum confinement is introduced, the direct band gap E'_{gL} at the L point increases quickly because of the small effective masses for both L-point electrons and holes.

properties from both the electrons and the holes.[3] In this case, the transport tensor elements become a summation of terms from both electrons and holes.[4] When the nanowires are fabricated so that their wire axes are along a crystalline direction other than the trigonal direction, multiple contributions from the electronic subbands arising from the anisotropy of the carrier pockets must also be considered.

In the following we first consider the case of parabolic L-point conduction bands

[3]As the quantum confinement is introduce, the direct band gap E'_{gL}, between the lowest conduction subband edge and the highest valence subband edge at the L-point, increase quickly with the decrease of wire width a so that the valence band at the L-point is always much lower than the valence band at the T-point. Therefore, in this chapter, I do not consider any contribution from the holes in the L-point valence band to transport. However, these holes become important when we introduce Sb alloying in Bi. This will be discussed in Chapter 6.

[4]Note, however, that $\mathcal{L}^{(1)}$ in Eq. (4.7) experiences a partial cancellation from the electron and hole contributions, because of the odd charge parity e shown in Eq. (2.29).

and then we consider the more realistic but computatively more difficult case of non-parabolic dispersion relations for the L-point electrons. First, assuming parabolic energy dispersion relations for both electrons at the L-points and holes at the T-point, we can write

$$\varepsilon_{e,h}(k) = \varepsilon_{e,h}^{(0)} \pm \frac{\hbar^2 k^2}{2m_{e,h}^*}, \tag{4.4}$$

where k is the wave number for electrons or holes in the 1D transport system, $\varepsilon_{e,h}^{(0)}$ denotes the subband edges of the conduction and valence bands, respectively, and $m_{e,h}^*$ denotes the effective mass components for electrons and holes, respectively, along the transport direction. The transport tensor elements are then calculated to be[5]

$$\mathcal{L}^{(0)} = D_e\left[\frac{1}{2}F^e_{-\frac{1}{2}}\right] + D_h\left[\frac{1}{2}F^h_{-\frac{1}{2}}\right] \tag{4.5}$$

$$\mathcal{L}^{(1)} = (k_BT)\left(D_e\left[\frac{3}{2}F^e_{\frac{1}{2}} - \frac{1}{2}\zeta_e^*F^e_{-\frac{1}{2}}\right] - D_h\left[\frac{3}{2}F^h_{\frac{1}{2}} - \frac{1}{2}\zeta_h^*F^h_{-\frac{1}{2}}\right]\right) \tag{4.6}$$

$$\mathcal{L}^{(2)} = (k_BT)^2\left(D_e\left[\frac{5}{2}F^e_{\frac{3}{2}} - 3\zeta_e^*F^e_{\frac{1}{2}} + \frac{1}{2}\zeta_e^{*2}F^e_{-\frac{1}{2}}\right] + D_h\left[\frac{5}{2}F^h_{\frac{3}{2}} - 3\zeta_h^*F^h_{\frac{1}{2}} + \frac{1}{2}\zeta_h^{*2}F^h_{-\frac{1}{2}}\right]\right) \tag{4.7}$$

where D_e and D_h are given by

$$D_{e,h} = \frac{2e}{\pi a^2}\left(\frac{2k_BT}{\hbar^2}\right)^{\frac{1}{2}}(m_{e,h}^*)^{\frac{1}{2}}\mu_{e,h}, \tag{4.8}$$

and where

$$F_i^{e,h} = \int_0^\infty \frac{x^i dx}{e^{(x-\zeta_{e,h}^*)}+1} \tag{4.9}$$

denotes the Fermi-Dirac related functions, with fractional indices $i = -\frac{1}{2}, \frac{1}{2}, \frac{3}{2}, \ldots$. The reduced chemical potentials $\zeta_{e,h}^* = (\zeta_{e,h} - \varepsilon_{e,h}^{(0)})/k_BT$ are related to each other through

$$\zeta_e^* + \zeta_h^* = -\Delta \tag{4.10}$$

[5]In 1D transport, the $\mathcal{L}^{(\alpha)}$ tensors reduce to scalars, as discussed in Section 2.5. Also, only the lowest conduction subband and the highest valence subband are considered here. In some cases, more than one subband need to be considered.

where Δ is the energy gap between the lowest L-point conduction subband and the highest T-point valence subband in the presence of quantum confinement, as shown in Fig. 4-4.[6] By controlling the doping level, the chemical potential can be adjusted to optimize $Z_{1D}T$ for the quantum wire system. In Eq. (4.8), $m^*_{e,h}$ and $\mu_{e,h}$ are effective masses and carrier mobilities, respectively, along the transport direction for electrons and holes.

The electrical conductivity σ, the Seebeck coefficient S, and the electronic part of the thermal conductivity κ_e can be calculated from

$$\sigma = \mathcal{L}^{(0)}, \tag{4.11}$$

$$S = -\left(\frac{1}{eT}\right)(\mathcal{L}^{(0)})^{-1}\mathcal{L}^{(1)}, \tag{4.12}$$

$$\kappa_e = \left(\frac{1}{e^2T}\right)(\mathcal{L}^{(2)} - \mathcal{L}^{(1)}(\mathcal{L}^{(0)})^{-1}\mathcal{L}^{(1)}), \tag{4.13}$$

and the lattice thermal conductivity is calculated on the basis of the simple approximation of a kinetic theory model (see Eq. (3.20)) by replacing the phonon mean free path (MFP) with the quantum wire size, when the wire size becomes smaller than the bulk MFP for phonons. The thermoelectric figure of merit Z_{1D} is then calculated using Eq. (3.13).

4.3 $Z_{1D}T$ for Bi quantum wires with parabolic band structures at 300 K

As a first approximation, I used a parabolic dispersion relation for both the electrons and holes in Bi,

$$\varepsilon_{e,h}(\mathbf{k}) = \varepsilon^{(0)}_{e,h} \pm \frac{\hbar^2}{2}\mathbf{k}\cdot\mathbf{m}^{-1}_{e,h}\cdot\mathbf{k}, \tag{4.14}$$

where $\pm$ refers to the electrons and holes, respectively. The bulk effective mass tensor components at the Fermi level are $m^e_1 = 0.00651m_0$, $m^e_2 = 1.362m_0$, $m^e_3 = 0.0297m_0$,

[6] For bulk Bi, the quantity Δ is the band overlap $\Delta = \Delta_0 = -38$ meV, whereas $\Delta = 0$ indicates that a semimetal-semiconductor transition is achieved.

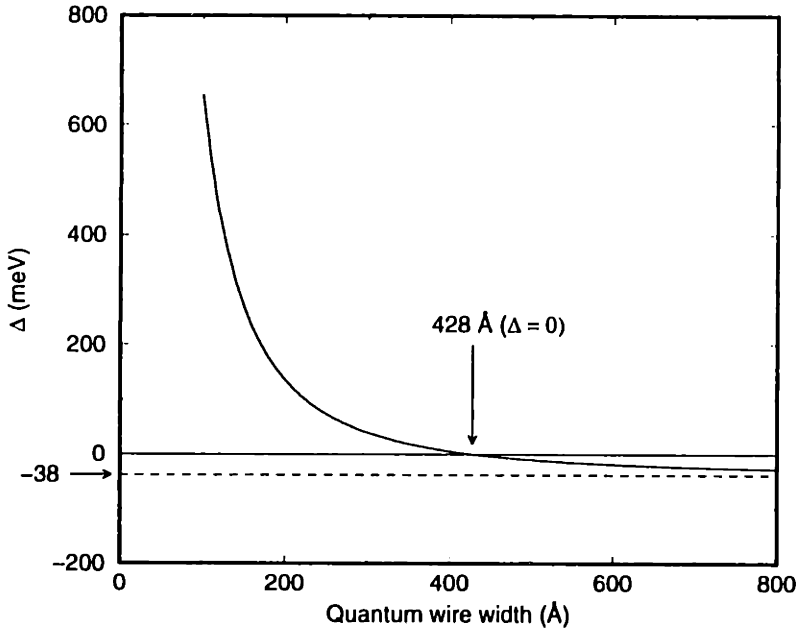

Figure 4-5: The quantum confinement-induced band gap as a function of Bi quantum wire width at 300 K for the wire along a trigonal direction, assuming a simple parabolic band model for the carriers. The conduction-valence band overlap is 38 meV for bulk bismuth. The semimetal-semiconductor transition occurs at a quantum wire width of 428 Å.

$m_1^e = 0.1635m_0$ for L-point electrons, and $m_1^h = 0.0644m_0$, $m_3^h = 0.696m_0$ for T-point holes, where m_0 is the free electron mass [47].

For simplicity, I assumed that the Bi nanowire of wire width a is square (a^2) in cross section,[7] and that the current flow is along the z, *i.e.* the trigonal, direction. The $\mathbf{k}$ vector is then quantized in the x and y directions, so that for the infinite potential for the quantum wells, $k_{x,m} = \pi/ma$ and $k_{y,n} = \pi/na$ with $m, n = 1, 2, \ldots$. The dispersion relation for the subbands are then calculated as

$$\varepsilon_{e,mn}(k_z) = \varepsilon_e^{(0)} + \frac{\hbar^2 k_{x,m}^2}{2m_1^e} + \frac{\hbar^2 k_{y,n}^2}{2m_2^e} + \frac{\hbar^2 (k_z - k_z^{(0)})^2}{2(m_3^e - m_4^{e2}/m_2^e)}, \tag{4.15}$$

for electrons and

$$\varepsilon_{h,mn}(k_z) = \varepsilon_h^{(0)} - \frac{\hbar^2 (k_{x,m}^2 + k_{y,n}^2)}{2m_1^h} - \frac{\hbar^2 k_z^2}{2m_3^h}, \tag{4.16}$$

[7]Throughout this chapter, I use a square cross section for the Bi quantum wires. For a circular cross section, a needs to be multiplied by a factor of $4/\pi$ to get the corresponding wire diameter for a simple but good approximation to the detailed solution for a circular cross section.

for holes, where

$$k_z^{(0)} = \frac{m_4^e}{m_2^e} k_{y,n} \tag{4.17}$$

indicates a shift in k-space in the conduction subband extrema due to the tilt of the principal axis of the electron ellipsoid with respect to the bisectrix axis.

Using the approximation of parabolic dispersion relations, the numerically calculated band gap Δ as a function of quantum wire width for the transport direction along the trigonal direction at room temperature yields a semimetal-semiconductor transition at a wire width of 428 Å, as shown in Fig. 4-5. As the quantum wire width becomes smaller than 200 Å, the extremal conduction and valence subband edges separate quite rapidly. The electronic transport properties for a 100 Å Bi quantum wire at room temperature are calculated using Eqs. (4.12)-(4.13) and (4.6)-(4.7). The results for σ, S and κ are shown in Figs. 4-6, 4-7 and 4-8, respectively. The corresponding dimensionless 1D thermoelectric figure of merit that is achieved using Eq. (3.13) is shown in Fig. 4-9, where we see that the maximum thermoelectric figure of merit occurs very close to the conduction subband and valence subband edges for n-type and p-type Bi quantum wires, respectively, and the maximum $Z_{1D}T$ for both n-type and p-type Bi quantum wires is over 1.0, which makes this system very interesting even for room temperature thermoelectric applications.

The thermoelectric figure of merit for various Bi nanowires with different wire widths at room temperature is shown in Fig. 4-10. The results of this simple calculation show that a value of $Z_{1D}T \sim 3.0$ could be achieved in a system with a quantum wire width of 50 Å, which is a size that may be feasible experimentally. (We have prepared samples with diameters down to 70 Å but the uniformity of the channels and the Bi filling factor of the template is not as good as for larger diameters in the 500 Å range.) The optimal[8] $Z_{1D}T$ as a function of quantum wire width is shown in Fig. 4-11. For comparison, the optimal figure of merit for a two-dimensional (2D) quantum well system is also shown [8]. This result indicates that a one-dimensional system has a greater potential for the enhancement of thermoelectric performance

[8]By placing the chemical potential at the optimum location, the system has the maximum value of $Z_{1D}T$. The placement of the chemical potential can be adjusted by varying the doping level.

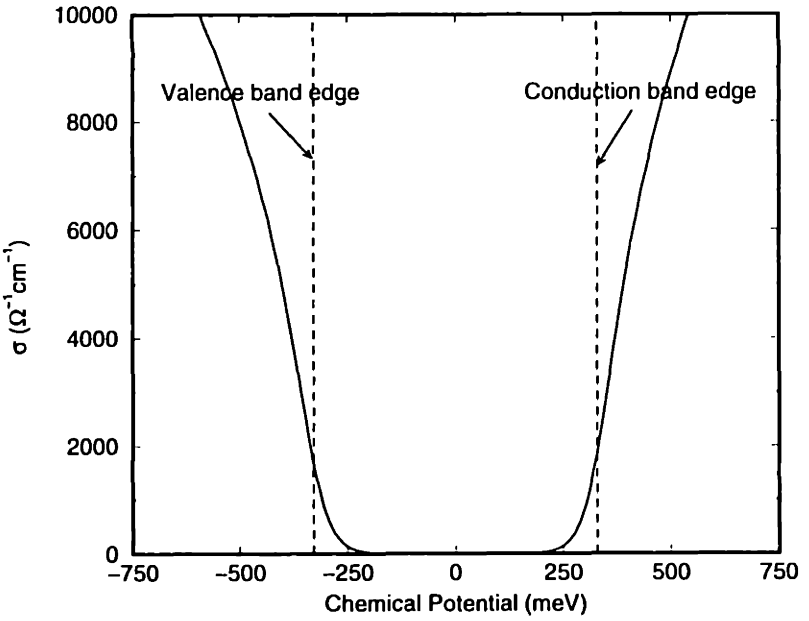

Figure 4-6: The calculated electrical conductivity for a 100 Å Bi quantum wire with transport along the trigonal axis at 300 K using a parabolic band structure approximation for the carriers.

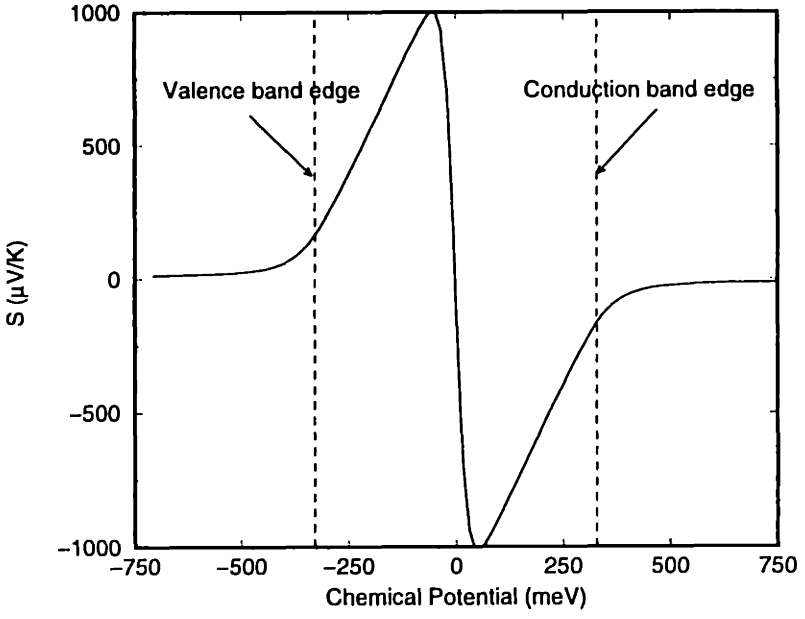

Figure 4-7: The calculated Seebeck coefficient for a 100 Å Bi quantum wire with transport along the trigonal axis at 300 K using a parabolic band structure approximation for the carriers.

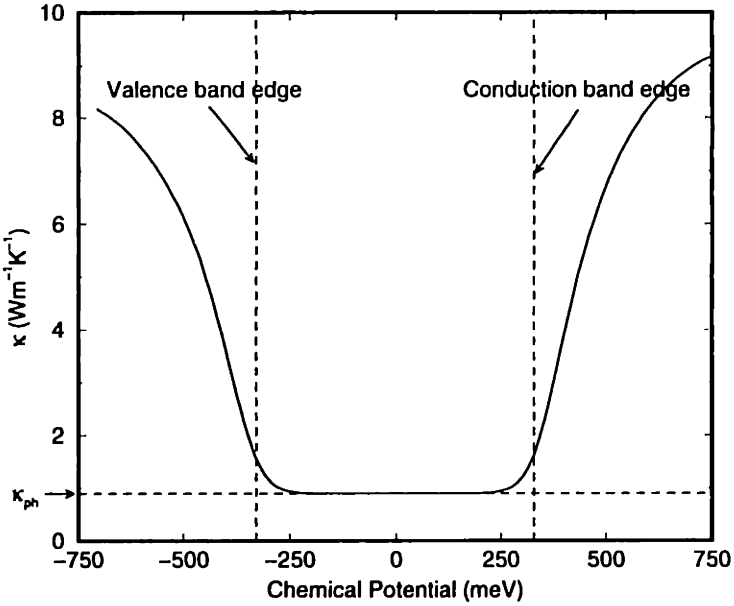

Figure 4-8: The calculated thermal conductivity for a 100 Å Bi quantum wire with transport along the trigonal direction at 300 K using a parabolic band structure approximation for the carriers. κ_{ph} indicates the contribution to the thermal conductivity from the phonons and $\kappa = \kappa_e + \kappa_{ph}$. The electron contribution to the thermal conductivity is calculated using Eq. (4.13).

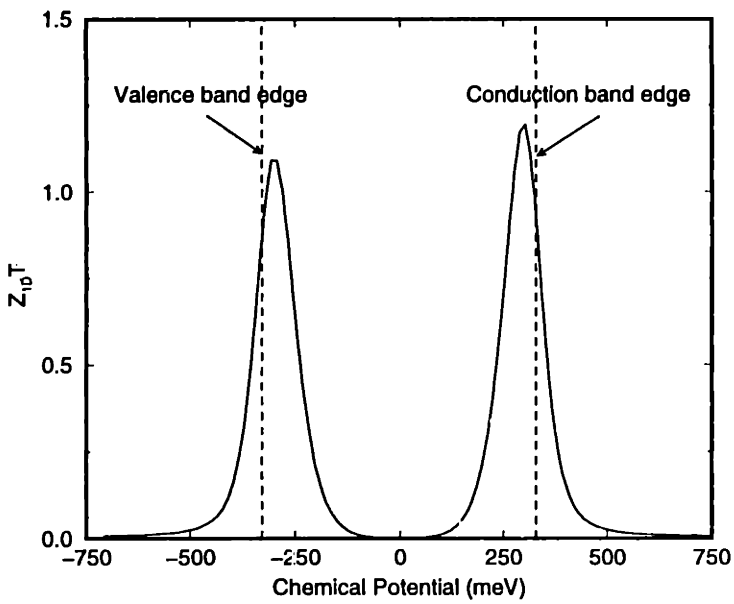

Figure 4-9: The calculated dimensionless 1D thermoelectric figure of merit $Z_{1D}T$ for a 100 Å Bi quantum wire with transport along the trigonal axis at 300 K using a parabolic band structure approximation for the carriers. The maximum thermoelectric figure of merit occurs very close to the conduction band edge and the valence band edge for n-type and p-type quantum wires, respectively.

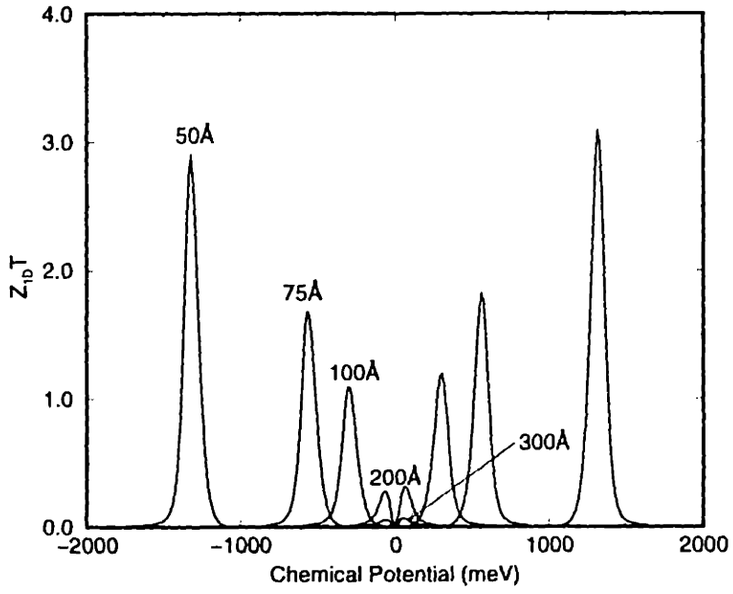

Figure 4-10: The dimensionless 1D thermoelectric figure of merit $Z_{1D}T$ as a function of chemical potential for Bi quantum wires of different sizes with transport along the trigonal axis at room temperature based on the parabolic band structure approximation for the carriers.

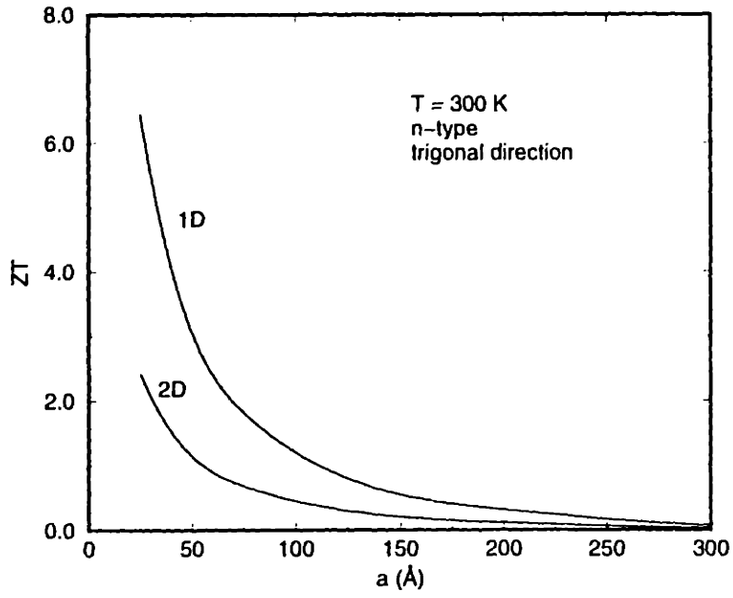

Figure 4-11: The optimal thermoelectric figure of merit for transport in the trigonal direction for n-type Bi nanowires as a function of the size of quantum wire at room temperature in the parabolic band structure approximation. For comparison, the optimal figure of merit for two-dimensional (2D) quantum well system is also shown.

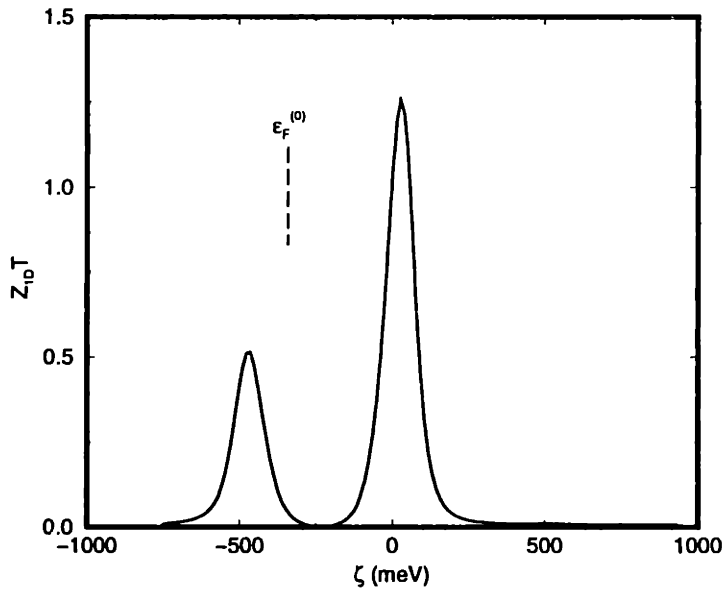

Figure 4-12: The dimensionless 1D thermoelectric figure of merit $Z_{1D}T$ as function of chemical potential for a 100 Å Bi quantum wire for transport along the bisectrix direction at room temperature, calculated on the basis of a parabolic dispersion relation. The zero point of the chemical potential is arbitrary. $\varepsilon_F^{(0)}$ indicates the Fermi level in bulk Bi.

over bulk than its two-dimensional counterpart.

Bismuth is a highly anisotropic material. It is therefore important to study the transport properties along crystal directions other than the trigonal direction. I therefore calculated the thermoelectric figure of merit for a 10 nm quantum wire with the transport along the bisectrix and binary directions, as shown in Figs. 4-12 and 4-13. We found that the n-type bisectrix nanowire has a slightly better $Z_{1D}T$ than the trigonal wire of the same wire width. However, the $Z_{1D}T$ for the p-type nanowire is much lower than that for the trigonal p-type wire due to the much smaller density of states for the holes arising from the smaller mass component along the bisectrix direction. The binary transport direction is predicted to be less favorable for n-type semiconducting bismuth, because only one of the three electron pockets strongly contributes to the power factor for this case. It is interesting to see that a very small second peak in $Z_{1D}T$ appears for the binary transport direction in the n-type range of Fig. 4-13. This small peak arises from the other two degenerate electron pockets with a higher subband edge.

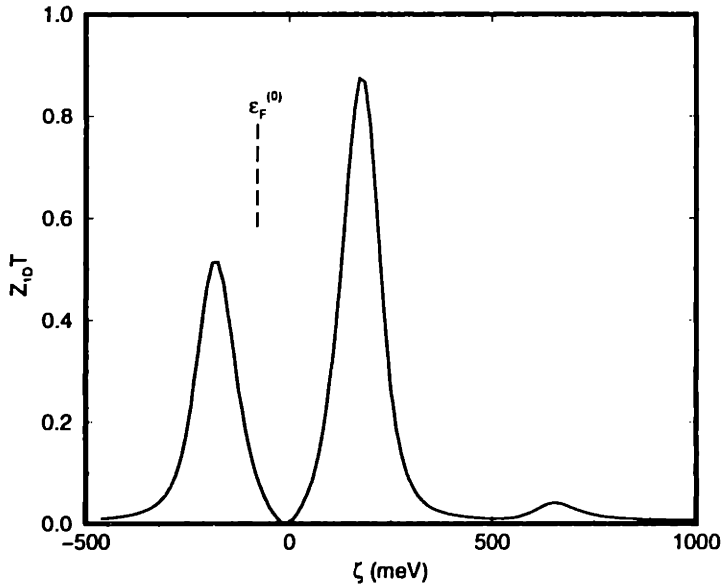

Figure 4-13: The dimensionless 1D thermoelectric figure of merit $Z_{1D}T$ as function of chemical potential for a 100 Å Bi quantum wire for transport along the binary direction at room temperature, calculated on the basis of a parabolic dispersion relation. The zero point of the chemical potential is arbitrary. $\varepsilon_F^{(0)}$ indicates the Fermi level in bulk Bi.

In this section, theoretical modeling of the thermoelectric transport properties of Bi quantum wires has been carried out based on a parabolic approximation for the basic band structure of bulk Bi. Our model calculations based on this simple approximation show that the Bi nanowire system, when appropriately doped, is potentially an interesting thermoelectric system. More detailed calculations using non-parabolic dispersion relations for the L-point electrons are needed to obtain a reliable estimation for $Z_{1D}T$. Such calculations are discussed in Sections 4.4 and 4.6.

4.4 $Z_{1D}T$ for Bi quantum wires at 77 K with non-parabolic band structures

In the previous section, I calculated the thermoelectric transport coefficients under the parabolic band approximation for both T-point holes and L-point electrons. The L-point electrons, however, are strongly coupled to the L-point holes, and are described

by highly non-parabolic dispersion relations through the Lax model [44, 46] which is based on $\mathbf{k} \cdot \mathbf{p}$ perturbation theory. Taking the L-point conduction band edge as the zero of energy, the dispersion relations for the L-point conduction (+ sign) and valence (− sign) bands becomes[9]

$$\varepsilon_{e,h}(\mathbf{k}) = -\frac{E_{gL}}{2} \pm \frac{1}{2}\sqrt{E_{gL}^2 + 2E_{gL}\hbar^2 \mathbf{k} \cdot \boldsymbol{\alpha} \cdot \mathbf{k}}, \tag{4.18}$$

where E_{gL} is the direct L-point band gap, and $\boldsymbol{\alpha}$ is the inverse effective mass tensor at the conduction band extrema of the form

$$\boldsymbol{\alpha} = \mathbf{m}_e^{-1} = \begin{pmatrix} \alpha_1 & 0 & 0 \\ 0 & \alpha_2 & \alpha_4 \\ 0 & \alpha_4 & \alpha_3 \end{pmatrix} \tag{4.19}$$

for the electron ellipsoid with its longest principal axis along a bisectrix axis. The other two electron ellipsoids are obtained by rotations of $\pm 120°$ about the trigonal axis. The elements in the $\boldsymbol{\alpha}$ tensor are related to those in the effective mass tensor by[10] $m_{e1} = \alpha_1^{-1}$, $m_{e2} = \alpha_3/\delta$, $m_{e3} = \alpha_2/\delta$, and $m_{e4} = -\alpha_4/\delta$, where $\delta = \alpha_2\alpha_3 - \alpha_4^2 > 0$. The values for the effective mass tensor elements are $m_{e1} = 0.00119\, m_0$, $m_{e2} = 0.263\, m_0$, $m_{e3} = 0.00516\, m_0$, $m_{e4} = 0.0274\, m_0$ [48], which are effective mass values at the band edge of bulk Bi. These values of the band parameters are valid up to ~80 K, above which the temperature dependence of $\boldsymbol{\alpha}$, E_{gL} and Δ_0 becomes important [39, 49]. For this reason, I present in this section theoretical modeling of the thermoelectricity of Bi nanowires at 77 K, which is a temperature of great interest for cryogenic cooling applications, and where the low temperature values of the band parameters are valid.

For the Bi nanowires[11] with transport along the z direction, *i.e.* the trigonal

[9] Since the valence band at the T-point is not strongly coupled to other T-point bands, it is a good approximation to consider the T-point holes as having a parabolic dispersion relation.

[10] $\delta > 0$ is a requirement to form a closed ellipsoidal Fermi surface around the L-point.

[11] The infinite quantum well approximation is valid for the bismuth nanowires embedded in the anodic alumina templates, because anodic alumina has a large band gap and a large barrier thickness [41].

direction, the k vector is then quantized in the x and y directions, so that $k_{x,m} = \pi/ma$ and $k_{y,n} = \pi/na$ with $m, n = 1, 2, \ldots$. The conduction subband extrema ($k_z = k_z^{(0)}$, see below) are then calculated as

$$\Delta\varepsilon_{e,mn}^{(z)} = -\frac{E_{gL}}{2} + \frac{1}{2}\sqrt{E_{gL}^2 + 2E_{gL}\hbar^2\left(\frac{k_{x,m}^2}{m_{e1}} + \frac{k_{y,n}^2}{m_{e2}}\right)}, \tag{4.20}$$

using Eq. (4.18). While calculating the transport properties in the quantum wires, it is found that only the carriers near the bottom of the subbands contribute to the transport, because the Fermi level in the system is always lower than the lowest subband edge in physical cases that are of interest. Therefore, since $\Delta\varepsilon_{e,mn}^{(z)} \gg E_{gL}$, it is a good approximation to expand the full dispersion relation derived from Eq. (4.18) into a parabolic form around the appropriate subband edge as

$$\varepsilon_{e,mn}(k_z) = \Delta\varepsilon_{e,mn}^{(z)} + \frac{\hbar^2(k_z - k_z^{(0)})^2}{2m_{e3}^*}, \tag{4.21}$$

where

$$m_{e3}^* = \left(m_{e3} - \frac{m_{e4}^2}{m_{e2}}\right)\left(1 + \frac{2\Delta\varepsilon_{e,mn}^{(z)}}{E_{gL}}\right), \tag{4.22}$$

and

$$k_z^{(0)} = \frac{m_{e4}}{m_{e2}}k_{y,n} \tag{4.23}$$

indicates the subband extrema shift in k-space due to the tilt of the principal axis of the electron ellipsoid with respect to the bisectrix axis.

For the Bi nanowires with their transport direction along the binary and bisectrix directions, the shifts in the conduction subband edges and the effective transport masses under quantum confinement conditions can be similarly derived. However, along these two directions, the three-fold degeneracy of the three electron ellipsoids will be broken into two groups, namely into the pocket labeled A and the two-fold degenerate pockets labeled B and C shown in Fig. 4-2. These two groups of pockets have different subband levels, and should be treated separately.

The following equations summarize the corresponding results for the subband

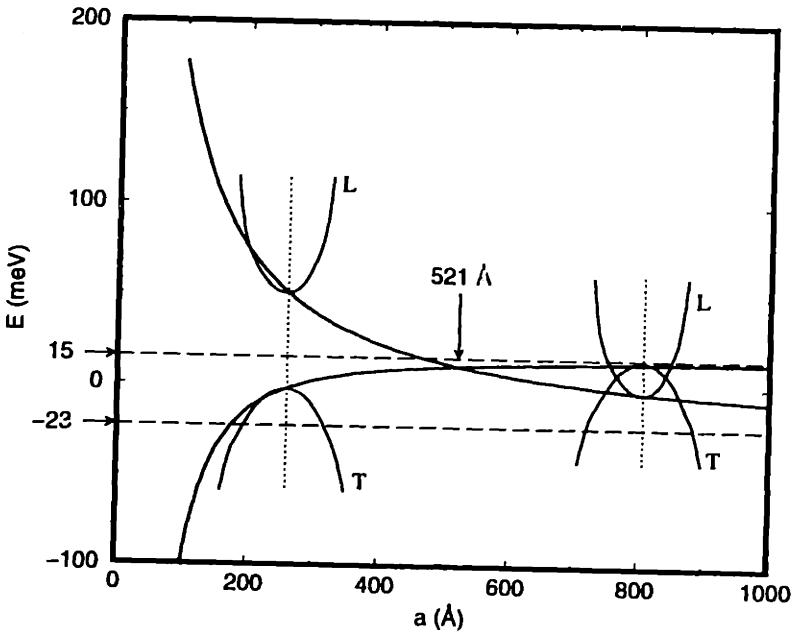

Figure 4-14: The subband structure for a Bi quantum wire along the trigonal direction under quantum confinement conditions at 77 K. The conduction subband at the L-point moves up and the valence subband at the T-point moves down, as the quantum wire size decreases. At $a_c = 521$ Å, the conduction and valence subband cross over, and a semimetal-semiconductor transition is achieved. The zero energy refers to the Fermi level in bulk Bi. The conduction band edge at the L-point for bulk Bi is at -23 meV and the valence band edge at the T-point for bulk Bi is at 15 meV.

structure along the binary and bisectrix directions. For pocket A along the binary direction, we have

$$\Delta\varepsilon_{e,mn}^{(x,A)} = -\frac{E_{gL}}{2} + \frac{1}{2}\sqrt{E_{gL}^2 + 2E_{gL}\hbar^2\left(\frac{k_{y,m}^2}{m_{e2} - \frac{m_{e4}^2}{m_{e3}}} + \frac{k_{z,n}^2}{m_{e3} - \frac{m_{e4}^2}{m_{e2}}} + \frac{2k_{y,m}k_{z,n}}{m_{e4} - \frac{m_{e2}m_{e3}}{m_{e4}}}\right)}, \tag{4.24}$$

and

$$\varepsilon_{e,mn}^{(A)}(k_x) = \Delta\varepsilon_{e,mn}^{(x,A)} + \frac{\hbar^2 k_x^2}{2m_{e1,A}^*}, \tag{4.25}$$

where

$$m_{e1,A}^* = m_{e1}\left(1 + \frac{2\Delta\varepsilon_{e,mn}^{(x,A)}}{E_{gL}}\right). \tag{4.26}$$

For pockets B and C along the binary direction, we have

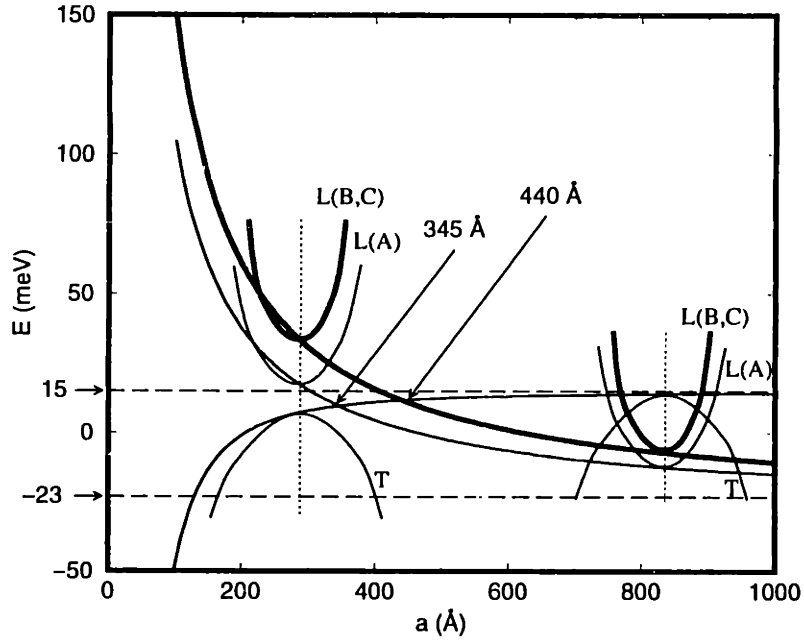

Figure 4-15: The subband structure for a Bi quantum wire along the binary direction under quantum confinement conditions at 77 K, showing the lowest subbands for the A and B, C electron carrier pockets at the L-point as well as the highest hole subband at the T-point. The conduction subbands at the L-point move up and the valence subbands at the T-point move down, as the quantum wire size decreases. The electron pocket A forms a lower conduction subband, while the electron pockets B and C form a two-fold degenerate subband at a higher energy level. At $a_c = 345\,\text{Å}$, the conduction ($L(A)$) and T-point valence subbands cross over, and a semimetal-semiconductor transition is achieved. The zero energy refers to the Fermi level in bulk Bi. The conduction band edge at the L-point for bulk Bi is at -23 meV and the valence band edge at the T-point for bulk Bi is at 15 meV.

$$\Delta\varepsilon_{e,mn}^{(x,BC)} = -\frac{E_{gL}}{2} + \frac{1}{2}\left[E_{gL}^2 + 2E_{gL}\hbar^2\left(\frac{k_{y,m}^2}{\frac{3}{4}m_{e1} + \frac{1}{4}m_{e2} - \frac{m_{e4}^2}{4m_{e3}}} + \frac{k_{z,n}^2}{m_{e3} - \frac{m_{e4}^2}{3m_{e1}+m_{e2}}} + \frac{4k_{y,m}k_{z,n}}{\frac{(3m_{e1}+m_{e2})m_{e3}}{m_{e4}} - m_{e4}}\right)\right]^{\frac{1}{2}}, \quad (4.27)$$

and

$$\varepsilon_{e,mn}^{(BC)}(k_x) = \Delta\varepsilon_{e,mn}^{(x,BC)} + \frac{\hbar^2(k_x - k_{x,BC}^{(0)})^2}{2m_{e1,BC}^*}, \quad (4.28)$$

where

$$m_{e1,BC}^* = \left[\frac{4m_{e1}(m_{e2}m_{e3} - m_{e4}^2)}{(3m_{e1} + m_{e2})m_{e3} - m_{e4}^2}\right]\left(1 + \frac{2\Delta\varepsilon_{e,mn}^{(x,BC)}}{E_{gL}}\right), \quad (4.29)$$

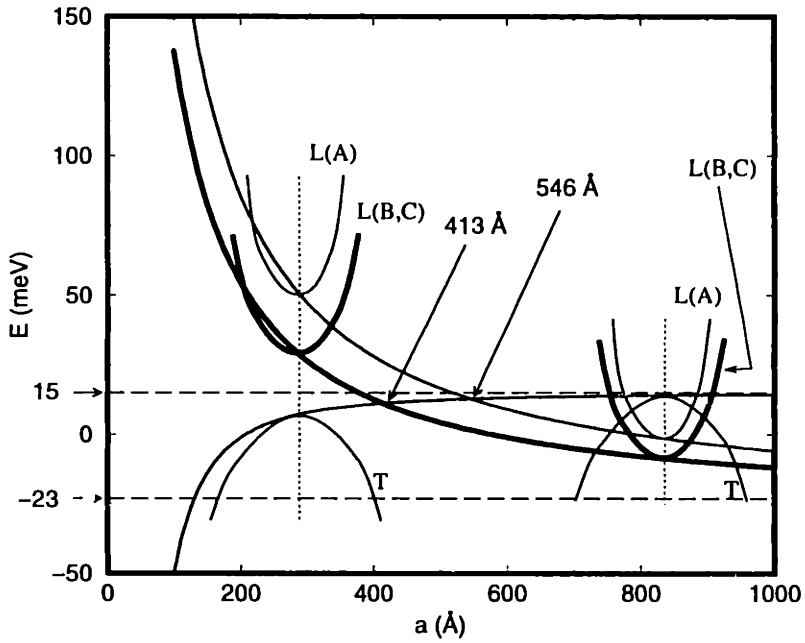

Figure 4-16: The subband structure for a Bi quantum wire along the bisectrix direction under quantum confinement conditions at 77 K, showing the lowest subbands for the A and B, C electron carrier pockets at the L-point as well as the highest hole subband at the T-point. The conduction subbands at the L-point move up and the valence subbands at the T-point move down, as the quantum wire size decreases. The electron pocket A forms a higher conduction subband, while the electron pockets B and C form a two-fold degenerate subband at a lower energy level. At $a_c = 413\,\text{Å}$, the conduction ($L(B, C)$) and T-point valence subbands cross over, and a semimetal-semiconductor transition is achieved. The zero energy refers to the Fermi level in bulk Bi. The conduction band edge at the L-point for bulk Bi is at -23 meV and the valence band edge at the T-point for bulk Bi is at 15 meV.

and

$$k_{x,BC}^{(0)} = \frac{\sqrt{3}[(m_{e1} - m_{e2})m_{e3} + m_{e4}^2]}{(3m_{e1} + m_{e2})m_{e3} - m_{e4}^2} k_{y,m} + \frac{2\sqrt{3}m_{e1}m_{e4}}{(3m_{e1} + m_{e2})m_{e3} - m_{e4}^2} k_{z,n}. \tag{4.30}$$

For pocket A along the bisectrix direction, we have

$$\Delta\varepsilon_{e,mn}^{(y,A)} = -\frac{E_{gL}}{2} + \frac{1}{2}\sqrt{E_{gL}^2 + 2E_{gL}\hbar^2\left(\frac{k_{x,m}^2}{m_{e1}} + \frac{k_{z,n}^2}{m_{e3}}\right)}, \tag{4.31}$$

and

$$\varepsilon_{e,mn}^{(A)}(k_y) = \Delta\varepsilon_{e,mn}^{(y,A)} + \frac{\hbar^2(k_y - k_{y,A}^{(0)})^2}{2m_{e2,A}^*}, \tag{4.32}$$

where

$$m^*_{e2,A} = \left(m_{e2} - \frac{m^2_{e4}}{m_{e3}}\right)\left(1 + \frac{2\Delta\varepsilon^{(y,A)}_{e,mn}}{E_{gL}}\right), \tag{4.33}$$

and

$$k^{(0)}_{y,A} = \frac{m_{e4}}{m_{e3}} k_{z,n}. \tag{4.34}$$

For pockets B and C along the bisectrix direction, we have

$$\Delta\varepsilon^{(y,BC)}_{e,mn} = -\frac{E_{gL}}{2} + \frac{1}{2}\left[E^2_{gL} + 2E_{gL}\hbar^2\left(\frac{k^2_{x,m}}{\frac{1}{4}m_{e1} + \frac{3}{4}m_{e2} - \frac{3m^2_{e4}}{4m_{e3}}} + \frac{k^2_{z,n}}{m_{e3} - \frac{3m^2_{e4}}{m_{e1}+3m_{e2}}} + \frac{4\sqrt{3}k_{x,m}k_{z,n}}{\frac{(m_{e1}+3m_{e2})m_{e3}}{m_{e4}} - 3m_{e4}}\right)\right]^{\frac{1}{2}}, \tag{4.35}$$

and

$$\varepsilon^{(BC)}_{e,mn}(k_y) = \Delta\varepsilon^{(y,BC)}_{e,mn} + \frac{\hbar^2(k_y - k^{(0)}_{y,BC})^2}{2m^*_{e2,BC}}, \tag{4.36}$$

where

$$m^*_{e2,BC} = \left[\frac{4m_{e1}(m_{e2}m_{e3} - m^2_{e4})}{(m_{e1} + 3m_{e2})m_{e3} - 3m^2_{e4}}\right]\left(1 + \frac{2\Delta\varepsilon^{(y,BC)}_{e,mn}}{E_{gL}}\right), \tag{4.37}$$

and

$$k^{(0)}_{y,BC} = \frac{\sqrt{3}[(m_{e1} - m_{e2})m_{e3} + m^2_{e4}]}{(m_{e1} + 3m_{e2})m_{e3} - 3m^2_{e4}} k_{x,m} - \frac{2m_{e1}m_{e4}}{(m_{e1} + 3m_{e2})m_{e3} - 3m^2_{e4}} k_{z,n}. \tag{4.38}$$

As quantum confinement is introduced into the Bi nanowire system by decreasing a, the extremal conduction and valence subband edges move in opposite directions to eventually form a positive energy band gap Δ between the lowest L-point conduction subband edge and the highest T-point valence subband edge, thereby leading to a semimetal-semiconductor transition (where $\Delta = 0$) as the wire size is decreased below a_c. Figures 4-14, 4-15, and 4-16 show the subband structures for the Bi quantum wires along the trigonal, binary and bisectrix directions, respectively. The zero energy in these figures refers to the Fermi level for bulk Bi. Therefore the conduction band edge at the L-point for bulk Bi is at -23 meV and the valence band edge at the T-point for bulk Bi is at 15 meV. For trigonal wires, the three electron pockets at the L-point form

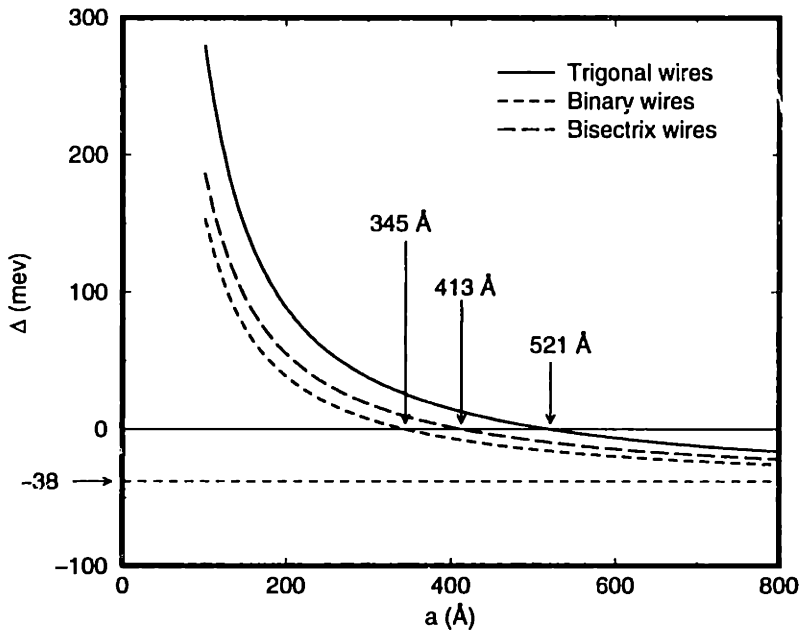

Figure 4-17: The quantum confinement-induced band gap as a function of Bi quantum wire width at 77 K. The conduction-valence band overlap is 38 meV in bulk form. The semimetal-semiconductor transition ($\Delta = 0$) occurs at a quantum wire width of 521 Å for trigonal wires, 345 Å for binary wires, and 413 Å for bisectrix wires. The band gap for binary and bisectrix wires is the separation of the T-point valence subband edge and the lower L-point conduction subband after the lifting of the three-fold degeneracy of the electron ellipsoids.

a three-fold degenerate subband. At $a_c = 521$ Å, the conduction and valence subband cross over, and a semimetal-semiconductor transition is achieved. For binary wires, the degeneracy of the three electron pockets at the L-point is lifted. The electron pocket A (see Fig. 4-2) forms a lower conduction subband, while the electron pockets B and C form a two-fold degenerate subband at a higher energy level. At $a_c = 345$ Å, the lower lying conduction $L(A)$-subband crosses the T-point valence subband, and a semimetal-semiconductor transition is achieved. For bisectrix wires, the degeneracy of the three electron pockets at the L-point is also lifted by quantum confinement. The electron pocket A forms a higher conduction subband, while the electron pockets B and C form a two-fold degenerate subband at a lower energy level. At $a_c = 413$ Å, the conduction $L(B, C)$-subband crosses the T-point valence subband crossover, and a semimetal-semiconductor transition is achieved.

Figure 4-17 shows the numerically calculated quantum confinement-induced band gap Δ as a function of Bi quantum wire width for transport along the three principal crystalline directions at 77 K. The semimetal-semiconductor transition ($\Delta = 0$) occurs at a quantum wire width of 521 Å for trigonal wires, 345 Å for binary wires, and 413 Å for bisectrix wires. The band gap for binary and bisectrix wires is the separation between the highest T-point valence subband edge and the lowest L-point conduction subband after the lifting of the three-fold degeneracy of the electron ellipsoids. As a becomes smaller than 200 Å (see Fig. 4-17), the conduction and valence extremal subband edges separate quite rapidly.

It is important to note that the dispersion relations for electrons under quantum confinement conditions given by Eqs. (4.21), (4.25), (4.28), (4.32), and (4.36) is approximated by a parabolic form with new transport effective mass values defined in Eqs. (4.22), (4.26), (4.29), (4.33), and (4.37), which reflect the non-parabolicity of the conduction band. Therefore, the formalism derived in Section 4.2 can be applied directly after replacing the transport effective mass appropriate to the subband extrema.

The calculated σ, S and κ for a 100 Å Bi wire along the trigonal direction are shown in Figs. 4-18, 4-19 and 4-20, respectively. The corresponding dimensionless 1D thermoelectric figure of merit $Z_{1D}T$ that is achieved using Eq. (3.13) is shown in Fig. 4-21. Figures 4-22 and 4-23 show the $Z_{1D}T$ results for a 100 Å Bi quantum wire along the binary and bisectrix directions, respectively. The maximum $Z_{1D}T$ occurs for $\zeta^*_{e,h}$ very close to the conduction subband and valence subband edges for n-type and p-type Bi quantum wires, respectively. For the optimized n-type trigonal quantum wire, the value of $Z_{1D}T$ is almost 1.43 for $a = 100$ Å, while for the p-type trigonal quantum wire,[12] the optimal $Z_{1D}T$ is only 0.12, reflecting the difference in the L-point and T-point band parameters.

The optimal $Z_{1D}T$ values versus the quantum wire width at 77 K are shown in

[12]Do not confuse this value at 77 K with that shown in Fig. 4-9, which is for 300 K. At such a low temperature as 77 K, the lattice thermal conductivity is much larger than that at 300 K. See Section 4.6 for discussions of $Z_{1D}T$ at 300 K considering the non-parabolic band structure of Bi.

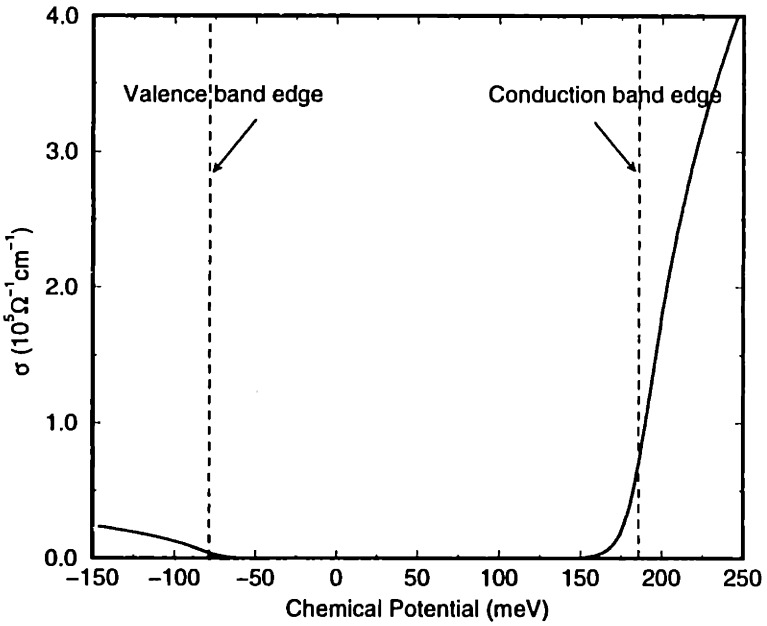

Figure 4-18: The calculated electrical conductivity for a 100 Å Bi quantum wire with transport along the trigonal axis at 77 K, considering a non-parabolic model for the conduction band at the L-point.

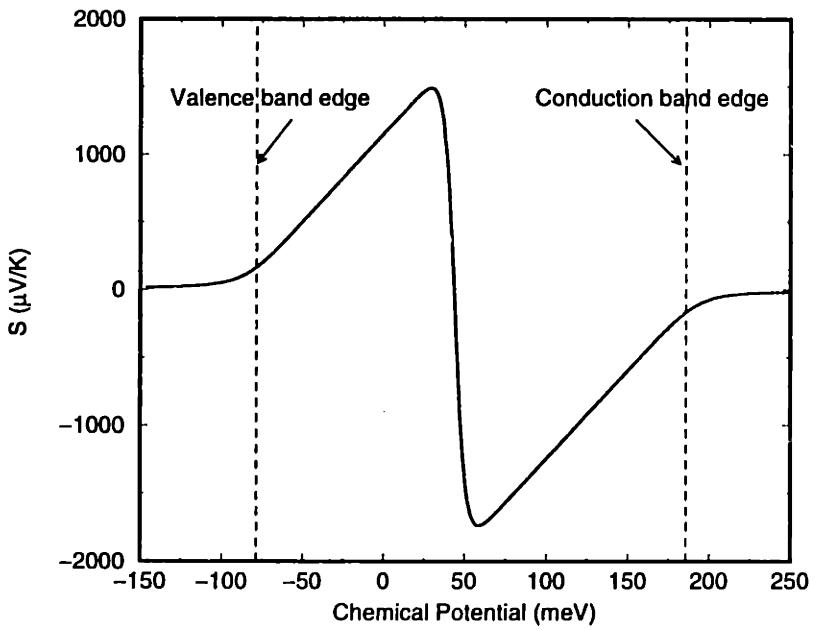

Figure 4-19: The calculated Seebeck coefficient for a 100 Å Bi quantum wire with transport along the trigonal axis at 77 K, considering a non-parabolic model for the conduction band at the L-point.

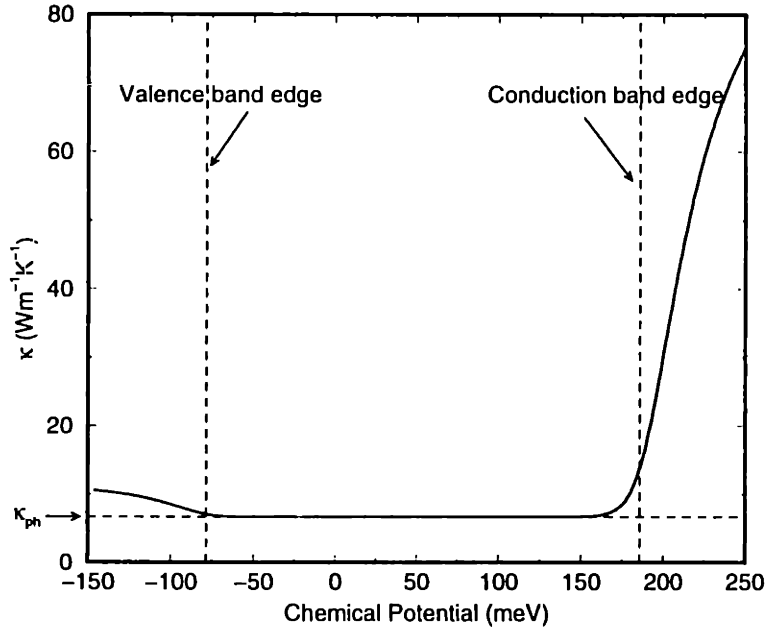

Figure 4-20: The calculated thermal conductivity for a 100 Å Bi quantum wire with transport along the trigonal direction at 77 K, considering a non-parabolic model for the conduction band at the L-point. κ_{ph} indicates the contribution to the thermal conductivity from the phonons and $\kappa = \kappa_e + \kappa_{ph}$. The electron contribution to the thermal conductivity is calculated using Eq. (4.13).

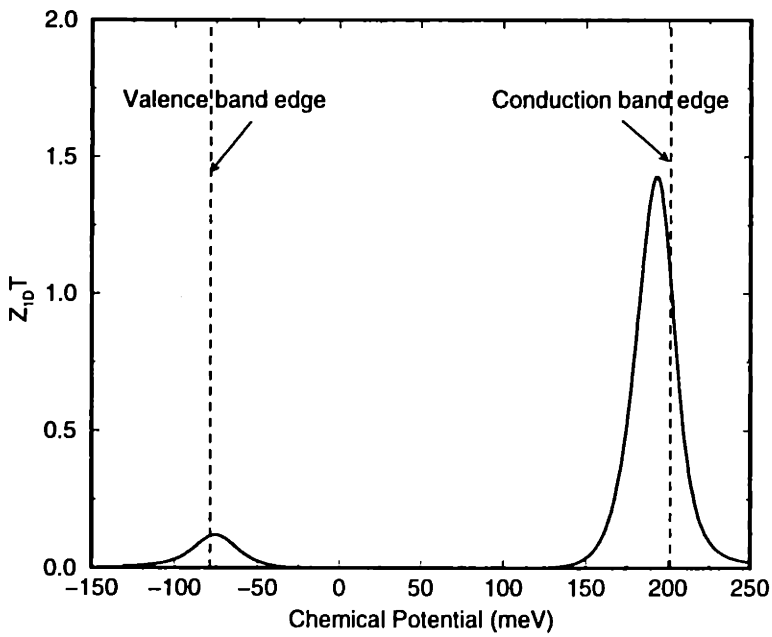

Figure 4-21: Calculated $Z_{1D}T$ versus chemical potential ζ for a 100 Å Bi quantum wire at 77 K along the trigonal direction using semiclassical transport theory. The maximum dimensionless 1D thermoelectric figure of merit $Z_{1D}T$ occurs very close to the L-point conduction band and the T-point valence band edges.

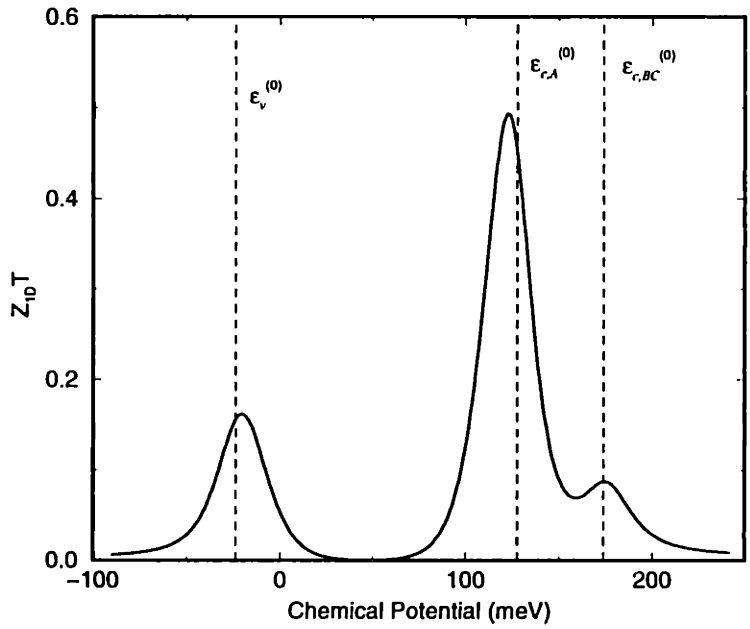

Figure 4-22: The thermoelectric figure of merit as a function of chemical potential for a 100 Å Bi quantum wire for transport along the binary direction at 77 K. The dashed lines are the positions of the valence subband edge ($\varepsilon_v^{(0)}$), the electron A subband edge ($\varepsilon_{c,A}^{(0)}$), and the electron B, C subband edge ($\varepsilon_{c,BC}^{(0)}$).

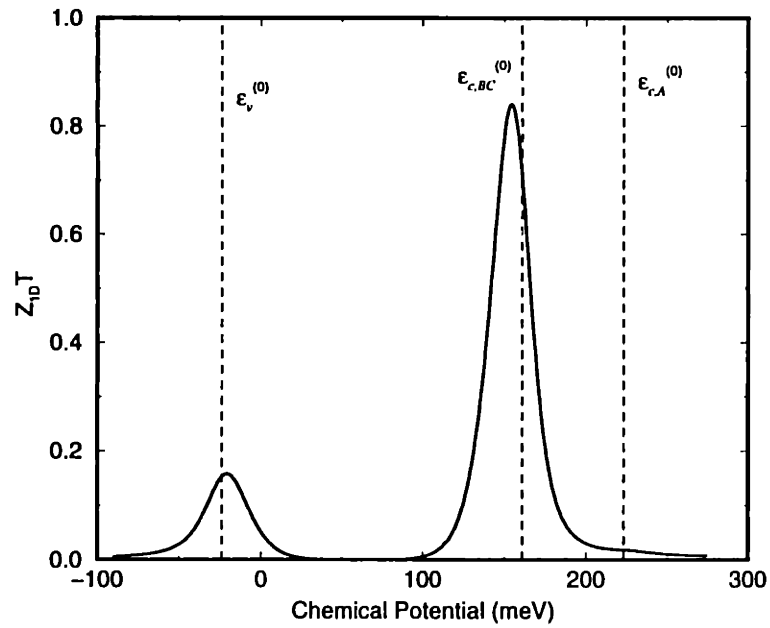

Figure 4-23: The thermoelectric figure of merit as a function of chemical potential for a 100 Å Bi quantum wire for transport along the bisectrix direction at 77 K. The dashed lines are the positions of the valence subband edge ($\varepsilon_v^{(0)}$), the electron A subband edge ($\varepsilon_{c,A}^{(0)}$), and the electron B, C subband edge ($\varepsilon_{c,BC}^{(0)}$).

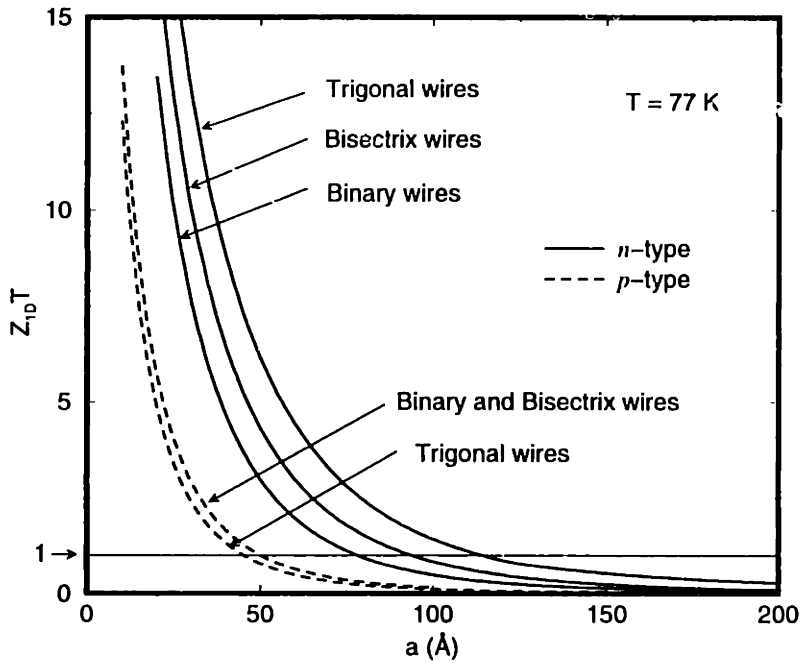

Figure 4-24: The optimal thermoelectric figure of merit as a function of quantum wire width, a, at 77 K for both n-type and p-type Bi nanowires oriented along the three principal crystalline directions.

Fig. 4-24 for both n-type (solid curves) and p-type (dashed curves) Bi nanowires. Experimentally, Bi nanowires with larger wire widths are easier to fabricate. Therefore, it is desirable to achieve a given value of $Z_{1D}T$ with a relatively larger quantum wire size. If we use $Z_{1D}T = 1$ as a benchmark, the corresponding Bi quantum wire sizes for both n-type and p-type along the principal crystalline directions are listed in Table 4.1. We see that for n-type Bi quantum wires, the trigonal direction is the most favorable, while the binary direction is the least favorable. For p-type Bi quantum wires, there is not much difference between the trigonal and the binary (bisectrix) directions, although the binary (bisectrix) direction is slightly better.

The optimum carrier concentrations corresponding to the optimal chemical potential (or doping level) for maximum $Z_{1D}T$ are presented in Fig. 4-25 as a function of quantum wire thickness a at 77 K for both n-type (solid curve) and p-type (dashed curve) Bi nanowires along the three principal crystalline orientations. For n-type Bi quantum wires along the trigonal direction, the three electron pockets at the L-point are equally populated. For n-type Bi quantum wires along the binary direction, the

Table 4.1: Bi quantum wire widths along the principal crystalline directions at 77 K corresponding to the $Z_{1D}T = 1$ benchmark value. For p-type Bi quantum wires, the binary and bisectrix directions have the same value for the wire width because of the cylindrical symmetry about the trigonal axis of the hole ellipsoid at the T-point.

	Trigonal	Binary	Bisectrix
n-type	114 Å	78 Å	94 Å
p-type	45 Å	50 Å	50 Å

the electron pocket A at the L-point is significantly populated. For n-type Bi quantum wires along the bisectrix direction, the the electron pockets B and C at the L-point are significantly populated. For p-type Bi quantum wires, however, there is only one hole pocket at the T-point for all the three directions. The quantum wire sizes shown in Fig. 4-25 are within the range of 1D semiconductors. Therefore, the intrinsic, or undoped, Bi quantum wires have a very low level of carrier concentration.[13] However, the carrier concentrations for optimal $Z_{1D}T$ values shown in Fig. 4-25 are in a feasible range for most doped semiconductors. Therefore, we expect that these doping levels can be achieved experimentally.

In this section, theoretical modeling of the thermoelectric transport properties has been carried out based on the basic non-parabolic band structure of bulk Bi at 77 K. My model calculations show that Bi nanowires, when appropriately doped, are potentially interesting for thermoelectric applications. Since band structure parameters of Bi are strongly temperature dependent above 80 K, more detailed results on the dependence of $Z_{1D}T$ on temperature will be discussed in the next section.

4.5 The temperature dependent properties of Bi

The band structure parameters are strongly temperature dependent at temperatures above 80 K and extending up to 300 K and beyond. In this section, I itemize the relevant band structure parameters and a few other physical properties that are used

[13]For example, an intrinsic 100 Å trigonal wire has a carrier density of 4.05×10^{9} cm^{-3} at 77 K for both electrons and holes (see Appendix A).

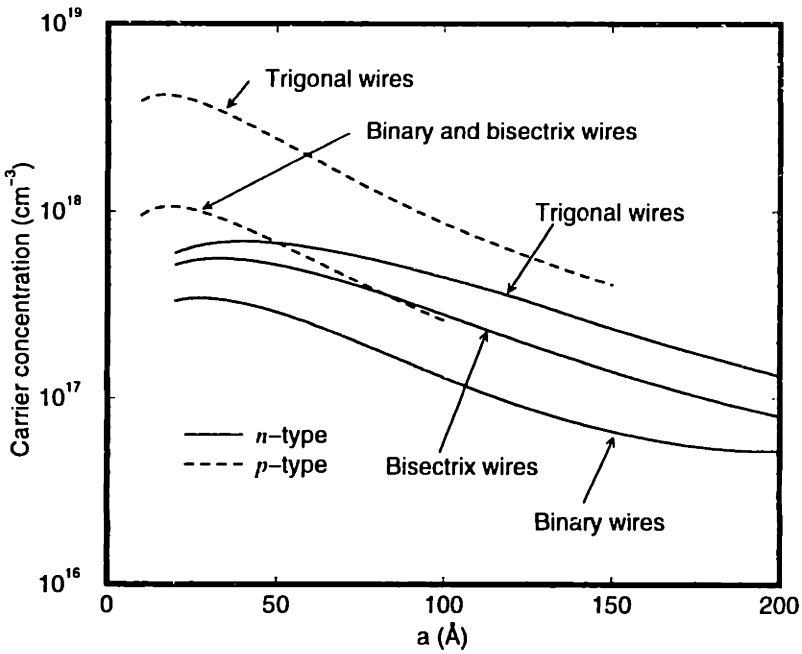

Figure 4-25: The optimum carrier concentrations corresponding to the optimal chemical potential as a function of quantum wire width, a, at 77 K for both n-type and p-type Bi nanowires oriented along the three principal crystalline directions.

in the calculations at temperatures above 80 K. They are all empirical equations based on data from the literature.

- The band overlap Δ_0 between the conduction band minimum at the L-point and the valence band maximum at the T-point in the Brillouin zone. The value of Δ_0 is negative, and is almost constant below 80 K. As the temperature increases, the overlap Δ_0 increases, and can be expressed empirically by [39]

$$\Delta_0 = \begin{cases} -38 \text{ (meV)} & (T < 80\text{K}) \\ -38 - 0.044(T-80) + 4.58 \times 10^{-4}(T-80)^2 & \\ \qquad -7.39 \times 10^{-6}(T-80)^3 \text{ (meV)} & (T > 80\text{K}) \end{cases} \tag{4.39}$$

- The direct band gap E_{gL} at the L-point in the Brillouin zone. At zero temperature, E_{gL} is 13.6 meV, and increases monotonically as a function of temperature.

It is experimentally determined as [49]

$$E_{gL} = 13.6 + 2.1 \times 10^{-3}T + 2.5 \times 10^{-4}T^2 \text{ (meV)}. \tag{4.40}$$

- The effective mass component for electrons are also sensitive to temperature above 80 K. The cyclotron effective masses along different principal directions were determined by magneto-optics. The mass values increase monotonically as a function of temperature, and can be expressed by [48, 49]

$$(\mathbf{m}_e(T))_{ij} = \frac{(\mathbf{m}_e(0))_{ij}}{1 - 2.94 \times 10^{-3}T + 5.56 \times 10^{-7}T^2}, \tag{4.41}$$

where $\mathbf{m}_e(0)$ is the effective mass tensor at $T = 0$ K.

- The lattice thermal conductivity is not only temperature dependent, but is also anisotropic. The lattice thermal resistivity is a monotonic ascending function of temperature, and can be expressed as [39]

$$(\kappa_{ph}^{-1})_{\|} = 0.036 - 6.09 \times 10^{-4}T + 1.46 \times 10^{-5}T^2 \text{ (mK/W)}, \tag{4.42}$$

$$(\kappa_{ph}^{-1})_{\perp} = -0.089 + 1.52 \times 10^{-3}T + 2.43 \times 10^{-6}T^2 \text{ (mK/W)}, \tag{4.43}$$

where the subscripts $\|$ and $\perp$ denote directions parallel and perpendicular to the trigonal axis. Note that these equations are functions that are empirically fitted to experimental data for temperatures between 100 K and 300 K, and are not valid for very low temperatures.

- The carrier mobility tensor elements are also temperature dependent. For the electrons, the mobility tensor is of the form

$$\boldsymbol{\mu}_e = \begin{pmatrix} \mu_{e1} & 0 & 0 \\ 0 & \mu_{e2} & \mu_{e4} \\ 0 & \mu_{e4} & \mu_{e3} \end{pmatrix}. \tag{4.44}$$

Table 4.2: The heat capacity C_v and sound velocities v of Bi.

T (K)	1.6	77	300
C_v ($JK^{-1}cm^{-3}$)	-	1.003	1.214
v (10^5 cm/s) (Binary)	2.62	-	2.540
v (10^5 cm/s) (Bisectrix)	2.70	-	2.571
v (10^5 cm/s) (Trigonal)	2.02	-	1.972

For the holes, the mobility tensor is of the form

$$\boldsymbol{\mu}_h = \begin{pmatrix} \mu_{h1} & 0 & 0 \\ 0 & \mu_{h1} & 0 \\ 0 & 0 & \mu_{h3} \end{pmatrix}, \tag{4.45}$$

in which the elements are the same (μ_{h1}) along the binary and bisectrix directions. The mobility of each tensor element changes with temperature as

$$(\boldsymbol{\mu}_{e,h})_{ij} = (\boldsymbol{\mu}^{(0)}_{e,h})_{ij} T^{-\lambda^{e,h}_{ij}}. \tag{4.46}$$

The empirical equations for each tensor element are listed below [50]:

$$\mu_{e1} = 1.05 \times 10^6 T^{-2.22} \ (m^2 V^{-1} s^{-1}) \tag{4.47}$$

$$\mu_{e2} = 6.91 \times 10^4 T^{-2.46} \ (m^2 V^{-1} s^{-1}) \tag{4.48}$$

$$\mu_{e3} = 1.74 \times 10^6 T^{-2.47} \ (m^2 V^{-1} s^{-1}) \tag{4.49}$$

$$\mu_{e4} = -1.09 \times 10^5 T^{-2.33} \ (m^2 V^{-1} s^{-1}) \tag{4.50}$$

$$\mu_{h1} = 2.27 \times 10^5 T^{-2.27} \ (m^2 V^{-1} s^{-1}) \tag{4.51}$$

$$\mu_{h3} = 3.10 \times 10^2 T^{-1.15} \ (m^2 V^{-1} s^{-1}) \tag{4.52}$$

- The heat capacity C_v and sound velocities v are used to estimate the phonon mean free path via Eq. (3.20). These quantities depend only slightly on the temperature. Experimental values for these quantities are available for C_v at

77 K and 300 K [51], and for v at 1.6 K [52] and 300 K [53]. These values are listed in Table 4.2, and linear interpolations of these values are used for other temperatures.

4.6 The temperature dependent study of the thermoelectric transport properties of Bi quantum wires

Considering the temperature dependent band structure parameters, the first noticeable feature is that the quantum confinement becomes temperature dependent. Because of the increase of the band overlap and in the electron effective mass components at higher temperatures, it is harder to get a quantum confinement induced semimetal-semiconductor transition at higher temperatures. Figure 4-26 shows the critical quantum wire width a_c at which the semimetal-semiconductor transition occurs versus temperature for Bi quantum wires with different orientations. We see that for all the three principal crystalline orientations, a smaller wire size is needed at higher temperatures in order to get a semimetal-semiconductor transition. At $T = 300$ K, the semimetal-semiconductor transition occurs at a quantum wire width of 172 Å for trigonal wires, 119 Å for binary wires, and 133 Å for bisectrix wires. Compared to the case at 77 K, the critical quantum wire width a_c for a quantum confinement induced semimetal-semiconductor transition is considerably reduced.

The one-dimensional thermoelectric figure of merit $Z_{1D}T$ for a 100 Å Bi quantum wire along the trigonal direction is calculated as a function of the chemical potential at 300 K, and the results are shown in Fig. 4-27. For the n-type wire, similar to the case at 77 K, the optimal chemical potential for maximum $Z_{1D}T$ is below but very close to the conduction subband edge (see Fig. 4-21), yielding a value of $Z_{1D}T$ of 1.73. However, for a p-type wire, the optimal chemical potential for maximum $Z_{1D}T$ lies "higher" inside the valence subband. This is because the electrons that are thermally excited from the conduction band are making a negative contribution to

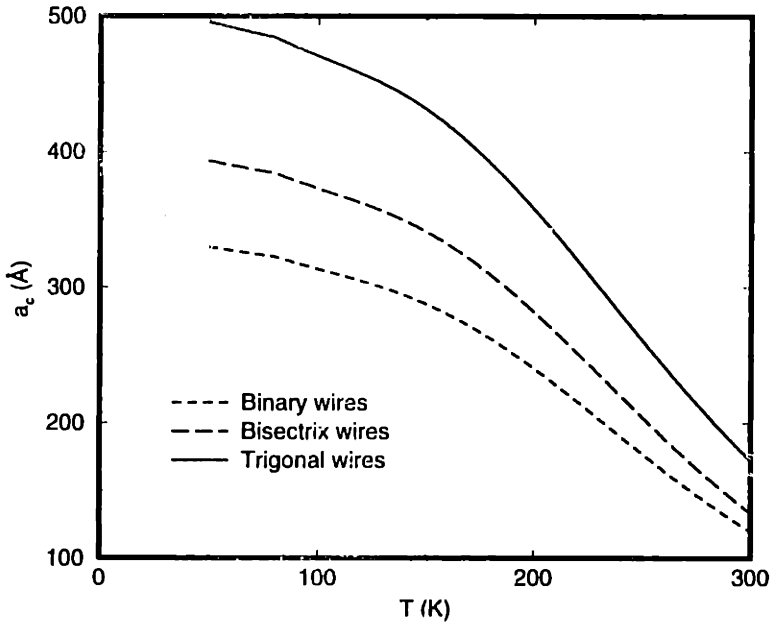

Figure 4-26: The critical quantum wire width a_c at which the semimetal-semiconductor transition occurs versus temperature for Bi quantum wires with different orientations.

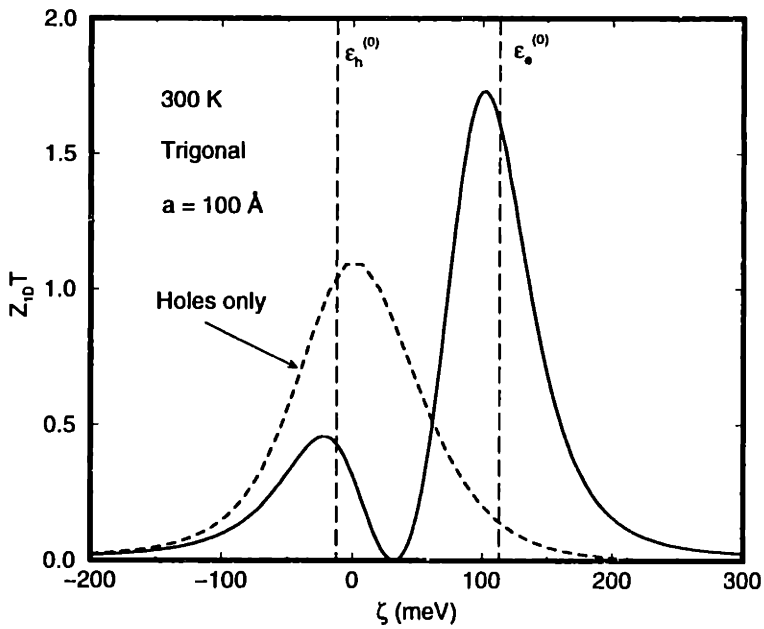

Figure 4-27: Calculated $Z_{1D}T$ versus the chemical potential ζ for a 100 Å Bi quantum wire along the trigonal direction at 300 K. Because the conduction band and valence are very close to each other, the electrons affect the thermoelectric transport for p-type wires, even though the electrons are minority carriers. The dashed curve shows $Z_{1D}T$ without any influence from the thermally excited electrons.

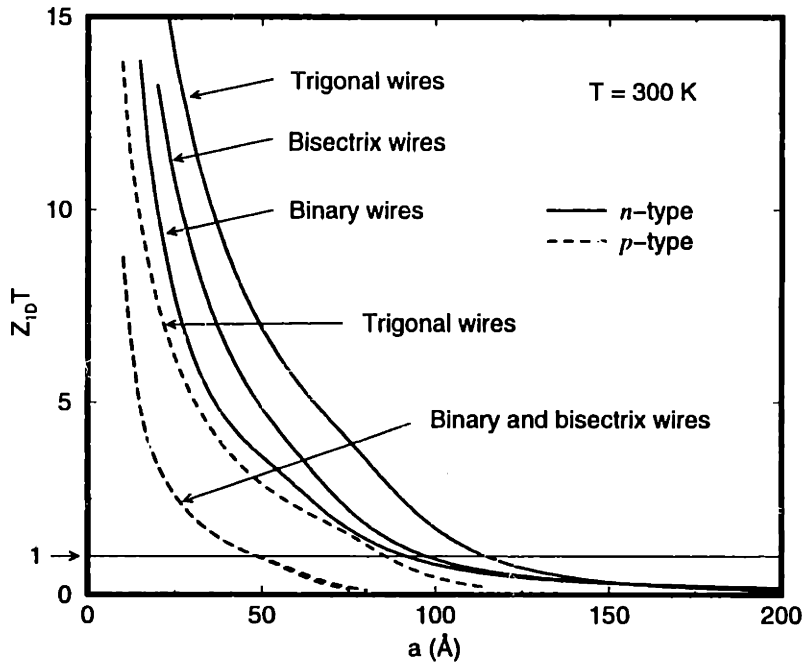

Figure 4-28: The optimal thermoelectric figure of merit as a function of quantum wire width, a, at 300 K for both n-type and p-type Bi nanowires oriented along the three principal crystalline directions. Note that for p-type wires along the binary and bisectrix directions, the difference in Z_{1D}T becomes distinguishable for wire sizes larger than 50 Å. This is because of the greater influence of thermally excited electrons on the hole transport.

the thermoelectric transport of holes. If we calculate $Z_{1D}T$ without considering the contribution for the electrons, we get $Z_{1D}T$ as a function of the chemical potential shown in Fig. 4-27 with the dashed curve. This result is similar to that shown in Fig. 4-9, in which the conduction subband and the valence subband are far apart in energy so that the influence of the electrons on the hole transport is negligible. This result implies that by considering temperature dependent band parameters, the band gap under quantum confinement conditions becomes so small that the importance of using the two-band model becomes more necessary. This effect reduces the optimal $Z_{1D}T$ value for p-type 100 Å Bi quantum wires at T = 300 K from 1.08 to 0.46, a 57% reduction.

The optimal $Z_{1D}T$ values versus the quantum wire width at 300 K are shown in Fig. 4-28 for both n-type (solid curves) and p-type (dashed curves) Bi nanowires. It is seen that p-type quantum wires along the binary and bisectrix directions have the

Table 4.3: The wire width of Bi quantum wires corresponding to the $Z_{1D}T = 1$ benchmark value along the principal crystalline directions at 300 K. Note that there is a small difference in the wire size for p-type Bi quantum wires along the binary and bisectrix directions because of the influence of the thermally excited electrons on the transport of the holes at the T-point.

	Trigonal	Binary	Bisectrix
n-type	115 Å	92 Å	97 Å
p-type	86 Å	48.4 Å	48.6 Å

same $Z_{1D}T$ values for $a < 50$ Å. This is because in the small wire size range, the quantum confinement is strong enough to separate the conduction subband and valence subband far apart so that the influence of electrons on hole transport becomes negligible. The binary and bisectrix directions become equivalent due to the cylindrical symmetry about the trigonal axis of the hole ellipsoid at the T-point. However, as the quantum wire size becomes larger than 50 Å, this symmetry is broken by the anisotropic contribution from the thermally excited L-point electrons to the hole transport. We therefore see that in Fig. 4-28 the difference in Z_{1D}T for p-type binary wires and bisectrix wires becomes distinguishable for $a > 50$ Å.

The Bi quantum wire sizes corresponding to the $Z_{1D}T = 1$ benchmark value for both n-type and p-type along the principal crystalline directions are listed in Table 4.3. We see that for both n-type and p-type Bi quantum wires, the trigonal direction is the most favorable, while the binary direction is the least favorable. Note that there is a small difference in the wire size for p-type Bi quantum wires along the binary and bisectrix directions because of the influence of thermally excited electrons at the L-point on the p-type transport due to the T-point holes.

The optimum carrier concentrations corresponding to the optimal chemical potential (or doping level) and to the maximum $Z_{1D}T$ are presented in Fig. 4-29 as a function of quantum wire thickness a at 300 K for both n-type (solid curve) and p-type (dashed curve) Bi nanowires along the three principal crystalline orientations, showing that the optimal chemical potential can be achieved with experimentally obtainable doping levels. Note that the carrier concentration for p-type quantum wires

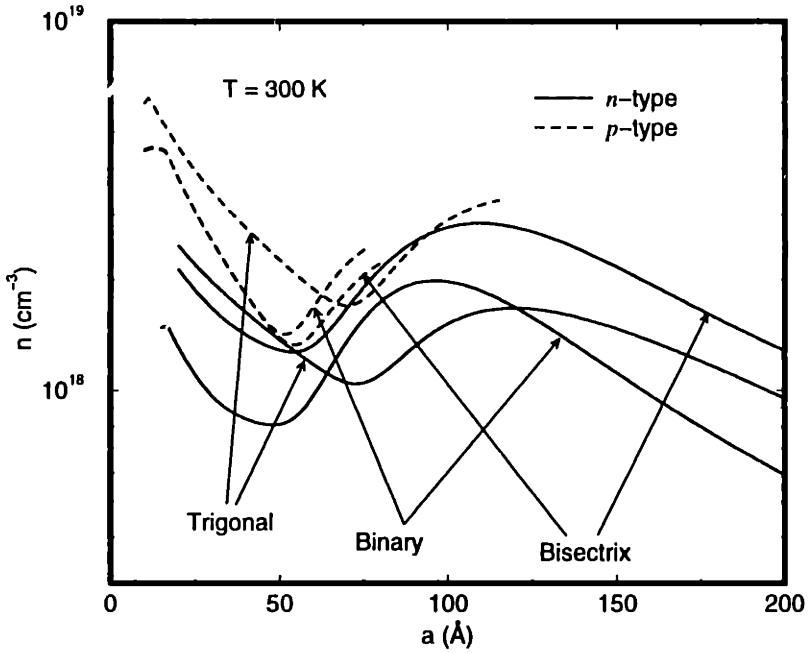

Figure 4-29: The optimum carrier concentrations corresponding to the optimal chemical potential as a function of quantum wire width, a, at 300 K for both n-type and p-type Bi nanowires oriented along the three principal crystalline directions.

oriented along the binary and bisectrix directions becomes different for wire sizes greater than 50 Å, reflecting the difference in optimum $Z_{1D}T$ for p-type wires along these two directions in this wire size range.

The optimal thermoelectric figure of merit as a function of temperature for both n-type and p-type Bi nanowires with a wire thickness $a = 100$ Å oriented along the three principal crystalline directions is shown in Fig. 4-30. For both n-type and p-type quantum wires, the trigonal orientation is the preferred direction except that for p-type wires, where the trigonal direction becomes slightly worse than the binary and bisectrix directions for temperatures below $\sim$100 K. For temperature between 175 K and 300 K, we see a difference in $Z_{1D}T$ for p-type binary wires and bisectrix wires, arising from the contribution of the electrons (minority carriers) to the hole transport. In Fig. 4-30, we also see abrupt transitions in $Z_{1D}T$ values, especially for n-type wires, around 110 K, below which the phonon mean free path is larger than the quantum wire size, so that an abrupt decrease in lattice thermal conductivity occurs at this temperature, according to the assumptions of our model.

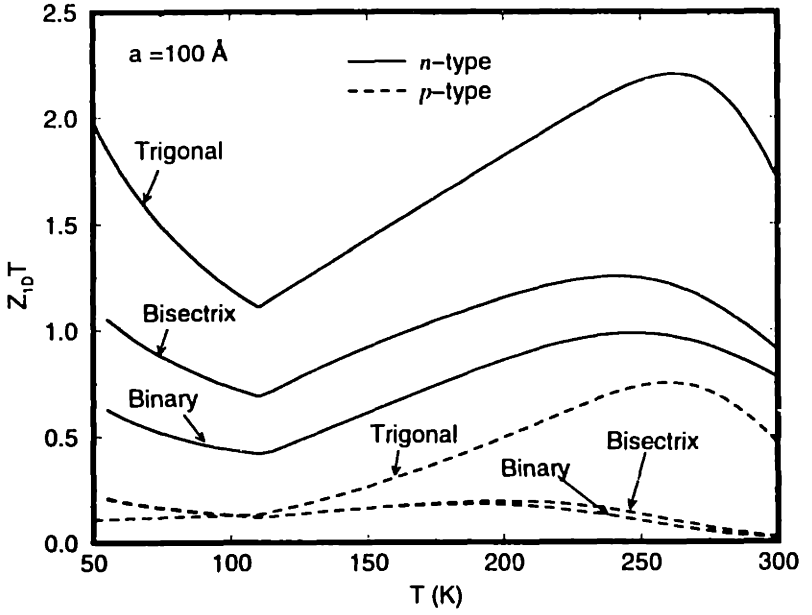

Figure 4-30: The optimal thermoelectric figure of merit as a function of temperature for both n-type and p-type Bi nanowires with wire thickness $a = 100$ Å oriented along the three principal crystalline directions.

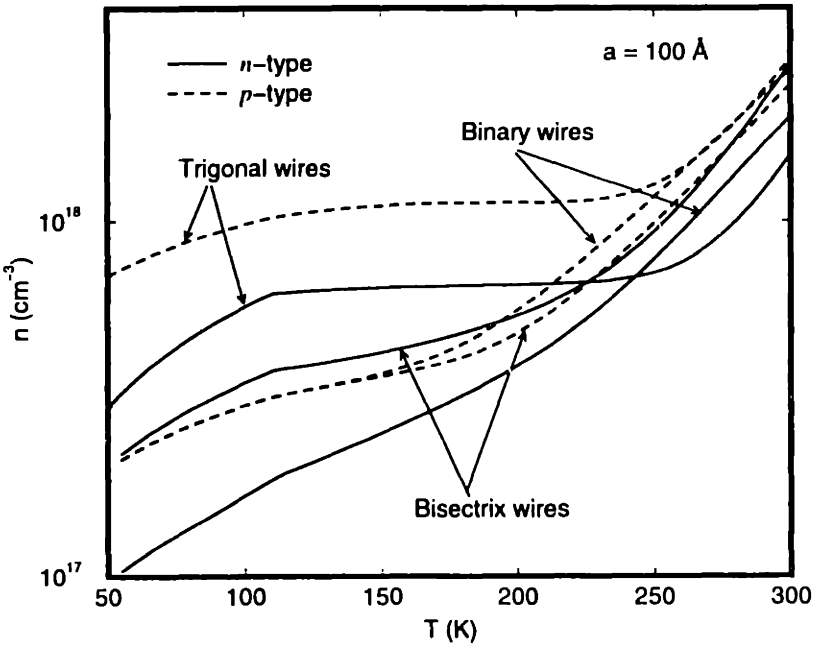

Figure 4-31: The optimum carrier concentrations corresponding to the optimal chemical potential as a function of temperature for both n-type and p-type Bi nanowires with wire size $a = 100$ Å oriented along the three principal crystalline directions.

The optimum carrier concentrations corresponding to the optimal chemical potential (or doping level) for maximum $Z_{1D}T$ are shown in Fig. 4-31 as a function of temperature for both n-type (solid curve) and p-type (dashed curve) Bi nanowires with a wire thickness $a = 100$ Å oriented along the three principal crystalline orientations, showing that the optimal chemical potential can be achieved with experimentally obtainable doping levels. Although a higher carrier concentration is needed at higher temperatures, it is easily compensated by thermal excitation.[14] Note that the carrier concentration for p-type quantum wires oriented along the binary and bisectrix directions becomes different for temperature between 175 K and 300 K, reflecting the difference in optimum $Z_{1D}T$ for these two directions in this temperature range.

In Fig. 4-30, we see that the optimal value of $Z_{1D}T$ is found around 250 K for both n-type and p-type Bi quantum wires oriented along the trigonal direction. For the other two crystalline directions, the optimal temperature is slightly lower. It is interesting to study how this optimal temperature changes with the size of the quantum wires. Figure 4-32 shows the optimal thermoelectric figure of merit as a function of temperature for both n-type and p-type Bi nanowires oriented along the trigonal direction for various wire thicknesses. We see that the optimal temperature for the optimum $Z_{1D}T$ increases as the quantum wire size decreases, approaching 300 K for a quantum wire size $a = 75$ Å. This is because as the quantum wire size decreases, the quantum confinement get stronger so that the effective band gap gets larger; therefore the system shows better thermoelectric performance at higher temperatures. For quantum wire sizes smaller than 75 Å, the optimum $Z_{1D}T$ would be higher than 300 K. This, however, still remains an open question, because values for all the physical properties of Bi on which my modeling is based come from characterizations of Bi below 300 K (see Section 4.5).

In this section, the temperature dependent study of the thermoelectric figure of merit of Bi quantum wires was developed, based on a basic non-parabolic band structure for bulk Bi and its temperature dependent band structure parameters. My

[14]For example, an intrinsic 100 Å trigonal wire has a carrier density of 2.87×10^{17} cm^{-3} at 300 K for both electrons and holes (see Appendix A).

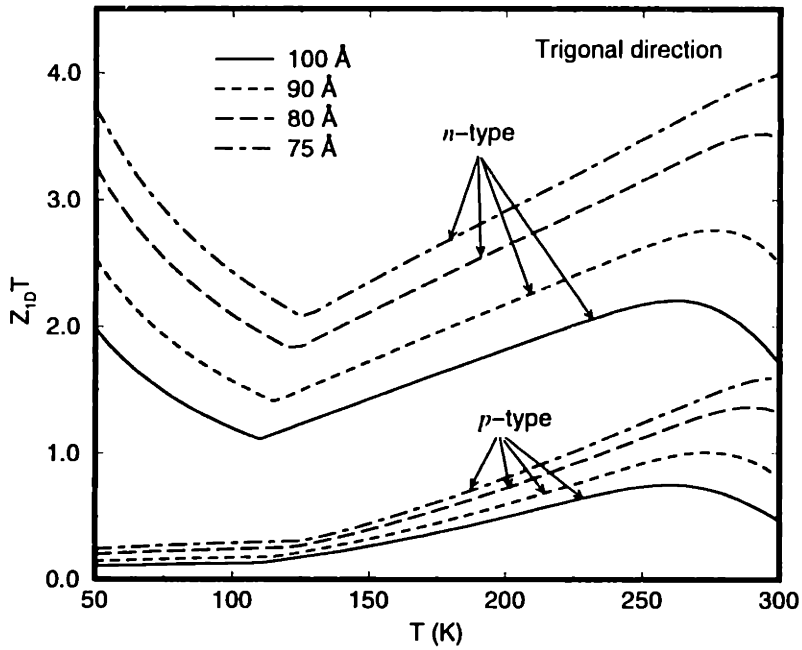

Figure 4-32: The optimal thermoelectric figure of merit as a function of temperature for both n-type and p-type Bi nanowires oriented along the trigonal direction for various wire thicknesses.

model calculations show that Bi nanowires, when appropriately doped, are potentially interesting for thermoelectric applications over a wide temperature range. However, the enhancement in $Z_{1D}T$ for p-type quantum wires is not as strong as for n-type wires. It is therefore demanding to design structures with high $Z_{1D}T$ values for p-type wires. Antimony (Sb) alloying provides a possible mechanism for this purpose and will be discussed in Chapter 6.

Chapter 5

Experimental Investigations

In the preceding chapters, I have shown the theoretical modeling of the thermoelectric figure of merit in the two-dimensional $Si/Si_{1-x}Ge_x$ superlattice system and in the one-dimensional Bi nanowire system. It is expected that significant enhancement of the thermoelectric figure of merit over bulk values can be achieved in low-dimensional systems. In this chapter, I present some experimental investigations on low-dimensional thermoelectricity in $Si/Si_{1-x}Ge_x$ and bismuth nanowire systems.

5.1 Thermoelectric transport measurement system

A thermoelectric transport measurement system working in the temperature range from 4 K to 300 K has been designed and constructed in order to characterize the thermoelectric transport properties of thin film or superlattice samples. This system is designed to enable the characterization of the electrical conductivity σ and the Seebeck coefficient S on the same sample in the same orientation, so that the power factor $S^2\sigma$ can be reliably characterized on the same piece of sample with transport along the same direction.

The experimental setup is shown in Fig. 5-1. This setup consists of a cryogenic dewar from Janis Research Co., Inc. (Model No. 10DT) to provide the cryogenic environment for the transport measurements. It can operate between 4 K and 300 K using cryogenic agents such as liquid nitrogen and liquid helium. The sample space

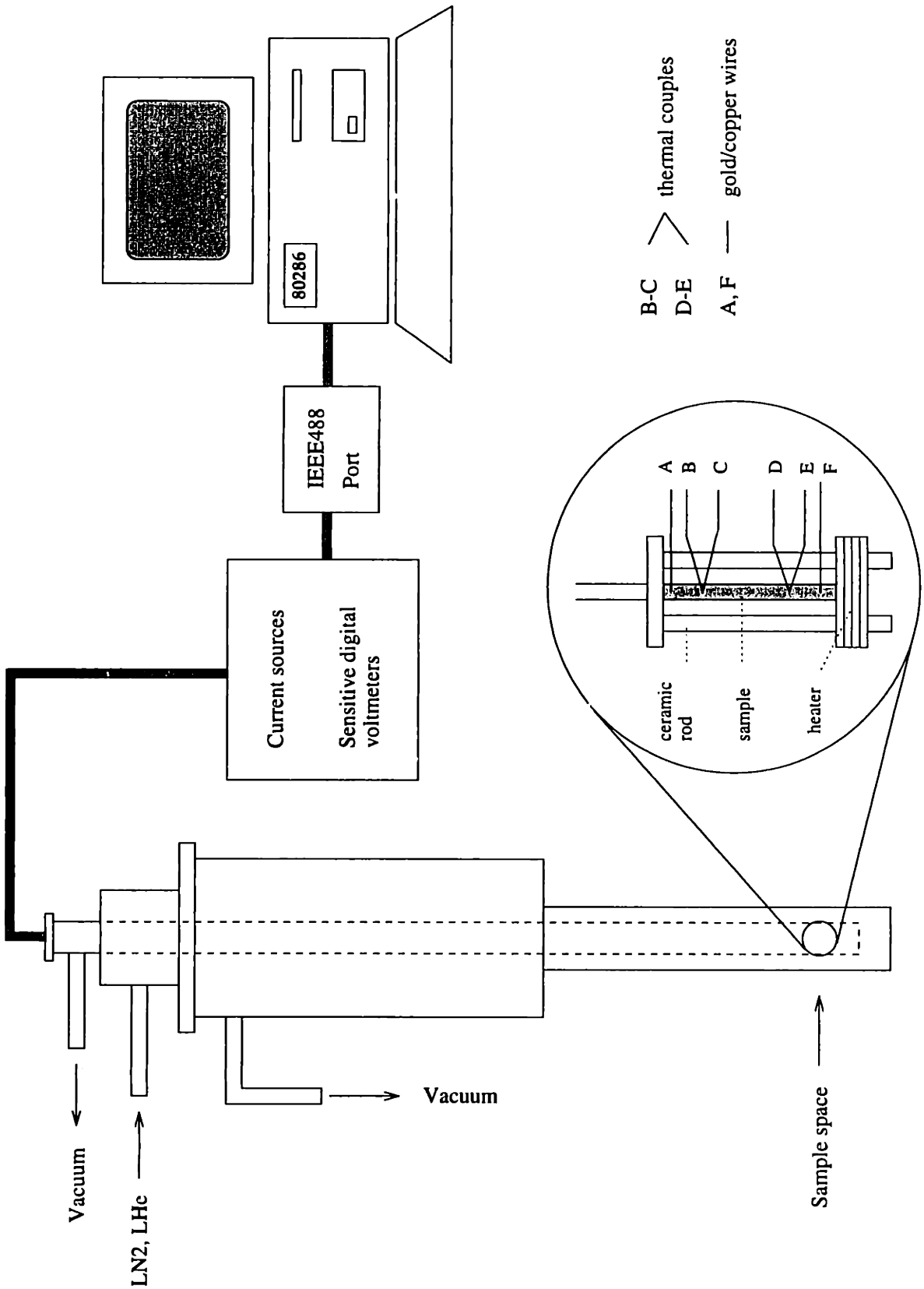

Figure 5-1: The thermoelectric transport measurement system.

can be pumped to high vacuum (up to 10^{-6} Torr) to eliminate systematic errors, such as convection and a false determination of temperature gradient, while measuring the Seebeck coefficient.

The probe tip is shown enlarged in Fig. 5-1. To provide a good thermal background, the probe tip is made of copper. The tip itself also functions as a heat sink. A sample heater is made of a copper block with 50 Ω twisted pair[1] LakeShore MW-36 Manganin Wire coiled tightly around it. The sample heater is supported by two low thermal conductivity ceramic rods, and the heater can be moved along the ceramic rods to fit the different sizes of the samples.

The sample is inserted between the heater and the heat sink, and is attached using electrically insulating but thermally conductive epoxy suited for different kinds of samples. The probe tip can accommodate a rectangular sample with maximum dimensions of 4×15 mm^2. Four ohmic contacts are made on the sample for the measurements. Wires A and F are gold or copper wires used to carry the electrical current for conductivity measurements. The wire pair B and C is a thermocouple: B is a 0.003″ chromel wire and C is a 0.005″ AuFe(0.07%) alloy wire. Wires D (chromel) and E (AuFe(0.07%)) constitute a second chromel-AuFe(0.07%) thermocouple. All wires are attached to the sample with indium, which results in excellent ohmic contacts as well as excellent thermal contacts with the thermocouple junctions. The other ends of the wires are connected to the base of the probe head to provide a common temperature reference. Care was taken to ensure that the wires attached to the base are in good thermal contact but make no electrical contact. The wires are then connected to the top of the probe by 36 AWG cryogenic wires, and then connected to a post plate using a copper cable. The post plate is then connected to the measuring devices, such as current sources and sensitive digital voltmeters. All the measuring devices are connected through an IEEE-488 port to a Personal Computer which is used for automatic data acquisition.

A LakeShore DT-471-SD silicon diode temperature sensor is attached to the base

[1]The use of a twisted pair wire eliminates the influence of the magnetic field that would otherwise be created by the heater current.

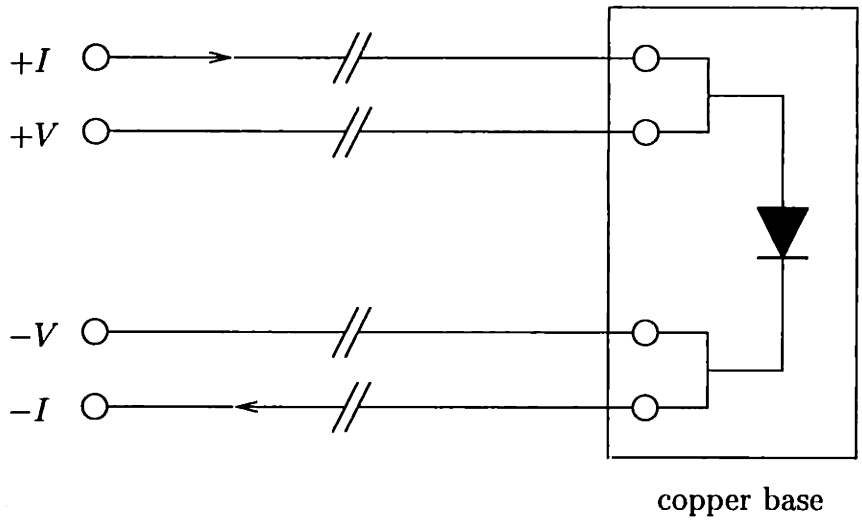

Figure 5-2: The wiring of the silicon diode temperature sensor.

of the probe tip to measure the temperature of the copper base reference. The wiring of the diode is shown in Fig. 5-2 to ensure precise measurement of the diode voltage.[2] This silicon diode temperature sensor is also used with a LakeShore DRC-93CA temperature controller.

A copper cylinder outside the probe tip is employed to protect the sample, the wiring and the heater during the measurement. A 50 Ω twisted pair of 36 AWG Manganin Wire is coiled tightly around the copper cylinder, which is used by the LakeShore DRC-93CA temperature controller as a system heater.

Electrical conductivity measurements employ the four-probe technique. With the sample heater off, a DC current is passed through wires A and F and the voltage is measured using gold or copper wires C and E. The potential drop was measured for both forward and reverse currents to eliminate any thermoelectric effects.

For Seebeck coefficient measurements, the sample heater is used to apply a temperature difference of several degrees to the sample, and the specimen enclosure is evacuated to minimize heat loss and air convection. The two thermocouples are used to measure both the temperature difference ΔT between the two junctions on the sample, and the resulting Seebeck voltage ΔV (across C and E) between the junc-

[2]This is to avoid including the voltage drop across the wires between the copper base and the voltmeter in the voltmeter reading, although the sensor current is only 10 μA.

tions. The temperature difference is varied, the corresponding Seebeck voltage is measured, and the Seebeck coefficient is found from the slope of the line (after subtracting the contribution of the AuFe(0.07%) wire). In each ΔV-ΔT measurement, there is a small non-zero offset in ΔV at $\Delta T = 0$. This offset together with the linearity of ΔV-ΔT data indicates the quality and reliability of the measurement.

After finding the electrical conductivity and the Seebeck coefficient of the same piece of sample, the measurement of the thermoelectric power factor $S^2\sigma$ is completed.

5.2 The PbTe/$Pb_{1-x}Eu_xTe$ multiple quantum well superlattices

After the thermoelectric transport measurement system was constructed, I first used it to characterize the thermoelectric power factor of PbTe/$Pb_{1-x}Eu_xTe$ multiple quantum well (MQW) superlattice samples. The PbTe/$Pb_{1-x}Eu_xTe$ MQW superlattices was the first system used to test the two-dimensional thermoelectric transport theory [9].

Samples of PbTe/$Pb_{1-x}Eu_xTe$ MQW superlattices were grown by Dr. Harman of M.I.T. Lincoln Laboratory using molecular beam epitaxy (MBE) in a modified Varian 360 MBE system. Details of the sample preparation and characterization are given elsewhere [54]. Briefly, first a $Pb_{0.958}Eu_{0.042}Te$ buffer of about 2000 Å was deposited on a freshly cleaved BaF_2(111) substrate to ensure complete strain relaxation and high structural perfection of the layer. Next, samples with periods of 100 to 150 PbTe/$Pb_{0.927}Eu_{0.073}Te$ MQW structures were grown, with PbTe well widths varying between 17 Å and 55 Å, separated by $Pb_{0.927}Eu_{0.073}Te$ barriers of about 450 Å. Each layer was a single crystal with the (111) plane parallel to the layers. The carrier density was varied by using Bi donor atoms in the barrier material. This resulted in an n-type material so that all the electrical conduction is in the conduction band quantum well.

Since the PbTe/$Pb_{1-x}Eu_xTe$ MQW superlattice samples were grown on BaF_2

substrates, which is a good insulator, both electrically and thermally, it was very easy to establish a suitable temperature gradient across the samples. To attach a sample between the sample heater and the heat sink, I used GE 7031 Varnish as an epoxy to provide good thermal contacts between the sample and the copper surface of the sample heater and heat sink, while providing good electrical insulation at the same time.

The electrical conductivity and the Seebeck coefficient of PbTe/$Pb_{1-x}Eu_xTe$ MQW superlattice samples were measured at room temperature, and the results were calibrated at the M.I.T. Lincoln Laboratory with a commercial system by MMR Technologies, which uses a comparison technique to measure the Seebeck coefficient. The agreement was excellent.

I have performed room temperature measurements as well as temperature dependent measurements of the thermoelectric power factor on a series of PbTe/$Pb_{1-x}Eu_xTe$ MQW superlattice samples, and the detailed results were described in Chapter 7 of Ref. [8].

5.3 The $Si/Si_{1-x}Ge_x$ superlattice samples

In Chapter 3, I predicted an enhancement of the thermoelectric figure of merit in the $Si/Si_{1-x}Ge_x$ superlattice system. In this section, I present an experimental investigation of the thermoelectric transport properties of $Si/Si_{1-x}Ge_x$ superlattices, basically confirming these predictions.

Based on my calculations, I designed the $Si/Si_{1-x}Ge_x$ superlattice structures and the samples were grown by Prof. K. L. Wang of the University of California at Los Angeles (UCLA) using a solid phase Perkin Elmer 430S molecular beam epitaxy (MBE) system.

All the $Si/Si_{1-x}Ge_x$ superlattice samples were grown on Si wafers. These substrates introduced a difficulty into the Seebeck coefficient measurements. Because Si has a very high thermal conductivity, it is very difficult to establish a significant temperature gradient across the sample, especially at cryogenic temperatures. In this

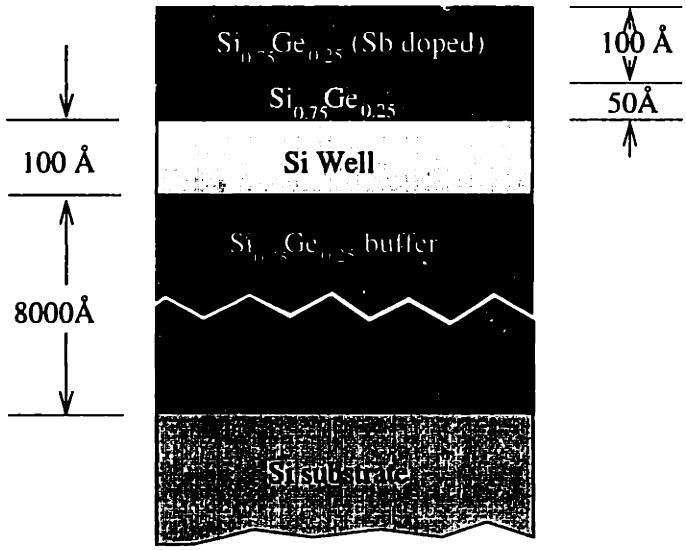

Figure 5-3: A single quantum well sample.

case, the thermal contacts between the sample and the copper surface of the sample heater and the heat sink become crucial, and GE 7031 Varnish, which worked quite well with PbTe/$Pb_{1-x}Eu_xTe$ MQW superlattice samples grown on BaF_2 substrate, does not provide good enough thermal contacts, especially at cryogenic temperatures. In order to improve the quality of the thermal contacts, I employed a high thermal conductivity epoxy EPO-TEK H70E from Epoxy Technology, which provided excellent thermal, but electrically insulating, contacts.

In order to make good ohmic contacts on n-type $Si/Si_{1-x}Ge_x$ superlattice samples, indium with 5 at% antimony alloy was used as the contact agent, and the contacts were annealed at 350 °C for 1-3 minutes.[3]

5.3.1 The early experiments

In order to measure the quantum confinement effect on the thermoelectric transport properties unambiguously, I started the experimental investigation with single layer Si quantum well samples. Figure 5-3 shows a typical structure of this type of sample.

[3]The annealing time depends on the thickness of the film. An empirical rate at this temperature is about 1000 Å per minute [55].

The sample was grown in the MBE chamber in a process as follows. A protective oxide resulting from the chemical cleaning was removed by an anneal at 900 °C for 10 minutes. A 3000 Å Si buffer layer was first grown, followed by a 4500 Å to 5000 Å $Si_{0.7}Ge_{0.3}$ layer which formed the substrate. The thickness and Ge fraction of this layer ensure nearly complete relaxation of the film used for the thermoelectricity experiments. On this substrate, a 100 Å Si quantum well was then grown, followed by a 50 Å $Si_{0.7}Ge_{0.3}$ spacer layer and a 100 Å to 200 Å $Si_{0.7}Ge_{0.3}$ Sb doped carrier supply layer. The substrate temperature was held at 600 °C except for the growth of the carrier supply layer, where the substrate temperature was reduced to 350 °C because of the reduced sticking coefficient of Sb at higher temperatures. Subsequent to the growth of the cap layer, the wafer was ramped to 600 °C for improving the film quality.

The transport measurement of a typical sample is described as follows. Hall measurements were performed at 300 K and 77 K, showing that the sample has mobilities of $\sim 700\,cm^2\,V^{-1}\,s^{-1}$ and $\sim 4000\,cm^2\,V^{-1}\,s^{-1}$ and carrier densities of $\sim 4\times10^{18}\,cm^{-3}$ and $\sim 2\times10^{18}\,cm^{-3}$, at 300 K and 77 K, respectively. The resistivity (Fig. 5-4) and Seebeck coefficient (Fig. 5-5) of the sample were measured from 77 K to 300 K. The power factor $S^2\sigma$ was determined from the resistivity and Seebeck measurements as a function of temperature, as shown in Fig. 5-6.

The results show that the power factor at room temperature is greatly enhanced compared to the bulk Si (by about one order of magnitude). Applying Eq. (3.20) with $l = 100$ Å for the thermal conductivity, we get a room temperature figure of merit of $Z_{2D}T \approx 0.12$, which is one order of magnitude higher than the figure of merit for bulk Si. Notice that this is a conservative estimate because the phonon scattering due to the surface roughness and imperfections gives rise to diffuse scattering which is expected to reduce the thermal conductivity significantly (see discussion in Section 3.4). The reduction of the thermal conductivity in a 2D system, part of which has been accounted by Eq. (3.20), can further increase the figure of merit to a useful value. In fact, a giant reduction by almost two orders of magnitude in the thermal conductivity has been reported for a Si membrane with only a decrease by a factor of two in the

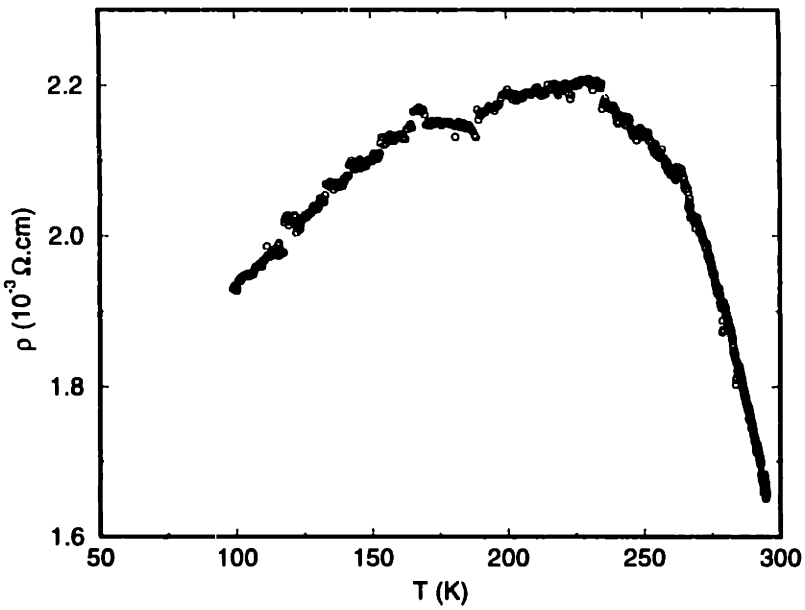

Figure 5-4: The experimental temperature dependence of the electrical resistivity ρ for a Si quantum well with $a = 100\,\text{Å}$ grown on a $Si_{0.7}Ge_{0.3}$ buffer layer.

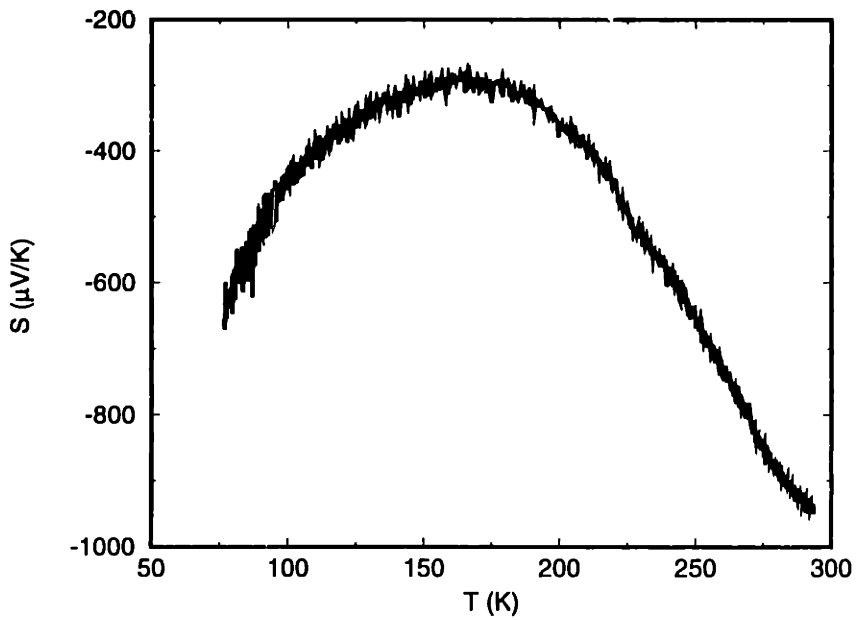

Figure 5-5: The experimental temperature dependence of the Seebeck coefficient S for a Si quantum well with $a = 100\,\text{Å}$ grown on a $Si_{0.7}Ge_{0.3}$ buffer layer.

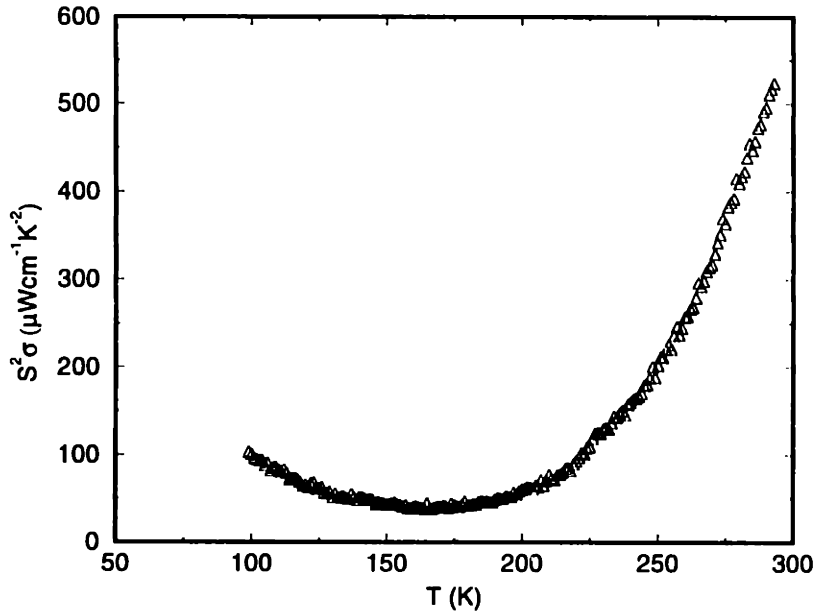

Figure 5-6: The experimental temperature dependence of the power factor ($S^2\sigma$) for a Si quantum well with $a = 100$ Å grown on a $Si_{0.7}Ge_{0.3}$ buffer layer.

carrier mobility [56]. Thus, further detailed work on the $Si/Si_{1-x}Ge_x$ system should address the optimization of ZT rather than of $S^2\sigma$.

Since $Si/Si_{1-x}Ge_x$ is a system aimed at high temperature operation (up to 1000 K), it would be interesting to look at the thermoelectric performance of $Si_{1-x}Ge_x$ quantum well systems at high temperatures. Since the power factor in Fig. 5-6 increases rapidly with increasing T above room temperature, the power factor as well as the thermoelectric figure of merit for the quantum well are expected to show even greater enhancement above room temperature, consistent with the high values of the figure of merit for bulk silicon-germanium alloys at elevated temperatures [25, 26].

5.3.2 Elimination of the influence from the Si substrate and $Si_{1-x}Ge_x$ buffer layer on the Seebeck measurements

Although a giant enhancement of the thermoelectric power factor of a single Si quantum well at room temperature over its bulk value has been observed (see Section 5.3.1), it is important to point out that Si with a low electrical conductivity has

a very high Seebeck coefficient. It is therefore expected that the Si substrate as well as the buffer layer, which is essential to get the relaxed type-II superlattice, might contribute to the transport measurements, especially to the Seebeck coefficient measurement. Therefore, it is necessary to eliminate the contributions of the substrate and buffer layer to the measured transport coefficients, in order to make more reliable measurements on superlattice samples.

To eliminate the substrate contribution, I proposed to make use of Silicon-on-Insulator (SOI) substrates, which use a 2000 Å to 3600 Å SiO_2 layer to electrically isolate the 510 μm to 540 μm thick Si substrate from the superlattice structure grown on top of the wafer. In this way, the contributions to the electrical conductivity measurement and the Seebeck coefficient measurement from the bulky Si substrate can be successfully eliminated.

However, on top of the SiO_2 layer, there is a buffer layer which is usually a few thousand angstroms of $Si_{1-x}Ge_x$. The contribution to the electrical conductivity from this buffer layer can be neglected because the electrical conductivity of this layer is a few orders of magnitude lower than that in the Si quantum wells. The measured Seebeck coefficient, however, is a weighted average of the Seebeck coefficient for all the components that contribute to the transport

$$S_{\text{measured}} = \frac{\sum_i R_i^{-1} S_i}{\sum_i R_i^{-1}}, \tag{5.1}$$

where R_i and S_i are the resistance and the Seebeck coefficient of the i^{th} component, respectively. Although the resistance of the buffer layer is much lower than that of the Si quantum well, the Seebeck coefficient of the buffer layer is higher [22], resulting in the product $R^{-1}S$ of the buffer layer being comparable[4] to the corresponding value for a quantum well.

In order to characterize the contributions to the Seebeck coefficient measurements from the buffer layer, I initiated an extrapolative approach. Suppose the superlattice

[4]It turned out experimentally that the $R^{-1}S$ values are only comparable for the buffer and the quantum well within an order of magnitude, and $R^{-1}S$ for the buffer layer is actually smaller than the value in the quantum well.

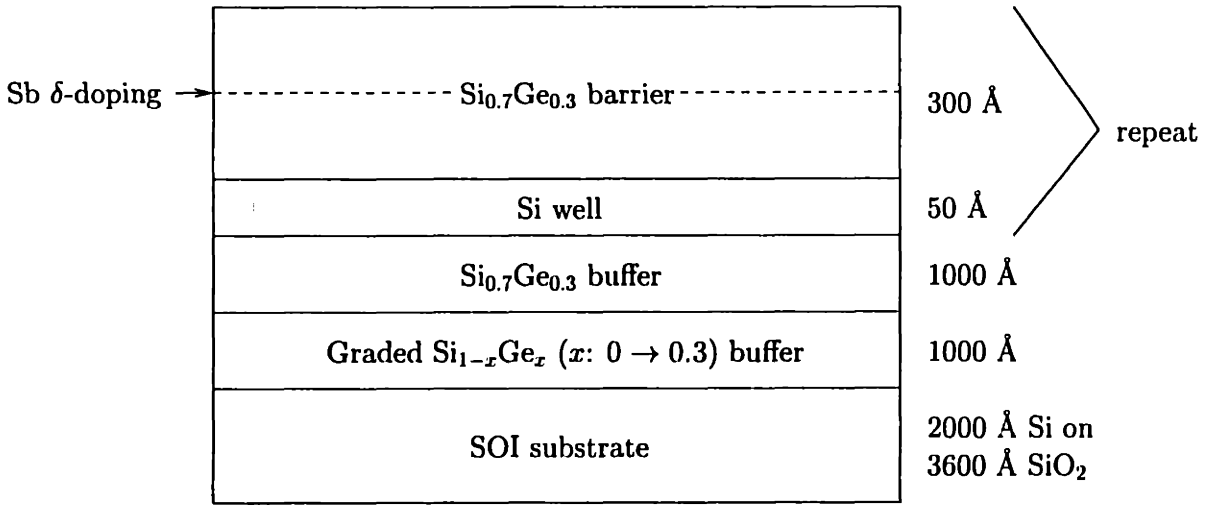

Figure 5-7: The structure of a set of three samples. Each period consists of a Si well and a $Si_{0.7}Ge_{0.3}$ barrier and is 350 Å wide. The three samples have 5, 10 and 15 periods, respectively.

consists of a buffer layer and n periods of quantum well and barrier layer all in parallel, according to Eq. (5.1), the measured Seebeck coefficient is then

$$S_n = \frac{R_b^{-1} S_b + n R_w^{-1} S_w}{R_b^{-1} + n R_w^{-1}}, \tag{5.2}$$

which leads to

$$S_n = S_w + \frac{R_w S_b}{R_b}\left(\frac{1}{n}\right) \tag{5.3}$$

when

$$R_b \gg \frac{R_w}{n} \qquad \text{or} \qquad R_b^{-1} \ll n R_w^{-1}, \tag{5.4}$$

where S_n is the measured Seebeck coefficient for a sample with n periods, S_w and S_b are the Seebeck coefficients for the quantum well and buffer regions, respectively, and R_w and R_b are resistances for the quantum well and buffer regions, respectively. Though R_b is very large compared to R_w, S_b is also very large due to the low carrier density in the buffer layer. Therefore, the contribution of the second term on the right hand side of Eq. (5.3) could be noticeable.

In Eq. (5.3), we see that the measured Seebeck coefficient is a linear function of

Table 5.1: Hall measurements of samples shown in Fig. 5-7 at room temperature.

# of periods in sample	5	10	15
Mobility (cm^2/Vs)	405.5	689.1	640.8
Sheet carrier density (cm^{-2})	2.5×10^{13}	5.17×10^{13}	1.04×10^{14}
Sheet carrier density per period (cm^{-2})	5.0×10^{12}	5.17×10^{12}	6.9×10^{12}

$1/n$, where n is the number of periods in the sample. Therefore, by measuring a set of samples with different numbers of periods, a linear regression can be performed on the S_n versus $1/n$ data pairs, and the Seebeck coefficient for the quantum well is obtained by extrapolating S_n in the limit of $1/n \rightarrow 0$, or $n \rightarrow \infty$.

To test this extrapolative approach, a series of samples with the same structure, but with different numbers of periods, were grown. Three similar superlattice samples with 5 periods, 10 periods and 15 periods, respectively, were fabricated. Their structures are schematically shown in Fig. 5-7.

These three samples were grown continuously, one after the other, using the solid source MBE system. Firstly, SOI wafers with 2000 Å Si on top of 3600 Å SiO_2 were used as substrates. After a standard Shiraki cleaning procedure, the substrates were immediately introduced into the MBE chamber. The protective oxide layer was removed by subsequently heating the substrates at 930 °C for 15 minutes. The growth temperature was kept at 550 °C except that the δn doping layers (Sb) were grown at 350 °C. The growth rate for Si and Ge was monitored and controlled by a Sentinel III Deposition controller. With these conditions, 1000 Å of an undoped $Si_{1-x}Ge_x$ layer with x varying from 0 to 0.3 was grown first, on top of which a 1000 Å layer of $Si_{0.7}Ge_{0.3}$ was grown, yielding a buffer layer with an overall thickness of 2000 Å. The Si quantum wells and $Si_{1-x}Ge_x$ barriers were then grown on top of the buffer layer, with the number of periods being 5, 10, and 15. An antimony δ-doping layer was placed in the middle of each $Si_{1-x}Ge_x$ barrier layer to provide electrons for the Si quantum wells. The final layer of the film is the last $Si_{1-x}Ge_x$ barrier layer.

The Hall measurements were performed on these samples using a Van der Pauw technique and the results are shown in Table 5.1. The results show that these sam-

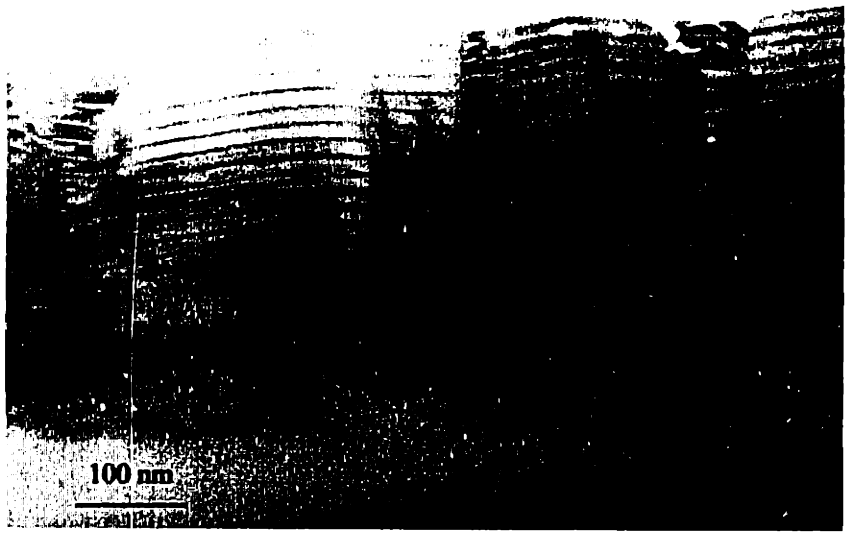

Figure 5-8: The TEM micrograph of the $Si/Si_{1-x}Ge_x$ superlattice sample with 15 periods. The quantum well thickness is 50 Å.

ples have a very similar sheet carrier density per period, which is essential to validate Eq. (5.3).[5] The mobility for the samples with 10 periods and 15 periods has similar values, but the mobility for the sample with 5 periods is about 40% lower. Transmission electron microscopy (TEM) shows that these samples have a large density of defects, as shown in Fig. 5-8, especially in the region closer to the buffer layer. Therefore, the 5 period sample has relatively more defect scattering compared to the other two samples. The TEM study also showed that there should be plenty of room for improvement of the interface quality.

The Seebeck coefficients for the set of samples were measured with high precision at room temperature, as shown in Fig. 5-9. Least mean squared linear regressions were performed on the ΔV-ΔT data to get the slopes for the Seebeck coefficients. The correlation coefficient γ shows a strong linearity in the data and a high precision of the fits. The small offsets in the measurements suggest that we have achieved high quality electrical and thermal contacts in our measurements.

[5]In Eq. (3.11), we see that the Seebeck coefficient is only determined by the chemical potential ζ^*, which determines the carrier density in the system, and S does not depend on the carrier mobility.

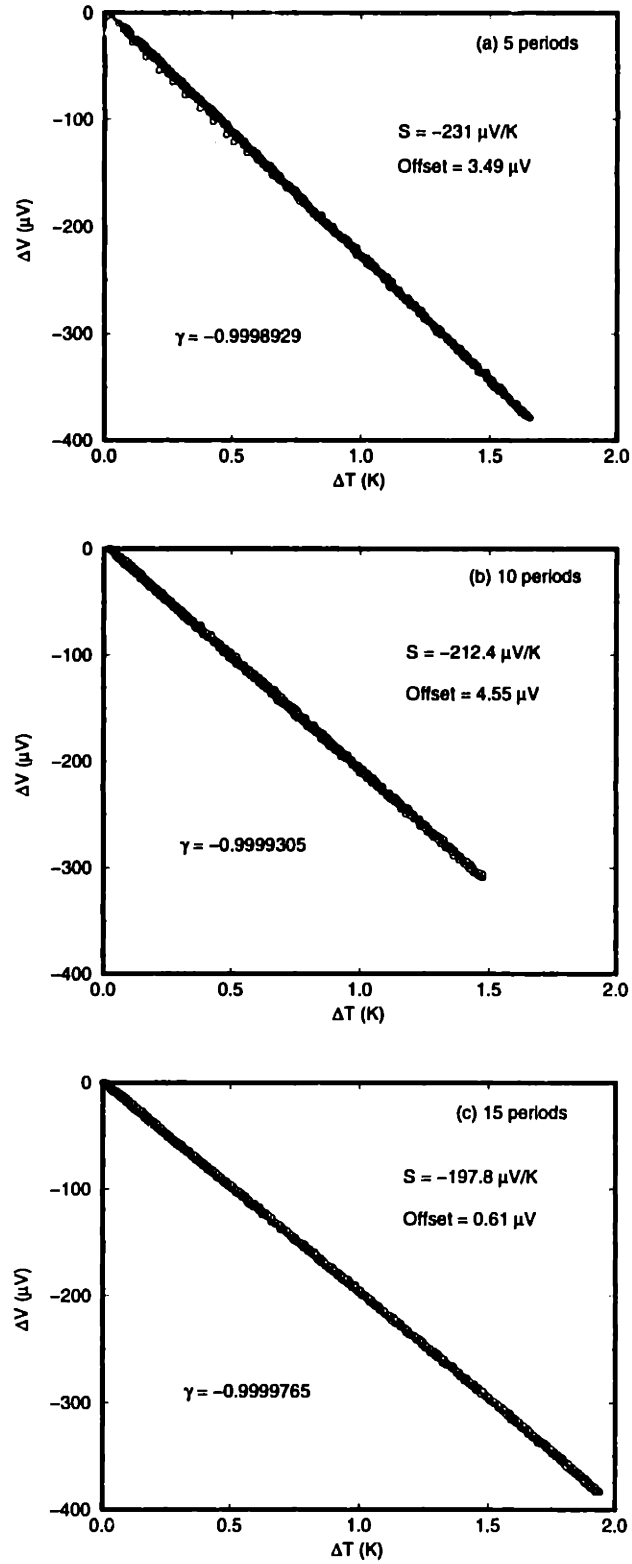

Figure 5-9: The Seebeck coefficients for the set of samples with structures shown in Fig. 5-7 are measured with high precision at room temperature. The correlation coefficient γ shows a strong linearity in the data and high precision of the fits.

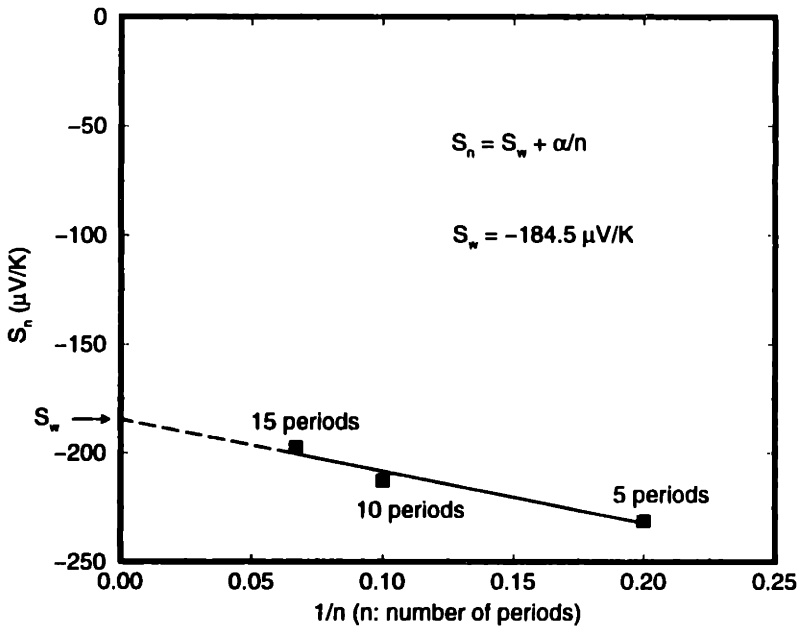

Figure 5-10: The measured Seebeck coefficient at room temperature as a function of $1/n$, where n is the number of periods in each sample. The Seebeck coefficient for the quantum well S_w is extrapolated to the limit $1/n \to 0$, or $n \to \infty$.

Figure 5-10 plots the room temperature Seebeck coefficient for these samples from Fig. 5-9 against the inverse of the number of periods, $1/n$. A linear extrapolation is performed for $1/n \to 0$ to get the Seebeck coefficient for the quantum well as $S_w = -184.5\,\mu\text{V/K}$, with the contribution from the buffer layer eliminated. Comparing this Seebeck coefficient value with that of the sample with 15 periods ($S_{n=15} = -197.8\,\mu\text{V/K}$), we see that the contribution to the Seebeck coefficient from the buffer layer is less than 10%. This suggests us that, in order to minimize the burden[6] on the sample growth, we can grow samples with a number of periods greater than or equal to 15 using SOI substrates, and the error introduced by neglecting the effect of the buffer layer is less than 10%. As we move in the direction of smaller quantum well widths, we expect that the contribution from the buffer layer will be less significant, because smaller quantum well widths are expected to yield a higher power factor.

[6]Because the Sb layers are grown at a lower temperature, temperature cycling in ultra-high vacuum is needed for each period of growth. This results in a growth time of about one hour for each period.

The power factor ($S^2\sigma$) at room temperature for this set of samples is found to be $45\,\mu W/cmK^2$, resulting in a two-dimensional thermoeletric figure of merit at 300 K of value 0.14, using the calculated value for the thermal conductivity, 9.64 W/mK, from our model as described above. Although this is a significant enhancement over the Si bulk value [12], we expect better performance if better carrier mobility (see Table 5.1) can be achieved by improving the interface quality.

5.3.3 $Si/Si_{1-x}Ge_x$ superlattice samples with smaller quantum well widths

As discussed above, in order to minimize the burden on the sample growth, we can grow samples with a number of periods greater than or equal to 15 using SOI substrates.

In this section, I present the experimental study of a set of superlattice samples with quantum well widths of 40 Å, 30 Å, 20 Å, and 10 Å. Each sample contains 15 periods of quantum wells and quantum barriers. The design of these samples is the same as that shown in Fig. 5-7 except that the buffer layer has a slightly different structure. The 2000 Å undoped $Si_{1-x}Ge_x$ graded buffer layers were grown on top of the SOI substrates, which consist of 500 Å Si, 500 Å $Si_{0.9}Ge_{0.1}$, 500 Å $Si_{0.8}Ge_{0.2}$, and 500 Å $Si_{0.7}Ge_{0.3}$. This structural modification was introduced in an attempt to improve the interface quality of the samples.

Figure 5-11 shows a TEM micrograph for the sample with a quantum well width of 30 Å. It is shown that the interface quality of this set of samples is largely improved compared to the previous set of samples (see Fig. 5-8). Note that a wavy in-plane feature has developed, which arises from the relaxation growth of the $Si_{1-x}Ge_x$ buffer layer. This wavy feature reduces the actual layer thickness relative the nominal layer thickness. The measured thickness of a period for this sample is 230 Å [57], a 30% reduction from its nominal thickness (330 Å).

The experimental characterizations of these samples at room temperature are shown in Table 5.2. The sheet carrier density and the carrier mobility were measured

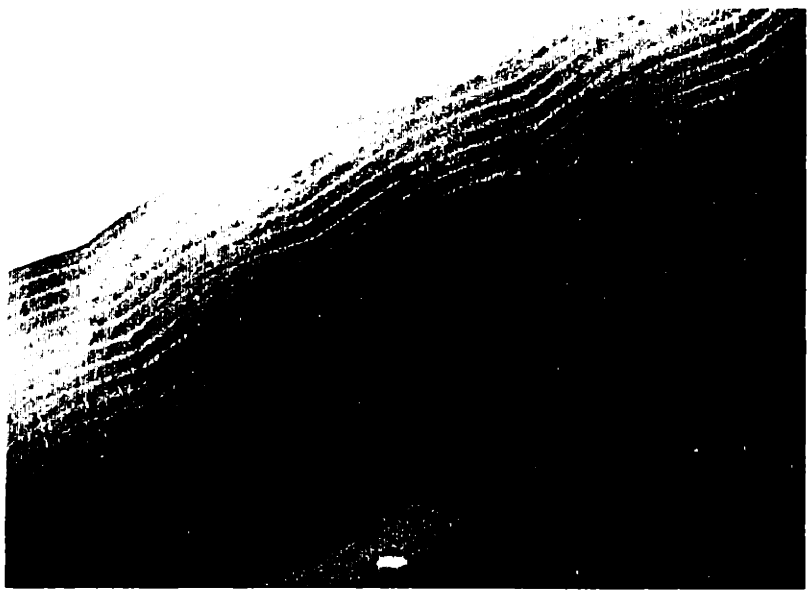

Figure 5-11: The TEM micrograph of the $Si/Si_{1-x}Ge_x$ superlattice sample with 15 periods. The quantum well thickness is 30 Å. The scale bar reads 100 nm.

by the Hall technique using the Van der Pauw configuration. If we assume that all the carriers are confined within the Si quantum wells, we will get a large enhancement of the thermoelectric power factor inside the Si quantum well as shown in the 9^{th} row of Table 5.2 where $S^2\sigma$ data are listed. However, for the strained type-II $Si/Si_{1-x}Ge_x$ superlattice structures, the conduction band offset between the Si quantum well layer and the $Si_{1-x}Ge_x$ quantum barrier layer is very small ($\sim$100 meV). As described in Section 3.7, for this kind of geometry, a large portion (about 30% to 50%) of the electron wave function leaks into the barrier regions. Therefore, for a more reliable estimation,[7] I calculated the transport quantities assuming that all the layers, including both the Si quantum well layers and the $Si_{1-x}Ge_x$ quantum barrier layers, are participating in the thermoelectric transport, as shown by the rows marked with the * sign in Table 5.2. In this case, all the samples have similar values for the thermoelectric power factor $S^2\sigma$, as shown in the 10^{th} row in Table 5.2. However, we observe that the mobility of the samples decreases significantly as the quantum well width

[7]This is also the most conservative estimation, which is very important for thermoelectric device evaluation.

Table 5.2: The characterization of $Si/Si_{0.7}Ge_{0.3}$ quantum well superlattice samples with various quantum well widths at room temperature.

Well Width (Å)	40	30	30	10
# of periods	15	15	15	15
Sheet carrier density ($10^{13}\,cm^{-2}$)	6.2	7.5	9.5	19
Volume carrier density ($10^{19}\,cm^{-3}$)*	1.8	2.3	3.0	6.1
Mobility (cm^2/Vs)	535	488	312	105
σ ($\Omega^{-1}cm^{-1}$)	833	1081	1418	1892
σ ($\Omega^{-1}cm^{-1}$)*	98.0	98.3	88.6	61.0
S ($\mu V/K$)	-297.5	-285.1	-312.9	-326.0
$S^2\sigma$ ($\mu Wcm^{-1}K^{-2}$)	73.7	87.9	138.9	201.0
$S^2\sigma$ ($\mu Wcm^{-1}K^{-2}$)*	8.7	8.0	8.7	6.5
S^2n ($10^{23}\,\mu V^2cm^{-3}K^{-2}$)*	15.9	18.7	29.4	64.8

* These quantities are obtained assuming that the barrier layers are part of the transport media. This is the most conservative estimation.

decreases, revealing that the interface scattering becomes a problem which limits the electronic carrier mobility.

It is believed that there are two physical factors that influence the thermoelectric transport of the system. The first factor is the quantum confinement induced enhancement of the density of states, which is the central topic that is discussed in this thesis. The second factor is the potential enhancement in the carrier mobility arising from the modulation doping, which is essentially a material science problem. To isolate these two physical aspects in this problem, I calculated the quantity S^2n, where n is the carrier concentration. This quantity is indeed the power factor $S^2\sigma$ apart from a factor that is proportional to the carrier mobility ($\sigma = ne\mu$). The experimental values including all the contribution from the buffer layers to S^2n are shown in the last row of Table 5.2. We see that a consistent enhancement of this quantity as the quantum well size decreases is demonstrated, and this enhancement solely arises from the effect of quantum confinement.

To make a comparison between my theoretical modeling and the experimental data, I calculated the maximum S^2n as a function of quantum well width a at room temperature for $Si/Si_{1-x}Ge_x$ superlattice structures based on the theoretical model

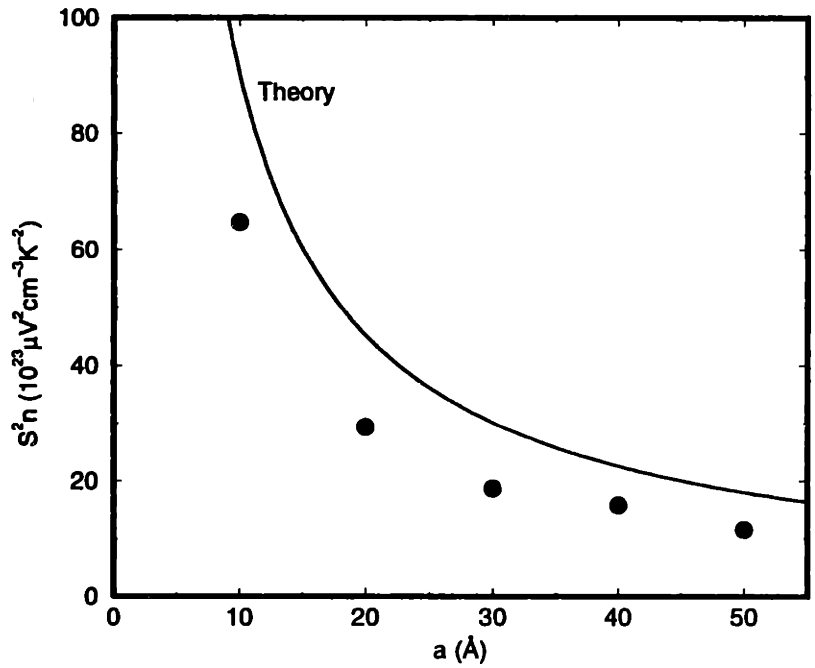

Figure 5-12: The comparison between experimental data for S^2n and the theoretical curve at optimal doping level for optimum thermoelectric figure of merit for $Si/Si_{0.7}Ge_{0.3}$ quantum well superlattice system at room temperature.

discussed in Section 3.4, and the comparison is shown in Fig. 5-12. Also shown in the figure are the experimental points listed in Table 5.2 and the 15-period sample that was studied in Section 5.3.2. We see that there is a systematic discrepancy between the theoretical modeling and the experimental data. There are three reasons for this discrepancy. Firstly, the samples are all structure with 15 periods. As demonstrated in Section 5.3.2, the measured Seebeck coefficient for such samples is larger than the Seebeck coefficient for a single period by about 10%. Secondly, assuming uniform carrier distribution in the Si quantum well layers and the $Si_{1-x}Ge_x$ quantum barrier layers underestimates the carrier density by 5%-20%, depending on the quantum well thickness. Thirdly, TEM studies (see Fig. 5-11 and the discussion on page 135) reveal that the samples we have studied in this section have a wavy in-plane microstructure arising from the relaxation growth of the $Si_{1-x}Ge_x$ buffer layer. This wavy microstructure introduces a 30% reduction in the thickness of a period from the nominal period thickness, which in turn results in an underestimation of the carrier concentration by

~30%. Considering all three correction factors suggests that quite good agreement is achieved between my theoretical modeling and the experimental study, especially considering that *no* adjustable parameters were used in the calculations. Therefore the experimental results appear to confirm the predictions of my theoretical modeling, showing that the $Si_{1-x}Ge_x$ quantum well superlattice structures may indeed be used to obtain a significant enhancement in ZT.

In summary, the enhancement of the thermoelectric power factor due to the quantum confinement effect has been demonstrated through the quantity S^2n. However, it appears that the carrier mobilities of the samples in this investigation are yet to be increased for this type of modulation doped structure. In order to increase the carrier mobility in the system, some materials science problems in the MBE growth technique have to be solved, which are beyond the scope of this thesis.

5.3.4 Temperature dependence

All the experimental investigations so far presented have been for 300 K. The results of Section 5.3.3 show that the enhanced thermoelectric figure of merit at 300 K for $Si/Si_{1-x}Ge_x$ superlattices makes this system very interesting for cooling purposes around room temperature. It is therefore interesting to see how our superlattice samples behave as a function of temperature.

Figures 5-13 and 5-14 show the temperature dependence of the electrical resistivity and the Seebeck coefficient, respectively, for five $Si/Si_{0.7}Ge_{0.3}$ superlattice samples with different quantum well sizes. All these samples have fifteen periods, and therefore the contribution from the buffer layers to the Seebeck coefficient measurements is less than 10%. The resulting temperature dependence of the thermoelectric power factor for these samples is shown in Fig. 5-15.

The behavior of the electrical resistivity and the Seebeck coefficient of these samples is typical for doped semiconductors [19]. As the temperature is decreased, all the superlattice samples show an decrease in the electrical resistivity and a decrease in the Seebeck coefficient. Notice that the carrier density for the 50 Å sample is much higher compared to the rest of the samples (see Tables 5.1 and 5.2), resulting in a

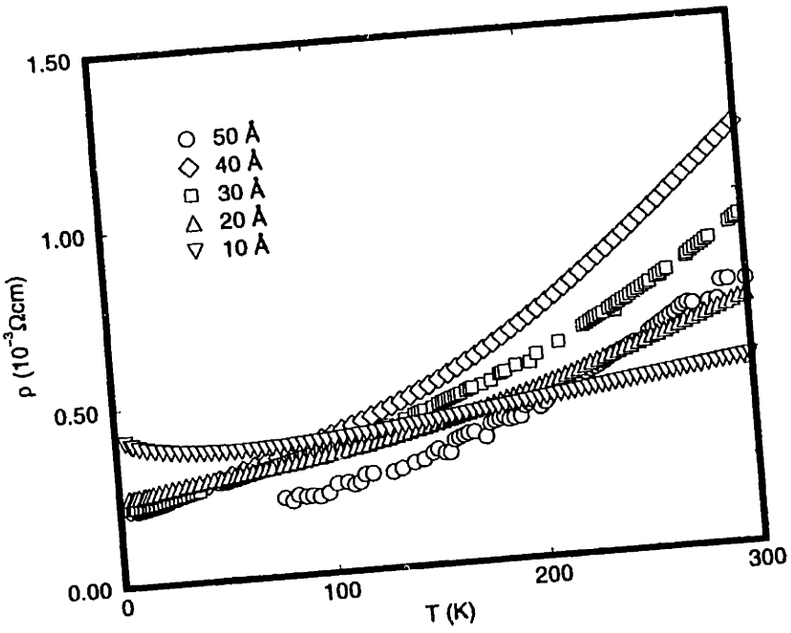

Figure 5-13: The temperature dependence of the electrical resistivity for $Si/Si_{0.7}Ge_{0.3}$ superlattice samples. All these samples have 15 periods.

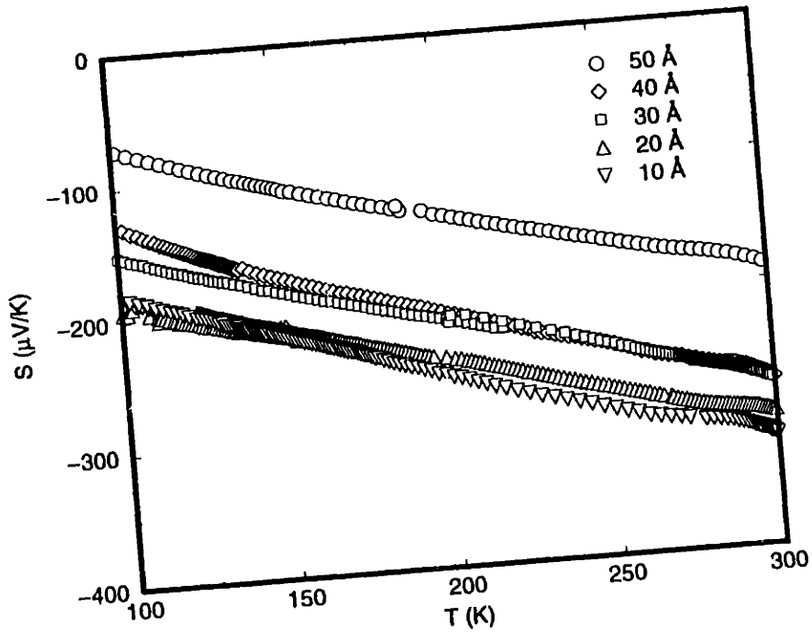

Figure 5-14: The temperature dependence of the Seebeck coefficient for $Si/Si_{0.7}Ge_{0.3}$ superlattice samples. All these samples have 15 periods.

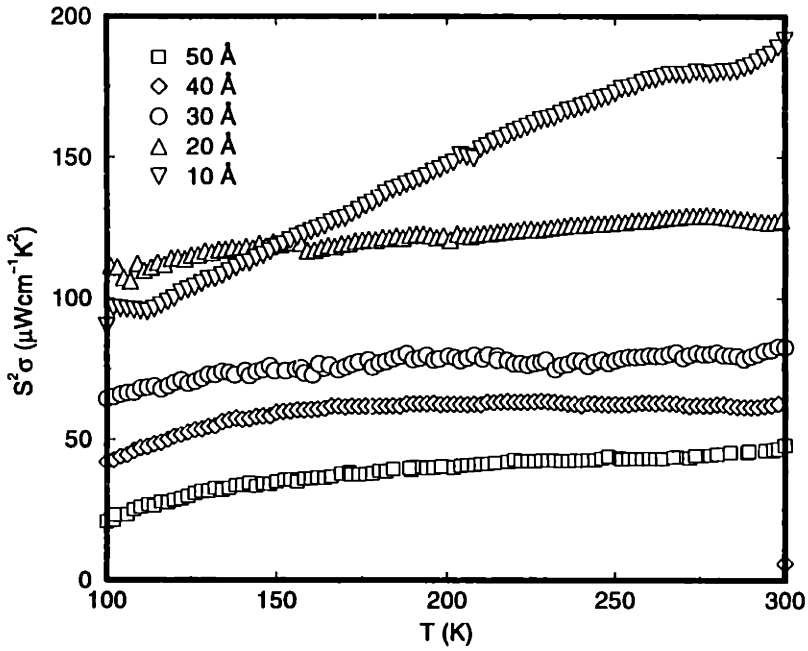

Figure 5-15: The temperature dependence of the power factor for $Si/Si_{0.7}Ge_{0.3}$ superlattice samples. All these samples have 15 periods.

relatively lower electrical resistivity and a lower Seebeck coefficient. The temperature dependence of the electrical resistivity shown in Fig. 5-13 indicates that samples with smaller quantum well widths are less sensitive to the temperature. In other words, $d\rho/dT$ decreases as the quantum well width decreases. This is because for smaller quantum wells, the scattering process for electrons is largely dominated by the interface scattering from the interface dislocations, which is less sensitive to the temperature. Therefore the mobility of electrons for smaller quantum wells is less sensitive to the temperature. The Seebeck coefficient for these superlattice samples show consistent enhancement for smaller quantum well widths. However, there is not as much difference in the behavior of the temperature dependent Seebeck coefficient. This is because as shown in Eq. (3.11), there is no mobility dependence in the Seebeck coefficient, so it is less affected by changes in the scattering mechanism.[8]

In Fig. 5-15, we observe a consistent enhancement in the thermoelectric power

[8]Significant changes in the scattering mechanism will, however, invalidate the relaxation-time approximation used to derive Eq. (3.11).

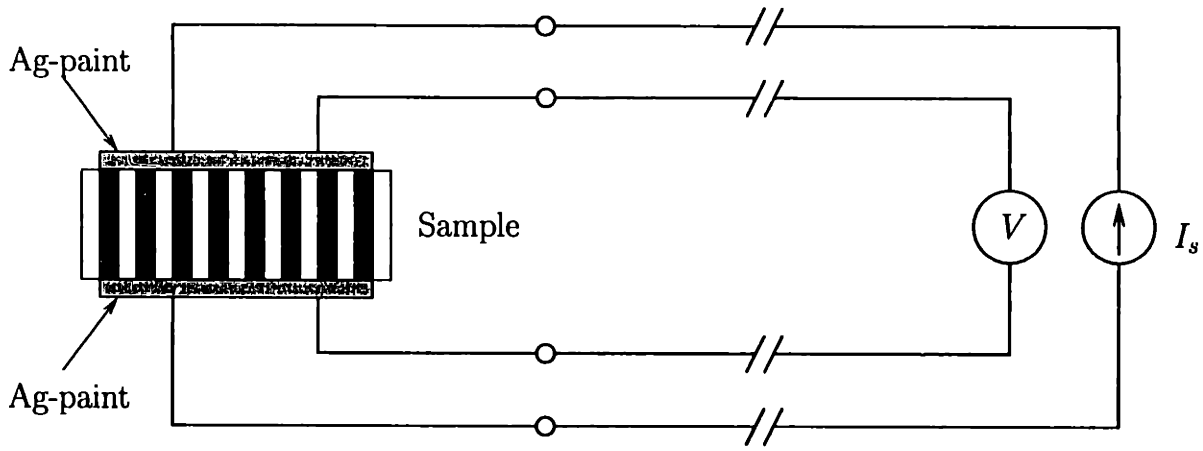

Figure 5-16: The schematic diagram of the pseudo-four-probe technique for the electrical conductivity measurement of Bi nanowire arrays.

factor ($S^2\sigma$) as the quantum well width decreases. It should also be pointed out that $S^2\sigma$ is an ascending function of the temperature for all samples, and therefore we expect better thermoelectric performance for $Si/Si_{1-x}Ge_x$ superlattices at elevated temperatures.[9]

5.4 Initial thermoelectric characterizations of Bi nanowire arrays

Recently, significant progress has been made with the fabrication of Bi nanowire arrays within anodic alumina templates [41]. These Bi nanowire arrays are close-packed Bi nanowires embedded in the porous anodic alumina template with their orientation perpendicular to the surface of the anodic alumina template. This causes extra difficulties in the characterization of the transport properties. It is, for example, difficult to perform regular four-point measurements for the electrical conductivity because of the configuration of the samples. In this thesis, I initiated a pseudo-four-

[9]The thermal conductivity of $Si_{1-x}Ge_x$ decreases as temperature goes above 300 K, reaching a minimum around 1000 K. We expect a somewhat similar behavior in the $Si/Si_{1-x}Ge_x$ superlattice structure, leading to an enhanced thermoelectric figure merit at elevated temperatures.

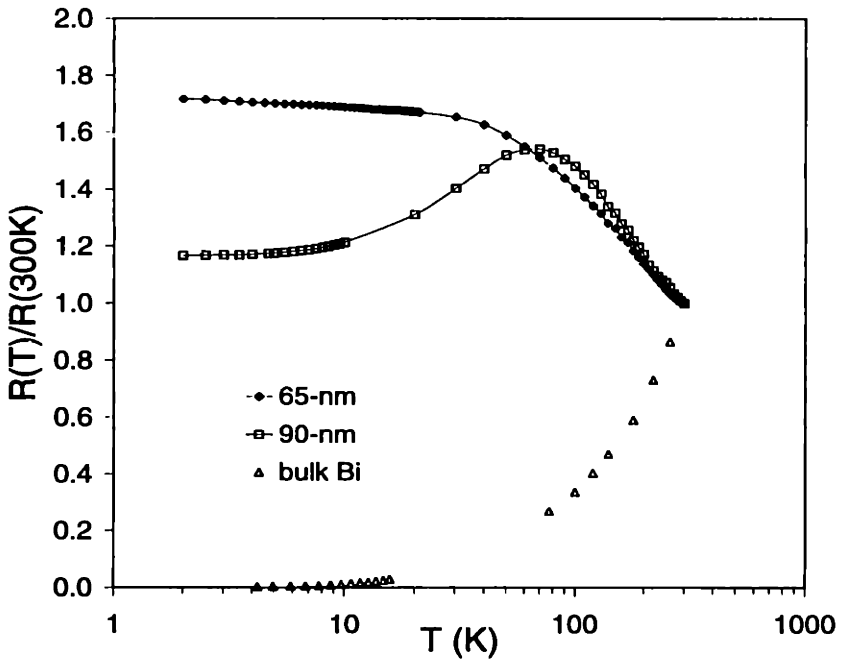

Figure 5-17: Temperature dependence of the resistance for Bi nanowire arrays with an average diameter of 65 nm and 90 nm. The data for bulk Bi is also shown for comparison.

probe method to solve part of the measurement problems. The configuration of this technique is shown in Fig. 5-16. Silver paint is used to make good ohmic electrical contacts on each side of the sample, on which four gold wires are attached. Two of the gold wires are connected to a current source, and the other two are connected to a sensitive digital voltmeter. The potential drop is measured for both forward and reverse currents to eliminate any thermoelectric effects. This configuration eliminates any potential drop across the wires and cables between the sample and the voltmeter, but can not eliminate the contact resistance. However, since Bi is a semimetal, over a large range of nanowire sizes when a significant effective band gap has not yet been developed, the Bi wires are metallic, and the nature of the contacts is metal-to-metal, so that the contact resistance is very small in most cases. One deficiency of this technique is that we cannot get the absolute values of the electrical conductivity, because the number of nanowires that are in contact with the silver paint can not be determined. However, the dependence of the electrical conductivity on temperature

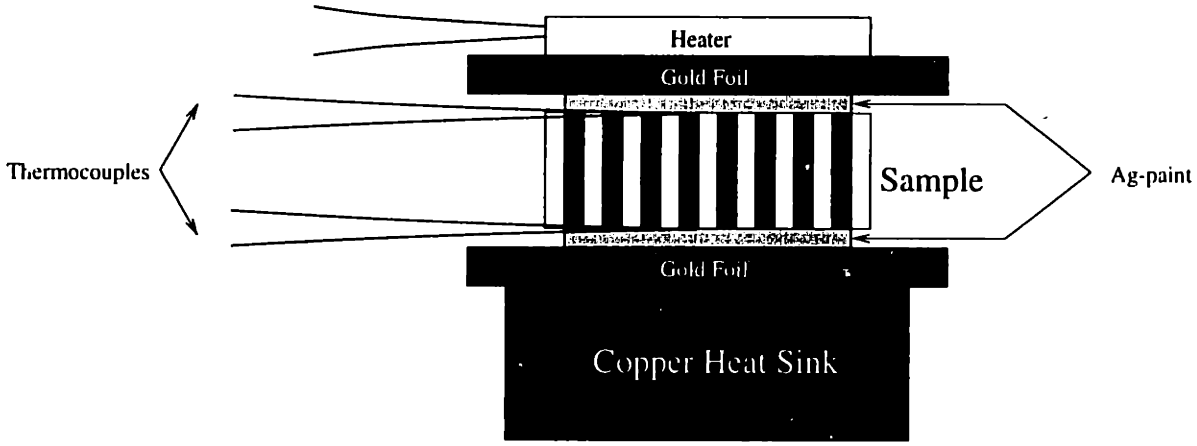

Figure 5-18: The schematic diagram of the technique for the Seebeck coefficient measurement of Bi nanowire arrays.

can be measured.

Figure 5-17 shows the temperature dependence of the resistance for Bi nanowire arrays with an average diameter of 65 nm and 90 nm. The data for bulk Bi are obtained from Refs. [58, 59]. All the data are scaled with respect to their values at $T =$ 300 K, and the resulting $R(T)/R(300K)$ can be interpreted as a normalized electrical resistivity. The increase in the electrical resistivity at lower temperatures for Bi nanowires arises from the reduced carrier concentration due to quantum confinement and the reduced carrier mobility due to interface scattering. A more detailed account of the electrical conductivity study of Bi nanowires was given in Ref. [60].

The measurement of the Seebeck coefficient of the Bi nanowire arrays is rather difficult because of the nature of the samples. The template is usually 50 to 100 μm in thickness, and therefore it is very difficult to get a sufficient temperature gradient across such a short distance. Figure 5-18 shows a schematic diagram of the technique that has been developed to characterize the Seebeck coefficient of Bi nanowire arrays. Silver paint is applied on both sides of the Bi nanowire array to provide good electrical and thermal contacts, and to attach two thermocouples onto the sample. The thermocouples are Omega's "cement-on" type-E (Chromel-Constantan) foil thermocouples, which are 0.0005″ (12.7 μm) in thickness. The thin foil thermocouples provide the smallest possible heat capacity at the junctions. The sample is, then,

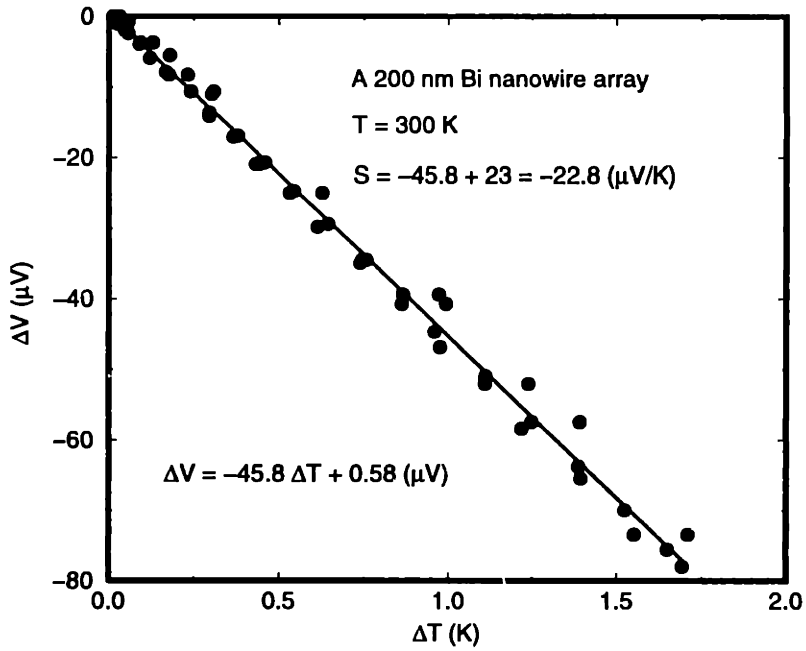

Figure 5-19: The Seebeck coefficient measurement of a 200 nm Bi nanowire array at room temperature.

sandwiched between two gold foils, one of which rests on the copper heat sink, while another is attached with a heater. A heater current (a few tens of mA) provides the heat that is needed to achieve the temperature gradient across the Bi nanowire array. The two thermocouples are used to measure the temperature gradient ΔT, and the thermoelectric voltage ΔV is measured through the two Chromel wires. The Seebeck coefficient is determined by performing a linear regression on the ΔV-ΔT data pairs to get the slope. Because the Chromel wires have a significant value of the Seebeck coefficient (23 μV/K), an adjustment is need to get the Seebeck coefficient value for the Bi nanowire array.

Figure 5-19 shows experimental data for a 200 nm Bi nanowire array at room temperature. Good linearity in the data is achieved, and the slope is found by a least square linear regression to be -45.8 μV/K. The Seebeck coefficient of the Bi nanowire array is thus found to be -22.8 μV/K, after a correction is made for the Seebeck value of the Chromel wires. The small offset (0.58 μV) at $\Delta T = 0$ indicates that both the electrical contacts and the thermal contacts to the Bi nanowires are of good quality.

This result is in good agreement with the measurements [61] carried out by Dr. J. P. Heremans of Delphi Research & Development using a slightly different technique, which uses a differential thermocouple to measure the temperature gradient across the sample.

Chapter 6

Suggestions for future studies

In this thesis, I established the basis of the low dimensional thermoelectric transport principle, which can outperform its bulk form, in the $Si/Si_{1-x}Ge_x$ quantum well superlattice (2D) system and the Bi quantum wire (1D) system. This work opens up a number of research possibilities that can be pursued in the future. In this chapter, I summarize a few potentially promising research directions that are worthy of pursuing in the immediate future.

6.1 The $Si/Si_{1-x}Ge_x$ quantum well system

A theoretical model has been developed in Chapter 3, and an experimental investigation has been performed in Section 5.3 for the $Si/Si_{1-x}Ge_x$ quantum well system. Beyond what I have achieved so far, there are several more directions that can be pursued.

6.1.1 Carrier pocket engineering in the Si/Ge superlattice system

The concept of carrier pocket engineering in the theory of low dimensional thermoelectricity was first introduced for use in the GaAs/AlAs superlattice system [18]. In bulk form, Si has 6 electron ellipsoids at the Δ-point in the Brillouin zone, and Ge

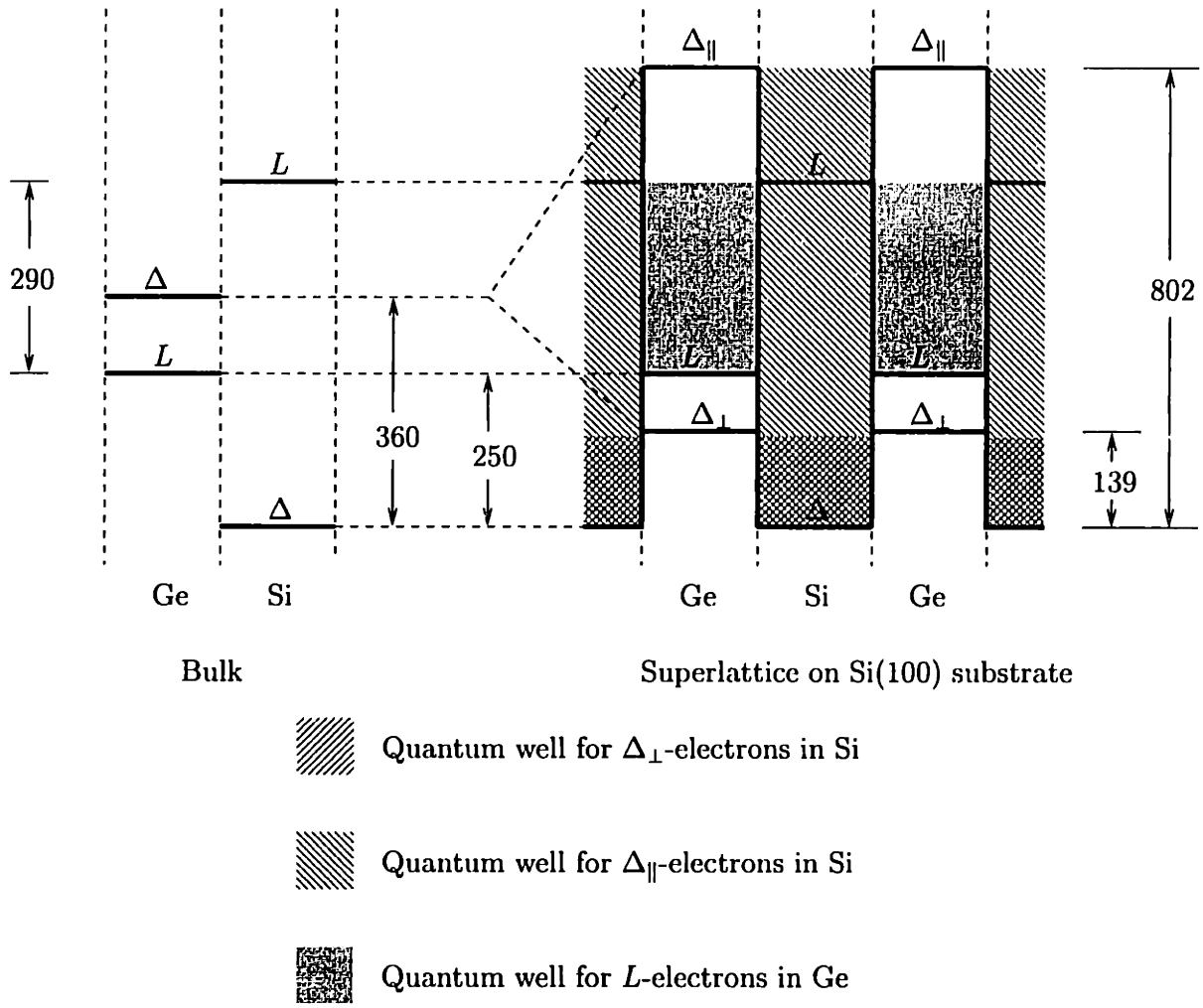

Figure 6-1: The conduction band extrema in bulk Si/Ge and in a Si(20Å)/Ge(20Å) superlattice grown on a Si(100) substrate. All the numbers are in units of meV.

has 4 electron ellipsoids at the L-point in the Brillouin zone. Therefore, Si and Ge form another ideal system for the application of carrier pocket engineering.

Figure 6-1 shows the conduction band extrema in bulk Si and Ge. An example of a Si(20Å)/Ge(20Å) superlattice grown on Si(100) substrate is also shown in Fig. 6-1. As the Si/Ge superlattice is grown on a Si substrate, the Si layers are relaxed, and the Ge layers are under compressive strain. Therefore, the 6-fold degenerate conduction band minima at the Δ-point split into two levels, denoted by $\Delta_\perp$ for the transverse electron pockets and $\Delta_\parallel$ for the longitudinal electron pockets. This forms two quantum wells for the electrons at the Δ-point in the Si layers, with quantum

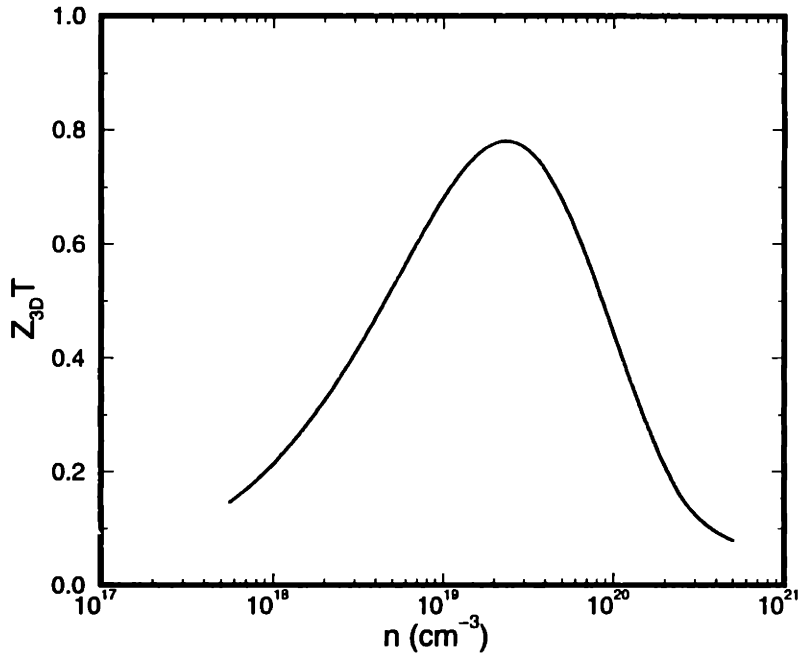

Figure 6-2: The calculated $Z_{3D}T$ as a function of carrier density n at room temperature for a Si(20Å)/Ge(20Å) superlattice grown on Si(001) substrate, using carrier pocket engineering model.

well depths of 139 meV for the transverse electrons and 802 meV for the longitudinal electrons, respectively. Although the $\Delta_{||}$-well is higher (by a factor of 5.8) than the $\Delta_{\perp}$-well, the confinement mass for the longitudinal electrons is also larger (by a factor of 4.5) than that for the transverse electrons. Therefore, the lowest conduction band subband levels for both transverse and longitudinal electrons in Si become very close. These nearly degenerate subbands give rise to a high density of states at the subband edge, therefore enhancing the thermoelectric performance in the Si/Ge superlattice.

Besides the quantum wells formed for the Δ-point electrons in the lowest conduction subband in the Si layers, a quantum well is also formed for L-point electrons in the Ge layers. However, as shown in Fig. 6-1, this quantum well is at a much higher energy. At the optimum doping level, this quantum well is not populated. Ideally, to make use of the Ge layers in a thermoelectric device, some smart designs are needed to bring the energy of the L-point quantum well down so that the subband levels in the L-point quantum well are close to those subband levels in the Δ-point quantum wells.

Figure 6-2 shows the calculated three dimensional thermoelectric figure of merit as a function of carrier concentration in the superlattice structure shown in Fig. 6-1, yielding a very interesting value for ZT.

Many more possibilities can be explored regarding the carrier pocket engineering in Si/Ge superlattice structures. Besides varying the thickness of the Si layers and Ge layers, we can also introduce $Si_{1-x}Ge_x$ buffer layers with different values of x to achieve different type and different amount the strain in the structure. Superlattices grown along the (111) direction are also interesting because of the 6-fold degeneracy of the electron ellipsoids at the Δ-point along this direction. Moreover, the $Si_{1-x}Ge_x/Si_{1-y}Ge_y$ superlattice structure, which has two more degrees of freedom, provides another interesting system to apply the concept of carrier pocket engineering. It is also interesting to apply the concept of carrier pocket engineering at elevated temperatures, because subbands at higher energy levels are easier to be populated at high temperatures.

6.1.2 Thermoelectric characterization at high temperatures

In Section 5.3, I experimentally investigated the thermoelectric transport properties of $Si/Si_{1-x}Ge_x$ superlattice structures, and demonstrated an enhancement of the thermoelectric performance at room temperature and below. This study suggests that the $Si/Si_{1-x}Ge_x$ superlattice structure should potentially be a good thermoelectric cooling system when operating around room temperature.

However, the $Si_{1-x}Ge_x$ alloy is a good thermoelectric material for power generation when it is operated at elevated temperatures around 1000 K. It is therefore interesting to study the thermoelectric properties of the $Si/Si_{1-x}Ge_x$ superlattice structure at elevated temperatures.

A high temperature thermoelectric transport measurement system has been designed and fabricated for this purpose. Figures 6-3 and 6-4 show some preliminary results for a $Si/Si_{0.7}Ge_{0.3}$ superlattice sample. We see that excellent agreement between the measurements on the low temperature setup and those on the high temperature setup is achieved. The next step of this research will be a systematic study of the

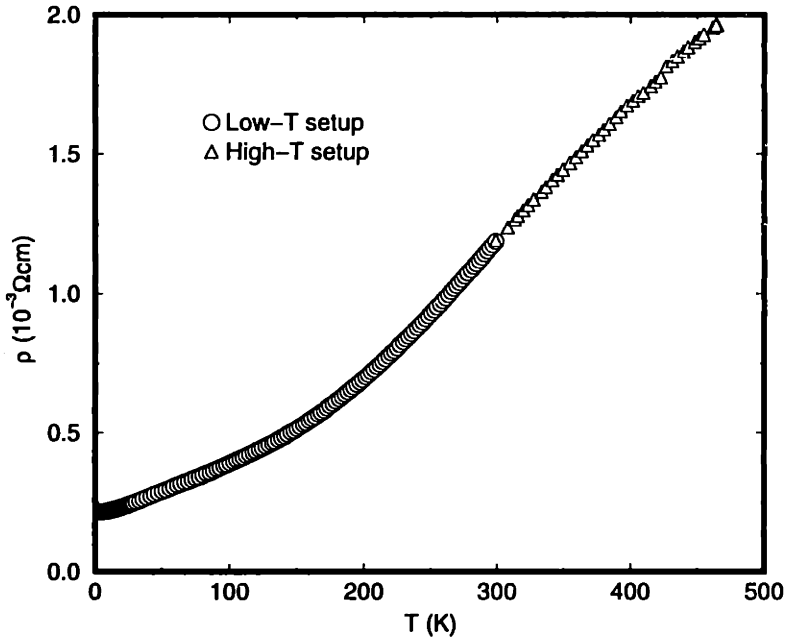

Figure 6-3: The temperature dependence of the electrical resistivity for a $Si/Si_{0.7}Ge_{0.3}$ superlattice sample characterized using both the low-temperature setup described in Section 5.1 and the newly constructed high-temperature setup. The sample consists of 15 periods of a 40 Å Si quantum well and a 300 Å quantum barrier.

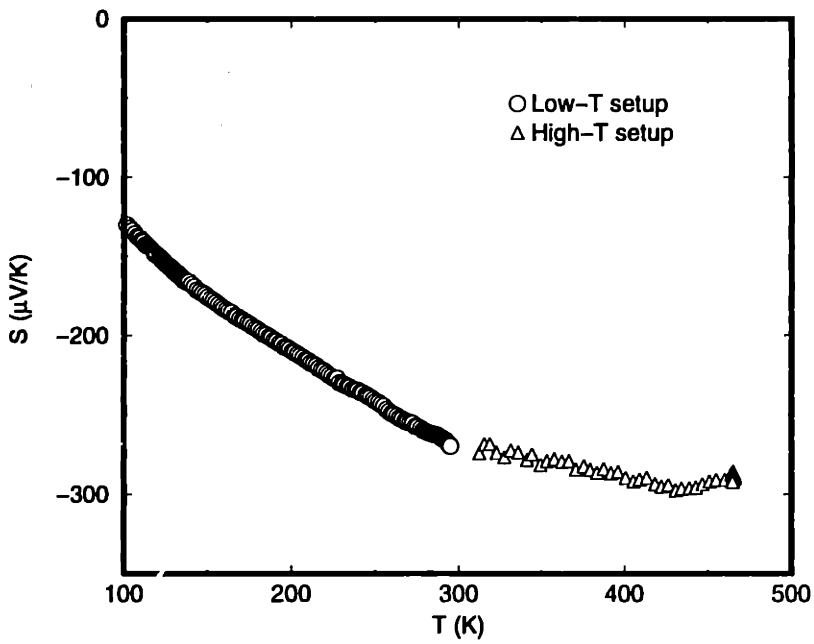

Figure 6-4: The temperature dependence of the Seebeck coefficient for a $Si/Si_{0.7}Ge_{0.3}$ superlattice sample characterized using both the low-temperature setup described in Section 5.1 and the newly constructed high-temperature setup. The sample consists of 15 periods of a 40 Å Si quantum well and a 300 Å quantum barrier.

$Si/Si_{1-x}Ge_x$ superlattice structures at elevated temperatures.

6.1.3 Searching for more $Si/Si_{1-x}Ge_x$ superlattice structures

In this thesis, I have studied n-type type II $Si/Si_{1-x}Ge_x$ superlattice structures to demonstrate the advantage of two-dimensional transport. In order to make thermoelectric devices, it is necessary to develop more structures with specific properties.

- As discussed in Section 3.7, by employing δ-doped wide band gap materials, such as SiC, within the barrier layers, it may be possible to improve quantum confinement of the carrier in the quantum wells. This strategy can also improve the high temperature thermoelectric performance for the $Si/Si_{1-x}Ge_x$ superlattice structures. Experimentally, boron and oxygen are also good candidates for this purpose besides carbon.

- In Section 5.3.2, I employed an extrapolative method to eliminate the contribution from the buffer layer to the Seebeck measurements done on the superlattices. A more direct approach could involve the use of a p-n junction on top of the buffer layer to isolate the buffer layer from the superlattice layers.

- In order to make thermoelectric devices, we also need p-type structures. Almost all of the structures discussed for n-type Si quantum wells now need to be developed for p-type materials.

- Experimental investigations are needed to test the carrier pocket engineering concept as discussed in Section 6.1.1. Therefore, specially designed structures are needed for this purpose.

6.2 Bismuth quantum wire system

The bismuth quantum wire system represents a new class of low-dimensional thermoelectric materials. This is an exciting field to be further studied, both theoretically and experimentally.

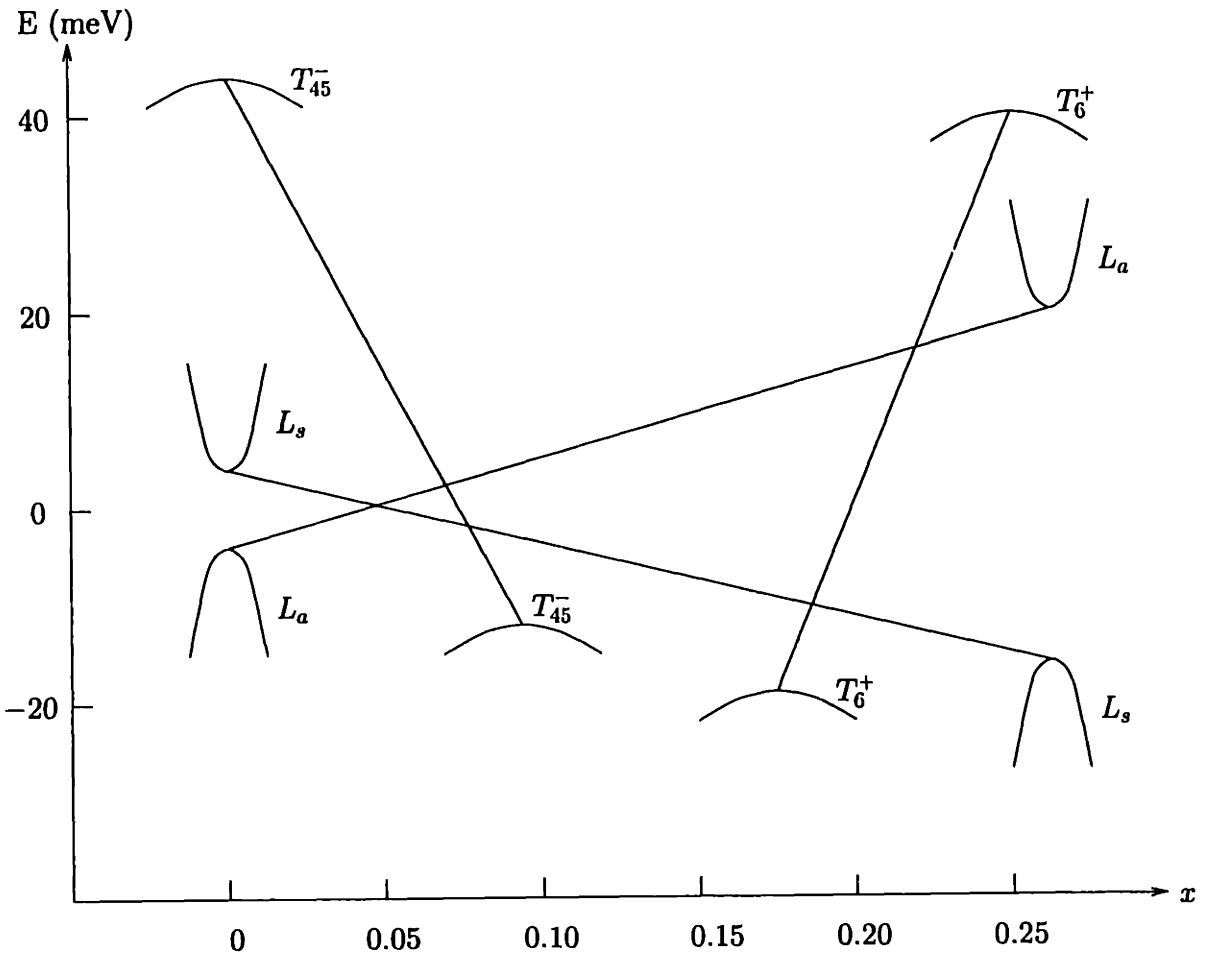

Figure 6-5: Variation of the energy spectrum of $Bi_{1-x}Sb_x$ alloys in the range of $0 < x < 0.25$.

6.2.1 Antimony alloying in Bi quantum wire system

As I have discussed in Chapter 4, the enhancement in $Z_{1D}T$ for p-type quantum wires is not as strong as that for n-type wires. It is therefore necessary to design structures with high $Z_{1D}T$ values for p-type wires. Antimony (Sb) alloying provides a possible mechanism for this purpose. This is because the addition of a small amount of Sb in Bi reduces the overlap of the valence band at the T-point and the conduction band at the L-point. For a range of Sb compositions, the valence band at the T-point lies lower than the valence band at the L-point, as shown in Fig. 6-5 [62]. Therefore it should be possible to utilize the holes in the L-point valence band for thermoelectric transport, so that p-type Bi nanowires with $Z_{1D}T$ comparable to that for n-type Bi

nanowires might be fabricated.

Figure 6-5 shows that the band edge of the valence band T_{45}^{-} is lowered on addition of Sb to Bi until about $x = 0.075$, where it moves below the L_s conduction band. Further addition of Sb causes the T_6^+ valence band to rise until at about $x = 0.18$, where it rises above the L-point L_s band edge. Therefore, in the range of $0.075 < x < 0.18$, it should be possible to make use of the holes in the L-point valence band. Considering that the effective mass of holes in the L-point valence band is much smaller than that of holes in the T-point valence band, the range of x values for Sb addition of interest may be smaller than (0.075, 0.18). The pertinent range of x may also depend on the size and orientation of the quantum wires. Using this approach we can expect to achieve a significant enhancement in $Z_{1D}T$ for p-type Bi quantum wires.

Another favorable effect of the addition of Sb is the reduction of the thermal conductivity due to point-defect scattering caused by the difference in masses of the Bi and Sb atoms.[1]

6.2.2 Thermoelectric characterization of Bi nanowires

The characterization techniques used for Bi nanowires that were discussed in Section 5.4 have been preliminary. In order to get a more complete characterization of the thermoelectric properties of the Bi nanowires, a few further studies need to be pursued.

- The characterization of the absolute value of the electrical conductivity for a single Bi nanowire is a challenge but a necessary technique to be developed. A possible method is to use micro-fabrication techniques to make four ohmic contacts directly on a free standing Bi nanowire. An alternative method is to use a scanning tunneling microscopy technique to perform electrical measurements on a single Bi nanowire within the template.

[1] For example, the addition of 12% Sb to bulk Bi reduces the thermal conductivity by 20% [63].

- The method of characterizing the Seebeck coefficient described in Section 5.4 is successful for a Bi nanowire array. However, it would be interesting to be able to measure the Seebeck coefficient of a free standing Bi nanowire. On such a small scale, it is very difficult to use a conventional heater to provide the necessary temperature gradient. A possible solution to this problem is to use a portion of the Bi nanowire itself as the heater. This technique, of course, relies on the success of making good ohmic contacts to a Bi nanowire.

- In order to make Bi nanowires with optimum thermoelectric performance, the wires need to be doped. Therefore, doping techniques for both n-type and p-type dopants need to be developed. For n-type nanowires, tellurium (Te) is a good dopant and some preliminary success with this dopant has already been achieved [64]. For p-type Bi nanowires, tin (Sn) or lead (Pb) could be a good candidate. In order to characterize the doping level or the carrier concentration in the Bi nanowires, Shubnikov-de Haas (SdH) effect measurements at low temperature provide a possible method, provided that the condition for quantum oscillatory behavior in a magnetic field, $\omega_c\tau \gg 1$, can be achieved, where ω_c and τ are, respectively, the cyclotron frequency and the relaxation time for the carriers.

6.2.3 Miscellaneous

Besides the two major efforts to be made for the Bi quantum wire system, I here itemize a few more random thoughts that could also be important.

- In Chapter 4, theoretical modeling has been performed for Bi quantum wires oriented along the three principal crystalline directions. However, Bi nanowires fabricated in the laboratory might not have an orientation along one of the principal directions. For example, the most recent technique [41] used for the fabrication of Bi nanowire arrays suggests a preferred orientation along the $[10\bar{1}1]$ direction. Therefore, it is important to extend the theoretical modeling to

Bi nanowires oriented along the preferred directions found in samples prepared experimentally.

- Throughout this thesis, I have assumed that the Bi nanowires with a square cross section. Although this is a very good approximation, a more detailed calculation with a circular cross section would also be beneficiary. In this case, the Schrödinger equation for the subband energy levels becomes anisotropic

$$\nabla \cdot \mathbf{m}^{-1} \cdot \nabla \Psi = \frac{2E}{\hbar^2} \Psi \tag{6.1}$$

with an anisotropic effective mass tensor $\mathbf{m}$ and a circular boundary condition. This differential equation need to be solved numerically.

- Actual scattering mechanisms need to be considered in the modeling. This is especially important to take into account the effect of phonon scattering on the lattice thermal conductivity. With more scattering interfaces introduced in the nanowire system, we expect a reduction in the lattice thermal conductivity, thereby resulting in a further enhancement of the 1D thermoelectric figure of merit.

- As indicated by the results of my theoretical modeling (Chapter 4), we need a quantum wire size smaller than 100 Å in order to get significant enhancement in the 1D thermoelectric figure of merit. For such a small wire size, both fabrication and characterization remain major challenges.

Appendix A

Intrinsic bismuth quantum wires

It is also interesting to examine the magnitude and temperature dependence of the carrier density for intrinsic Bi quantum wires. This information gives perspectives of how difficult it is to dope the system for optimum thermoelectric performance and the relative importance of the thermal excitation mechanism.

In this appendix, I calculated the intrinsic carrier concentration for a 100 Å Bi quantum wire along the three principal crystallographic directions. For a single band of a one-dimensional (1D) conductor with effective mass m^*, the carrier density is given by

$$n = \int \frac{dk}{\pi a^2} f(\varepsilon(k)) = \frac{1}{\pi a^2} \left(\frac{2k_B T}{\hbar^2} \right)^{\frac{1}{2}} (m^*)^{\frac{1}{2}} F_{-\frac{1}{2}}, \tag{A.1}$$

where a is the quantum wire size, and $F_{-\frac{1}{2}}$ is defined in Eq. (4.9). For a 100 Å intrinsic Bi quantum wire, it is a 1D semiconductor, and all the carriers, including electrons and holes, are thermally excited. First, the Fermi level is found by equating

$$n_e = n_h \equiv n_0, \tag{A.2}$$

and the results are shown in Fig. A-1. The Fermi energies E_F^e and E_F^h in the figure are measured with respect to the lowest conduction subband edge and the highest valence subband edge, respectively, and $E_F^e + E_F^h = -\Delta$, where Δ is the band gap between the lowest conduction subband and the highest valence subband. The non-

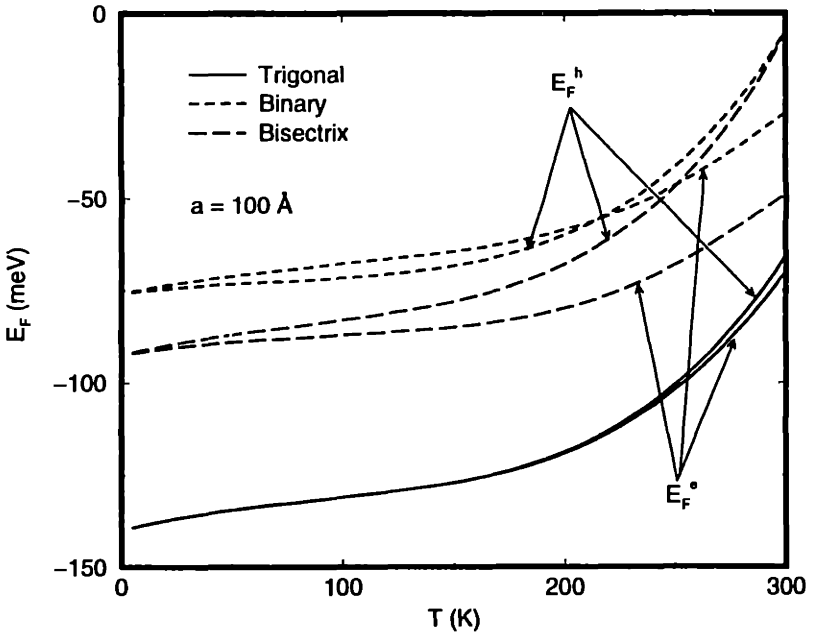

Figure A-1: The calculated temperature dependence of the Fermi levels for a 100 Å intrinsic Bi quantum wire along the principal crystallographic directions. E_F^e and E_F^h are measured with respected to the lowest conduction subband edge and the highest valence subband edge, respectively.

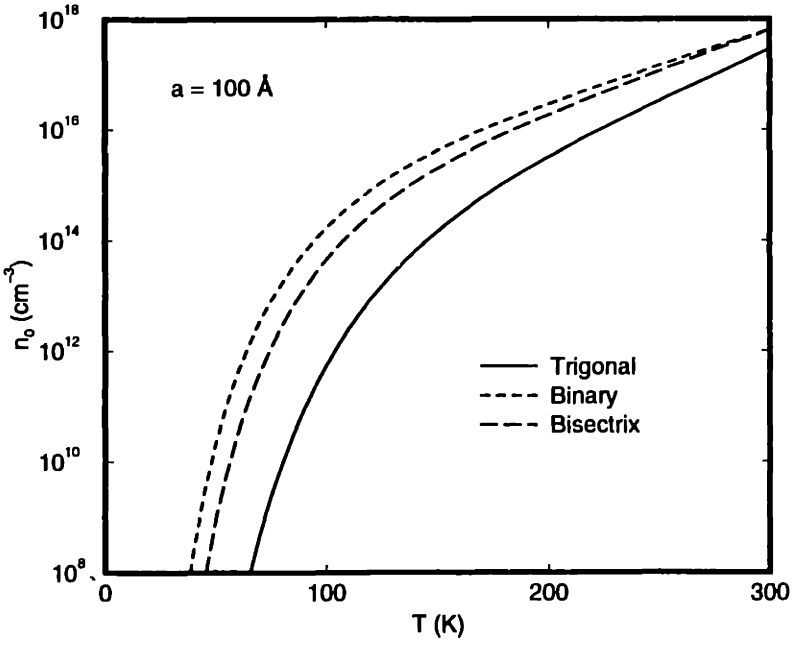

Figure A-2: The calculated temperature dependence of the intrinsic carrier concentration, $n_0 = n_e = n_h$, for both electrons and holes for a 100 Å intrinsic Bi quantum wire along the principal crystallographic directions.

parabolic characteristic for the conduction band and the temperature dependent band parameters are considered in the calculation. After getting the Fermi level of the intrinsic system, the carrier concentrations are calculated using Eq. (A.1), and the results are presented in Fig. A-2 showing that the thermal excitation plays a very important role in this 1D semiconductor system.

Bibliography

[1] T. J. Seebeck, Abh. Preuss. Akad. Wiss. page 265 (1822–1823).

[2] A. F. Ioffe, *Semiconductor Thermoelements and Thermoelectric Cooling* (Infosearch Ltd., London, 1957).

[3] H. D. Lutz and G. Kliche, Phys. Status Solidi B **112**, 549 (1982).

[4] W. Jeitschko and D. Braun, Acta Crystallogr. B **33**, 3401 (1977).

[5] L. D. Hicks and M. S. Dresselhaus, Phys. Rev. B **47**, 12727 (1993).

[6] L. D. Hicks and M. S. Dresselhaus, Phys. Rev. B **47**, 16631 (1993).

[7] L. D. Hicks, T. C. Harman, and M. S. Dresselhaus, Appl. Phys. Lett. **63**, 3230 (1993).

[8] Lyndon D. Hicks, *The effect of quantum-well superlattices on the thermoelectric figure of merit*, PhD thesis, Massachusetts Institute of Technology, June 1996.

[9] L. D. Hicks, T. C. Harman, X. Sun, and M. S. Dresselhaus, Phys. Rev. B **53**, R10493 (1996).

[10] L. D. Hicks, T. C. Harman, X. Sun, and M. S. Dresselhaus, in *Proceedings of the 15th IEEE International Conference on Thermoelectrics, Pasadena, CA*, edited by J.-P. Fleurial, page 450, Institute of Electrical and Electronics Engineers, Inc., Piscataway, NJ, 1996.

[11] X. Sun, M. S. Dresselhaus, K. L. Wang, and M. O. Tanner, in *Advances in Microcrystalline and Nanocrystalline Semiconductors – 1996*, edited by P. M.

Fauchet, R. W. Collins, P. A. Alivisatos, I. Shimizu, T. Shimada, and J.-C. Vial, page 261, Materials Research Society Press, Pittsburgh, PA, 1997.

[12] X. Sun, M. S. Dresselhaus, K. L. Wang, and M. O. Tanner, in *Thermoelectric Materials - New Directions and Approaches*, edited by T. M. Tritt, M. G. Kanatzidis, H. B. Lyon, Jr., and G. D. Mahan, page 169, Materials Research Society Press, Pittsburgh, PA, 1997.

[13] T. Koga, X. Sun, S. B. Cronin, M. S. Dresselhaus, K. L. Wang, and G. Chen, J. Computer-Aided Materials Design **4**, 175 (1997).

[14] T. Koga, S. B. Cronin, T. C. Harman, X. Sun, and M. S. Dresselhaus, in *Semiconductor Process and Device Performance Modeling*, edited by J. S. Nelson, C. D. Wilson, and S. T. Dunham, Materials Research Society Press, Pittsburgh, PA, 1998.

[15] G. Dresselhaus, M. S. Dresselhaus, Z. Zhang, X. Sun, J. Ying, and G. Chen, in *Proceedings of the Seventeenth International Conference on Thermoelectrics*, edited by K. Koumoto, Institute of Electrical and Electronics Engineers, Inc., Piscataway, NJ, 1998.

[16] X. Sun, G. Chen, K. Wang, and M. S. Dresselhaus, in *Proceedings of the Seventeenth International Conference on Thermoelectrics*, edited by K. Koumoto, Institute of Electrical and Electronics Engineers, Inc., Piscataway, NJ, 1998.

[17] G. Chen, K. L. Wang, and M. S. Dresselhaus, Phys. Rev. B (1998).

[18] T. Koga, X. Sun, S. B. Cronin, and M. S. Dresselhaus, Appl. Phys. Lett. **73**, 2950 (1998).

[19] H. J. Goldsmid, *Thermoelectric Refrigeration* (Plenum Press, New York, 1964).

[20] H. J. Goldsmid, *Electronic Refrigeration* (Pion, London, 1986).

[21] B. Sherman, R. R. Heikes, and R. W. Ure, J. Appl. Phys. **31**, 1 (1960).

[22] G. H. Jonker, Philips Res. Repts **23**, 131 (1968).

[23] N. W. Ashcroft and N. D. Mermin, *Solid State Physics*, chapter 13, (Holt, Rinehart and Winston, New York, 1976).

[24] A. V. Ioffe and A. F. Ioffe, Dokl. Akad. Nauk SSSR **98**, 5, 757 (1954).

[25] G. A. Slack and M. A. Hussain, J. Appl. Phys. **70**, 2694 (1991).

[26] C. B. Vining, in *CRC Handbook of Thermoelectrics*, edited by D. M. Rowe, page 329, CRC Press, New York, 1995.

[27] G. D. Mahan, in *Solid State Physics*, edited by H. Ehrenreich and F. Spaepen, page 82, Academic Press, 1997.

[28] C. Wood, Rep. Prog. Phys. **51**, 459 (1988).

[29] O. Madelung, in *Landolt-Börnstein Numerical Data and Functional Relationships in Science and Technology, New Series*, page 43, edited by K.-H. Hellwege (Springer-Verlag, Berlin, 1982), Vol. 17a.

[30] R. Braunstein, A. R. Moore, and F. Hereman, Phys. Rev. **109**, 695 (1958).

[31] G. Abstreiter, H. Brugger, and T. Wolf, Phys. Rev. Lett. **54**, 2441 (1985).

[32] E. Kasper, H.-J. Herzog, H. Jorke, and G. Abstreiter, Superlattices and Microstructures **3**, 141 (1987).

[33] K. Ismail, in *Low-Dimensional Electronic Systems*, edited by G. Bauer, F. Kuchar, and H. Heinrich, page 333, Springer-Verlag, Berlin, 1992.

[34] S. Krishnamurthy, A. Sher, and A.-B. Chen, Phys. Rev. B **33**, 1026 (1986).

[35] G. Chen, J. Heat Transfer **119**, 220 (1997).

[36] R. A. Smith, *Semiconductors*, 2nd ed., (Cambridge University Press, Cambridge, 1978).

[37] S. S. Li, NBS Special Publication **400-33**, 13 (1977).

[38] L. I. Schiff, *Quantum Mechanics*, 3rd ed., (McGraw-Hill, New York, 1968).

[39] C. F. Gallo, B. S. Chandrasekhar, and P. H. Sutter, J. Appl. Phys. **34**, 144 (1963).

[40] K. Itaya, S. Sugarwara, K. Arai, and S. Saito, J. Chem. Engr. Jpn. **17**, 514 (1984).

[41] Z. Zhang, J. Y. Ying, and M. S. Dresselhaus, J. Mater. Res. **13**, 1745 (1998).

[42] D. Schiferl and C. S. Barrett, J. Appl. Crystallogr. **2**, 30 (1969).

[43] R. D. Brown, R. L. Hartman, and S. H. Koenig, Phys. Rev. **172**, 598 (1968).

[44] B. Lax and J. G. Mavroides, in *Solid State Physics*, edited by F. Seitz and D. Turnbull, page 261, Academic Press, New York, 1960.

[45] B. Lax, J. G. Mavroides, H. J. Zeiger, and R. J. Keyes, Phys. Rev. Lett. **5**, 241 (1960).

[46] B. Lax, Bull. Am. Phys. Soc. **5**, 167 (1960).

[47] R. T. Isaacson and G. A. Williams, Phys. Rev. **185**, 682 (1969).

[48] J. Heremans and O. P. Hansen, J. Phys. C: Solid State Phys. **12**, 3483 (1979).

[49] M. P. Vecchi and M. S. Dresselhaus, Phys. Rev. B **10**, 771 (1974).

[50] G. A. Saunders and Z. Sümengen, Proc. Roy. Soc. London **A329**, 453 (1972).

[51] G. K. White, J. Phys. C **5**, 2731 (1972).

[52] K. Walther, Phys. Rev. **174**, 782 (1968).

[53] Y. Eckstein, A. W. Lawson, and D. H. Reneker, J. Appl. Phys. **31**, 1534 (1960).

[54] T. C. Harman, D. L. Spears, and M. J. Manfra, J. Electron. Mater. **25**, 1121 (1996).

[55] J. Liu and K. L. Wang, private communication.

[56] X. Y. Zheng, M. Chen, and K. L. Wang, in *Porceedings of the seventh International Symposium on MEMS*, 1996.

[57] R. Gronsky, T. Radetic, B. Bloom, J. Szostak, M. Sander, and C. Caylor, Annual Review of the DoD MURI on Quantum Structures for Thermoelectric Applications, 1999.

[58] R. Hartmann, Phys. Rev. **181**, 1070 (1969).

[59] J.-P. Michenaud and J.-P. Issi, J. Phys. C **5**, 3061 (1972).

[60] Z. Zhang, *Fabrication, characterization and transport properties of bismuth nanowire systems*, PhD thesis, Massachusetts Institute of Technology, February 1999.

[61] J. Heremans, C. M. Thrush, S. Cronin, Z. Zhang, X. Sun, M. S. Dresselhaus, J. Y. Ying, and J. Mansfield, Phys. Rev. B (1999), in preparation.

[62] N. B. Brandt, S. M. Chudinov, and V. G. Karavaev, Sov. Phys. JEPT **34**, 368 (1972).

[63] T. Yazaki, J. Phys. Soc. Jpn. **1054**, 25 (1968).

[64] J. Heremans, C. M. Thrush, D. T. Morelli, Z. Zhang, X. Sun, M. S. Dresselhaus, and J. Y. Ying, Bulletin of the American Physical Society **44**, 226 (1999).